UC Berkeley
UC Berkeley Electronic Theses and Dissertations

Title
Synthesis and Assembly of 2D Materials for Sensing and Clean Energy Applications

Permalink
https://escholarship.org/uc/item/4r86v2wk

Author
Zang, Xining

Publication Date
2017

Peer reviewed|Thesis/dissertation

eScholarship.org Powered by the California Digital Library
University of California

Synthesis and Assembly of 2D Materials for Sensing and Clean Energy Applications

By

Xining Zang

A dissertation submitted in partial satisfaction of the

requirements for the degree of

Doctor of Philosophy

in

Engineering-Mechanical Engineering

in the

Graduate Division

of the

University of California, Berkeley

Committee in charge:

Professor Liwei Lin, Chair
Professor Costas Grigoropoulos
Professor Jie Yao

Summer 2017

© Copyright 2017
Xining Zang
All rights reserved

Abstract

Synthesis and Assembly of 2D Materials for Sensing and Clean Energy Applications

by

Xining Zang

Doctor of Philosophy in Mechanical Engineering

University of California, Berkeley

Professor Liwei Lin, Chair

Structurally two-dimensional materials such as graphene, transition metal dichalcogenide (TMDC), and transition metal carbide (TMC) have various unique properties for possible sensing and clean energy applications. The fabrication methods toward large scale, defect-free, single crystal manufacturing of these 2D materials have been difficult and challenge, include chemical vapor deposition (CVD), atomic layer deposition (ALD) and metal organic chemical vapor deposition (MOCVD). This work presents a few approaches for the synthesis and assembly of 2D materials by promoting the reaction dynamics with seeding catalysts or template structures for self-limiting kinetics to synthesize 2D materials, including graphene based on a droplet-CVD process, 2D-TMDC based on hydrogel scaffolds, and 2D-TMC based on hydrogel mixtures with direct-write laser processes.

A liquid metal droplet-based chemical vapor deposition process is developed for the synthesis of single-layer graphene flakes utilizing molten nickel droplets (nominal diameter from 0.5 to 1μm) as the catalysts. Experimentally, both single- and double-layer graphene flakes with low defects have been synthesized by using nickel thin films of either less or more than 100nm (up to 130nm) in thickness, respectively. When the original nickel thin film is 75 nm in thickness, the resulting nickel droplets are physically and electrically isolated, while after the CVD synthesis process, the graphene flakes are found to be electrically connected due to the outgrowth of graphene. These electrically-connected graphene sheets could be readily available for device applications without the need of transfer processes. We demonstrate the direct generation of photocurrents (up to 0.53 $\mu A/mm^2 \cdot W$) due to the photo-thermal effect based on as-fabricated graphene sheets.

A two-step atomistic layer deposition process is developed by depositing TiN by ALD and then annealing TiN in sulfur vapor. Such method is used to coat TiS_2 onto carbon nanotube (CNT) forest for highly conductive electrodes with high capacitance and cyclability in supercapacitors. Furthermore, a high concentration electrolyte (21m LiTFSI) is employed to intercalate with TiS_2 and the results show high electrochemical window (3V). Such

TiS_2/CNT- LiTFSI system results in 195 F/g specific capacitance, 60.9 Wh/kg energy density and 1250 W/kg in power density. This material system also outperforms the most typical highest energy materials from oxide, nitride, transition metal carbide and chalcogenide families for unique advantage and promising application in high energy, high power, and high voltage supercapacitor applications.

A solution-based method is developed for the synthesis of 2D materials driven by the layer-by-layer self-assembly of gelatin to convert ions to 2D carbides and chalcogenides using either CVD or laser processes. The resulting material has typical thickness of 10~15nm with more than 20μm in domain size including MoC_x, WC_x and CoC_x using CO_2 laser under ambient condition. The conductive and highly porous structures are utilized for energy storage applications. Specifically, gravimetric capacitance of laser-induced Mo_3C_2 can produce up to 100 F/g supercapacitors in Mg^{2+} based electrolyte. Mo_3C_2 electrodes also show exceptional operation stability from -50 to 300 ^oC in conjunction with semi-solid LiTFSI-PVA electrolyte. Furthermore, 2D carbide materials can also be directed constructed on paper using laser for disposable and foldable electronics. Finally, with the control of precursor concentration, thin MoS_2 sheets with thickness from few μm to few tens of nm are developed with monolayer type photoluminescence characteristics at 1.8 eV.

To my parents and my husband Dr X

Table of contents

Abstract 1
Table of contents ii
List of Figures iv
List of Table vii
Acknowledgments viii
1 Chapter: Introduction 1
1.1 Application of 2D materials 1
1.2 Synthesis of 2D materials 2
1.3 Structure of the dissertation 3
2 Chapter: Synthesis of Single Layer Graphene on Nickel Using a Droplet CVD Process 6
2.1 Abstract 6
2.2 Introduction 6
2.3 Results and Discussion 7
2.4 Conclusion 20
2.5 Experimental Section 20
3 Chapter: TiS_2 Coated Carbon Nanotube Hybrid Electrodes Enable High Energy Density Pseudocapacitors 23
3.1 Abstract 23
3.2 Introduction 23
3.3 Results and Discussion 25
3.4 Experiment Session 35
4 Chapter: Direct Laser Synthesis of Two-Dimensional Transition Metal Carbides in Ambient Environment 39
4.1 Abstract 39
4.2 Introduction 39
4.3 Results and Discussion 41
4.4 Experimental Sessions 50
4.5 Appendix 50
5 Chapter: Foldable Paper Electronics by Direct-Write Laser Patterning 54
5.1 Abstract 54
5.2 Introduction 54

5.3 Results and Discussion 55
5.3.1 Characterization 55
5.3.2 Applications 60
5.4 Experimental Session: 65
6 Chapter: Surfactant assisted large-scale synthesis of MoS_2 67
6.1 Abstract 67
6.2 Introduction 67
6.3 Results and Discussion 68
6.4 Experimental Sessions: 73
7 Chapter: Conclusion 75
7.1 Summary of Current Research 75
7.2 Future Directions 76
Biography 78

List of Figures

Figure 1.1 illustrating different method for 2D materials synthesis. 3

Figure 2.1 Schematics showing the droplet-based CVD process. 8

Figure 2.2 SEM images showing the size and distribution of nickel droplets after the droplet CVD process to synthesize graphene with different initial film thicknesses. . 9

Figure 2.3 Raman spectra corresponding to the droplet-based CVD growth process. 10

Figure 2.4 Raman spectra mapping results with sample area of 4×4μm^2. 10

Figure 2.5 2D peak Full Width of Half Maxim (FWHM) of graphene vs initial film thickness. Single layer graphene shows narrower than 55 cm^{-1}. 11

Figure 2.6 SEM images showing the size and distribution of copper droplets after the droplet CVD process to synthesize graphene with different initial film thicknesses 11

Figure 2.7 Raman spectra corresponding to the droplet-based CVD growth process with initial nickel film thickness of 20, 30, 40, 50, 75, 105, 130 nm. 12

Figure 2.8 AFM results of nickel droplet and analysis of carbon solutbility 13

Figure 2.9 Estimation of carbon absorped in nickel droplet and the carbon amount to form graphene on nickel droplet surface. 14

Figure 2.10 The generation of photocurrents on as-fabricated graphene flakes samples after the droplet CVD process with electrodes fixed at the two opposites, diagonal ends of the chip.. 17

Figure 2.11 Photocurrent characterizations. 18

Figure 2.12 Bandgap simulation of nickel-graphene contact, and Fermi level shift. 19

Figure 2.13 Raman spectra results showing a blue-shift of the 2D intensity peak of graphene flakes fabricated by the droplet CVD process implying hybridization from nickel. 20

Figure 3.1 TiS_2-VACNT hybrid fabrication process and advantage as Pseudocapacitor electrodes. 24

Figure 3.2 Transmission electron microscope (TEM) image of TiN coated CNT, scale bar 20 nm. 25

Figure 3.3 SEM and Diameter analysis of TiN-VACNT electrodes after 500 and 800 ALD cycles of TiN coatings and after the sulfur annealing process to convert TiN to TiS_2 composite. 26

Figure 3.4 Material characterization of the TiS_2-VACNT composite electrodes.. 26

Figure 3.5 X-ray photoelectron spectroscopy (XPS) and Electron dispersion spectrum(EDS) of the TiS_2-VACNT composite electrodes. 27

Figure 3.6 Electrochemical testing results of TiS_2-VACNT composite electrodes in the 21 m LiTFSI electrolyte. 28

Figure 3.7 Testing results of TiS_2-VACNT composite electrodes grown on the stainless-steel substrate using a 10 nm-thick Al_2O_3 passivation layer. 29

Figure 3.8 Cyclic Voltammetry tests of the TiS_2-VACNT composite electrode systems in the 10m and 1m LiCl electrolyte with different scan rates. 29

Figure 3.9 Chronopotentiometry charge-discharge curve of a TiS_2-VACNT electrode system in 21m LiTFSI electrolyte at varying current densities. 30

Figure 3.10 SEM and XRD of TiS_2-VACNT hybrid before and after 10,000-cycle cyclic voltametery test. 30

Figure 3.11 CV tests of the TiS_2-VACNT composite electrode systems under different temperature, showing similarity in capacitance after the integration of the current density curve.. 31

Figure 3.12 Cyclic voltammetry test results of TiS_2-VACNT electrode systems in different electrolytes. 31

Figure 3.13 TiS_2-VACNT composite electrodes outperform other VACNT-based electrodes coated with high-energy pseduocapacitive materials such as RuO_x, TiN, and MoS_2. 33

Figure 3.14 SEM image MoS_2 flower grown on top of VACNT forest. 33

Figure 3.15 Demonstration of potential application. 34

Figure 3.16 (Left) illustration of TiS_2-VACNT density measurement. (Right) mass change. 37

Figure 4.1 Schematic of the process for laser-induced transition metal carbides. 41

Figure 4.2 Characterizations of laser ablated Mo-gelatin gel.. 42

Figure 4.3 Meta-stable phase of Molybdenum and Tungsten carbide from XRD characterizations and their phase diagram 43

Figure 4.4 Laser ablated Mo-gel with different polymer, inlcuding PVP and PEO.. 45

Figure 4.5 SEM and XRD images of particles and structure of laser ablated iron-gelatin and nickel-gelatin films. and oxide/carbide hybrid by using the Ti^{4+} and Zr^{4+} precursor. 46

Figure 4.6 SEM of fabricated metal/metal oxide film by using a UV laser. 47

Figure 4.7 Energy storage capability of carbide material in different electrolytes. 48

Figure 4.8 Electrochemical applications of Mo_3C_2. 49

Figure 5.1 Illustration of a prototype origami structure made by the laser direct conductive electrodes on a non-conductive paper substrate. 55

Figure 5.2 Sheet resistance of samples after the laser ablation process. 57

Figure 5.3 SEM and TEM image of paper at different regimes. 58

Figure 5.4 Conductivity of converted paper electrode in different conditions. 58

Figure 5.5 Electron dispersion spectrum of MG-paper converted from different polymer gel.. 58

Figure 5.6 SEM images of MG-paper converted from different types of paper, with different fabrication parameters.. 59

Figure 5.7 Paper-based electret generator I. 61
Figure 5.8 Paper-based electret generator II 62
Figure 5.9 A double side converted and folded paper triboelectret generator. 62
Figure 5.10 Supercapacitor made by laser converted paper electrodes. 63
Figure 5.11 Optical images of a paper-based interdigitated supercapacitor before and after the conversion to conducted MG-paper. 63
Figure 5.12 Other foldable electronic application based on the MG-paper: heavy metal ion detection; gas sensor and pulse wave sensor. 65
Figure 6.1 The schematic diagram for the large-scale synthesis of MoS_2 by the self-assembly of gelatin scaffold. 68
Figure 6.2 Characterization of synthesized single crystalline large scale MoS_2 thin film with a thickness of about 2 μm. 70
Figure 6.3 Characterizaiton of few layer MoS_2 grown from diluted thiosalt of Mo. 71
Figure 6.4 Characterizaiton of few layer MoS_2 grown from diluted MoO_4^{2-} and its optical properties. 72
Figure 6.5 Stacking layers of MoS_2. 73

List of Table

Table 2.1 Summary of graphene synthesis results by the droplet CVD process 16

Table 3.1 TiS_2 composite-VACNT electrodes in different electrolytes. (NMP: N-Methyl-2-pyrrolidone) 34

Table 3.2 Comparisons of state-of-art high capacitance, high energy density materials..... 35

Table 4.1 Current $M_{n+1}AX_n$ phases, ("211", "312", and "413") and valence electron configuration for the M and A elements[7]. 40

Table 4.2 Summary of the composition of various tested hydrogels and their obtained products with laser ablation..... 46

Acknowledgments

First, I would like to thank my research advisors, Professor Liwei Lin for introducing me to the field of Micro Electromechanical Systems. Professor Lin gave me all kinds of freedom and encouragement which enabled me to continue doing materials orientated research in a MEMS group. I would also thank Prof Costas Grigoropoulos and Prof Jie Yao for being on my thesis committee; Prof Chris Dames and Holger Müller for being on qualify committee and sharing inspiring comments. Several other professors have contributed graciously on my behalf: Prof Daryl Chrzan discussed the exfoliation of MoS_2 and the interlayer coupling; Prof Alex Zettl and Prof Junqiao Wu share their Raman instrument which is essential for 2D materials characterization.

During the years in Berkeley, I met many great collaborators who have been working in different style with me: Dr Mohan Sanghadasa support the research in 2d materials energy storage; Dr Adam Schwartzberg (molecular foundry) helped me to develop the synthesis routine of TiS_2 by ALD; Dr Nathan Hohman (molecular foundry) collaborate with me on developing large scale assembly of 2D MoS_2; Dr Jim Schuck (molecular foundry) provide the opportunity to work on advanced optical measurement in foundry; and Dr Jeff Urban introduced his phd to help me with MOF work.

I would also like to thank all the facility staffs for their professional service and gracious help, including staffs in Marvel Nanolab, BNC and Stanford Nanolab. Especially many staff scientists in LBNL generously help me on non-trivial characterizations with greatly deepen my understanding of 2D materials: Dr Michael Brady (ALS) helped me using beamline 7.3.3 to characterize GIWAXS; Dr Nobumichi Tamura helped to use 12.3.2 mapping single crystal; Dr Tev Kuykendall and Miss Tracy Mattox trained me on XRD, UV-VIS and PL in the inorganic facilities of molecular foundry; Miss Liana Klivansky helped me gas absorption BET tests.

I would also like to thank a lot of former senior lab members for their generous help: Dr Qin Zhou (University of Nebraska Lincon) and Dr Yingqi Jiang (Analog Device Inc) both collaborate with my on research the provide guide when I just arrive at Berkeley; Dr Roseanne Warren trained me on CVD and electrochemical work stations and provided me RuO_x samples after she moved to Utah University; Dr Jiyoung Chang (Utah University) helped me with AFM analysis; Mr Kaiyuan Yao contribute a lot on the optical characterization of MoS_2 samples; Dr Kwok Siong Teh revised a couple of my paper draft and proposals; Dr Hyungseok Jang work on one paper together; Dr Hyun Sung Park helped with device analysis. I would also sincerely thank many of current lab fellows: Dr Junwen Zhou, Dr Minsong Wei, Mr Caiwei Shen, Miss Emmeline Kao, Mr Yumeng Liu, Mr Takeshi Hayasaka, Miss Yao Chu, Mr Eric Sweet, and Mr Huiliang Liu all helped me on different experiments or facilities. There are also quite a few visiting students/scholars I have been effectively working together with: Mr Follmar Mateo (ETH) on metal carbide project; Dr Guoxi Luo on electrospinning project; Mr Buxuan Li on carbide and paper electronics projects. There are also many research fellows on Berkeley campus and BSAC who have contributed discussion, ideas and hands on help to who I would like to express my deep thanks: Dr Aiming Yan in physics department and Mr Penghong Ci in Prof Wu's

group both helped with Raman measurement; Mr Ruopeng Zhang in Prof Minor's group helped with TEM imaging.

I sincerely thank my parents for their support, patience and unconditional love. Finally, I would like to thank my husband Dr J-H X for getting his PhD two years earlier than me which greatly motivate me to work harder to graduate sooner. I want the Doctor title on my flight ticket too!

1 Chapter: Introduction

The foresight speech, titled "There's plenty of room at the bottom" was given nearly 60 years ago by Professor Richard Feynman (Nobel Laureate in Physics) in 1959 and generations of scientists have worked toward the miniaturizations of size of devices[1]. Stemming from the development of microfabrication, the trends in research of microelectronics and microelectromechanical systems (MEMS) have been pushing towards nanoelectromechanical and nanoengineering[2]. With the push of lithography down to a few nano-meter, the expanding of Moore's law requires new approach[3]. The discovery of lower dimensional materials, including 1D nanowires and nanotubes[4] and 2D graphene introduce new directions and inspirations. Especially, after the first demonstration of field effect transition by the two-dimensional, single layer graphene[5], the research of low dimensional materials and devices has increased explosively[6]. On the other hand, two dimensional materials, including graphene[6], 2D transition metal Xenes[7], transition metal carbide (TMC)[8, 9] and transition metal dichalcogenide (TMDC)[10, 11], have been expanding the knowledge of material scientists, condense matter physicians, and chemists[12]. Specially, the 2D density of states, phonon dispersion and high layer dependency induce a lot interesting and non-trivial electronical[13, 14], optical[15] and chemical properties[16].

1.1 Application of 2D materials

Graphene has been reported with the highest Young's modulus (2000 ± 400 GPa) and tensile strength (130 ± 10GPa), for applications such as electromechanical resonators based on their resonance frequency changes[17]. Exceptional carrier mobility in the monolayer graphene (2×10^5 $cm^2V^{-1}S^{-1}$) motivates great amounts of research to apply graphene in electronics in field effect transistors, RF communications, ambipolar nonlinear electronics, photodetectors … etc[18]. Besides graphene, which has the van Hove singularity at the Dirac point but lack of the true bandgap[19], monolayer transition metal dichalcogenides with layer-dependent bandgap and sub-nanometer thickness could become promising materials in analog devices[20]. So far ultrasmall FET has been demonstrated on MoS_2, showing down to 1 nm gate length to employ a single wall carbon nanotube (CNT) as the gate[21]. Meanwhile, the merits of transition metal chalcogenide chemical properties, including rich edge state, highly anisotropic surface chemistry, and intercalation with Li^+ ions[22], also motivate their applications in chemical sensors, catalysis in desulfurization and hydrogen evolution, and energy storage electrodes[16]. With the hydrogen evolution capability nearly comparable to Platinum, the low cost MoS_2 is more competitive to bring new solutions to fuel cell related reaction catalysts[23].

2D transition metal carbides, the other family of 2D materials, have been attracting interests only recently after graphene and TMDC as their intrinsic structures don't have the weak interlayer interactions for possible direct exfoliation of the layer-by-layer structure. Only in recent years, materials scientists have fabricated the 2D transition metal carbides by etching the interlayer of the MAX phase ceramics and isolate them down to a few nanometer sheets with the protection of the surface -OH, -O and OOH groups[24]. A beauty and intuitive name, MXENE, was given to this family of materials. With the exceptional high surface area, conductivity and surface functional

groups, MXENE has produced the highest volumetric capacitance (~900 F/cm^3) to the best of our knowledge with a great potential for fast charge-discharge energy storage applications[25].

1.2 Synthesis of 2D materials

Like many of the accidental discovery in the history of science, the first 2D material is made by the mechanical exfoliation from graphite in pencil using a scotch tape[26]. Even though this manual method results high quality graphene, the human labor cost and deficiency in scale fabrication motivate the development of new methods including chemical vapor deposition (CVD), epitaxial growth (on SiC substrates), chemical reduction of graphene oxide, and precipitation of carbon[17]. Similarly, the fabrication methods for TMDC include the mechanical exfoliation from crystals[27], solution based reactions[28], chemical vapor deposition[11], atomic layer deposition (ALD) [29], … etc. As a newly emerged family of TMDs, there are only limited synthesis processes such as the MAX phase etching process[30] and chemical vapor deposition[31]. While the research into 2D materials synthesis has achieved fruitful results, large scale fabrication is still missing for mass productions. For example, wafer-level deposition of single layer MoS_2 could only be achieved by the MOCVD which is highly restricted and expensive[11].

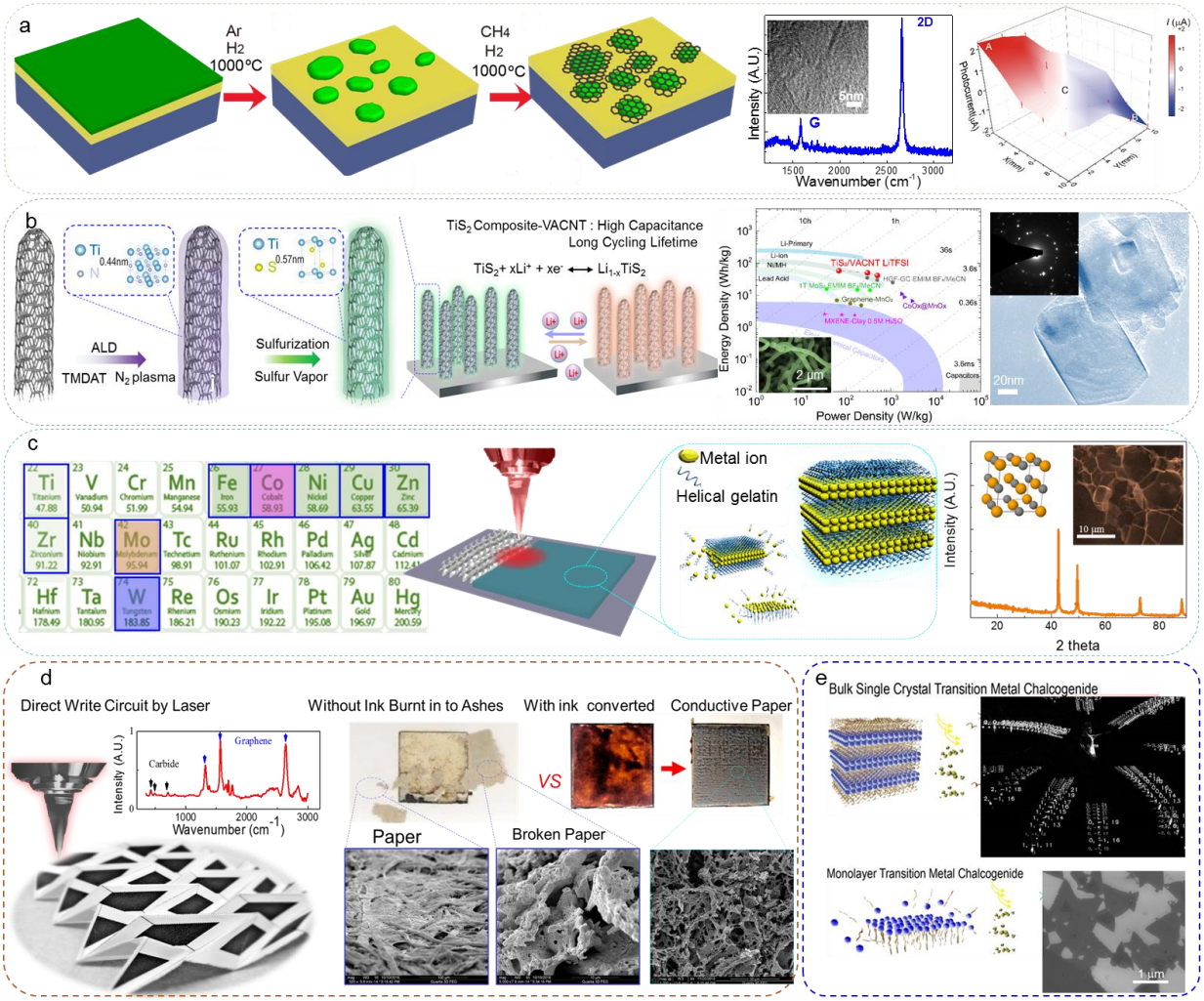

Figure 1.1 illustrating different method for 2D materials synthesis. (a) Monolayer graphene grown on melt and reflowed nickel droplets, which is applied for photo thermal electricity. (b) Atomic layer deposition-sulfurization process employed to coated uniform TiS2 onto high aspect ratio carbon nanotubes, leading high specific energy density in lithium rich electrolyte (21m LiTFSI). (c) CO2 laser induced transition metal carbides from gelatin mediated transition metal ions(Mo5+/W6+/Co2+) templates. (d) Foldable paper electrodes converted from paper rinsed by Mo-gelatin ink, without which paper will be burnt into ashes. (e) Surfactant assisted assembly of MoS2 single crystal and few layer structure, thickness of which is decided by precursor concentration.

1.3 Structure of the dissertation

This dissertation present new methodologies for the synthesis of 2D materials, aiming at large scale, uniform depositions of graphene, TMDC and TMC with controllable layers and dimensions. The key processes and results are summarized in **Figure 1**. Chapter 2 discusses the growth of

graphene based on microscale liquid metal droplets and the feasibility to use the grown structure directly as photodetectors without the common graphene transfer process[32] (**Figure 1a**). Chapter 3 illustrates a hybrid ALD/sulfurization process to uniformly decorate TiS_2 composites onto vertical aligned CNT forests and the demonstrations of ultrahigh energy density pseudo-capacitors using high concentration Li-ion electrolytes (**Figure 1b**). Chapter 4 discussed laser ablation method to synthesize 2D transition metal carbides and their applications in energy storage (**Figure 1c**). Such process is versatile with a Mo/W/Co precursors, assembled in 2D favor mediated by the triple helix polymer. Chapter 5 discusses the expansion of the laser processed 2D metal carbide on paper for the direct print of flexible electronics on paper for various applications (**Figure 1d**). Chapter 6 introduces a polymer assisted self-assembly process for large scale synthesis of MoS_2 films, which shows monolayer-type photoluminescence with the multiple layer structure isolated by interlayer polymer templates (**Figure 1e**). Chapter 7 concludes the research work and provides outlooks for future directions.

References

1. G. E. Moore, *Proceedings of the IEEE*, 1998, **86**, 82-85.
2. M. Despont, J. Brugger, U. Drechsler, U. Durig, W. Haberle, M. Lutwyche, H. Rothuizen, R. Stutz, R. Widmer, G. Binnig, H. Rohrer and P. Vettiger, *Sensor Actuat a-Phys*, 2000, **80**, 100-107.
3. T. Roy, M. Tosun, J. S. Kang, A. B. Sachid, S. B. Desai, M. Hettick, C. M. C. Hu and A. Javey, *Acs Nano*, 2014, **8**, 6259-6264.
4. S. J. Tans, A. R. M. Verschueren and C. Dekker, *Nature*, 1998, **393**, 49-52.
5. A. K. Geim and K. S. Novoselov, *Nature Materials*, 2007, **6**, 183-191.
6. Z. H. Sun and H. X. Chang, *Acs Nano*, 2014, **8**, 4133-4156.
7. A. Molle, J. Goldberger, M. Houssa, Y. Xu, S. C. Zhang and D. Akinwande, *Nature Materials*, 2017, **16**, 163-169.
8. M. Naguib, V. N. Mochalin, M. W. Barsoum and Y. Gogotsi, *Advanced Materials*, 2014, **26**, 992-1005.
9. M. Ghidiu, M. R. Lukatskaya, M. Q. Zhao, Y. Gogotsi and M. W. Barsoum, *Nature*, 2014, **516**, 78-U171.
10. S. Das, J. A. Robinson, M. Dubey, H. Terrones and M. Terrones, in *Annual Review of Materials Research, Vol 45*, ed. D. R. Clarke, 2015, vol. 45, pp. 1-27.
11. K. Kang, S. Xie, L. Huang, Y. Han, P. Y. Huang, K. F. Mak, C.-J. Kim, D. Muller and J. Park, *Nature*, 2015, **520**, 656-660.
12. G. Fiori, F. Bonaccorso, G. Iannaccone, T. Palacios, D. Neumaier, A. Seabaugh, S. K. Banerjee and L. Colombo, *Nat Nanotechnol*, 2014, **9**, 768-779.
13. W. M. Hu, S. Y. Ren and J. D. Dow, *Phys Rev B*, 1981, **24**, 6156-6157.
14. A. Kormányos, G. Burkard, M. Gmitra, J. Fabian, V. Zólyomi, N. D. Drummond and V. Fal'ko, *2d Mater*, 2015, **2**, 022001.
15. J. Xiao, M. Zhao, Y. Wang and X. Zhang, *Journal*, 2017, **0**.
16. M. Chhowalla, H. S. Shin, G. Eda, L. J. Li, K. P. Loh and H. Zhang, *Nat Chem*, 2013, **5**, 263-275.
17. X. N. Zang, Q. Zhou, J. Y. Chang, Y. M. Liu and L. W. Lin, *Microelectron Eng*, 2015, **132**, 192-206.
18. T. Palacios, *Nat Nanotechnol*, 2011, **6**, 464-465.

19. J. L. McChesney, A. Bostwick, T. Ohta, T. Seyller, K. Horn, J. Gonzalez and E. Rotenberg, *Phys Rev Lett*, 2010, **104**.
20. H. Wang, L. L. Yu, Y. H. Lee, Y. M. Shi, A. Hsu, M. L. Chin, L. J. Li, M. Dubey, J. Kong and T. Palacios, *Nano Lett*, 2012, **12**, 4674-4680.
21. S. B. Desai, S. R. Madhvapathy, A. B. Sachid, J. P. Llinas, Q. X. Wang, G. H. Ahn, G. Pitner, M. J. Kim, J. Bokor, C. M. Hu, H. S. P. Wong and A. Javey, *Science*, 2016, **354**, 99-102.
22. G. A. Muller, J. B. Cook, H. S. Kim, S. H. Tolbert and B. Dunn, *Nano Lett*, 2015, **15**, 1911-1917.
23. D. H. Deng, K. S. Novoselov, Q. Fu, N. F. Zheng, Z. Q. Tian and X. H. Bao, *Nat Nanotechnol*, 2016, **11**, 218-230.
24. M. Naguib, O. Mashtalir, J. Carle, V. Presser, J. Lu, L. Hultman, Y. Gogotsi and M. W. Barsoum, *Acs Nano*, 2012, **6**, 1322-1331.
25. M. R. Lukatskaya, S. Kota, Z. Lin, M.-Q. Zhao, N. Shpigel, M. D. Levi, J. Halim, P.-L. Taberna, M. W. Barsoum, P. Simon and Y. Gogotsi, 2017, **6**, 17105.
26. K. S. Novoselov, A. K. Geim, S. V. Morozov, D. Jiang, Y. Zhang, S. V. Dubonos, I. V. Grigorieva and A. A. Firsov, *Science*, 2004, **306**, 666-669.
27. J. N. Coleman, M. Lotya, A. O'Neill, S. D. Bergin, P. J. King, U. Khan, K. Young, A. Gaucher, S. De, R. J. Smith, I. V. Shvets, S. K. Arora, G. Stanton, H. Y. Kim, K. Lee, G. T. Kim, G. S. Duesberg, T. Hallam, J. J. Boland, J. J. Wang, J. F. Donegan, J. C. Grunlan, G. Moriarty, A. Shmeliov, R. J. Nicholls, J. M. Perkins, E. M. Grieveson, K. Theuwissen, D. W. McComb, P. D. Nellist and V. Nicolosi, *Science*, 2011, **331**, 568-571.
28. F. Wang, J. H. Seo, G. F. Luo, M. B. Starr, Z. D. Li, D. L. Geng, X. Yin, S. Y. Wang, D. G. Fraser, D. Morgan, Z. Q. Ma and X. D. Wang, *Nat Commun*, 2016, **7**.
29. N. P. Dasgupta, X. B. Meng, J. W. Elam and A. B. F. Martinson, *Accounts Chem Res*, 2015, **48**, 341-348.
30. O. Mashtalir, M. Naguib, V. N. Mochalin, Y. Dall'Agnese, M. Heon, M. W. Barsoum and Y. Gogotsi, *Nature Communications*, 2013, **4**.
31. Y. Gogotsi, *Nat Mater*, 2015, **14**, 1079-1080.
32. X. N. Zang, Q. Zhou, J. Y. Chang, K. S. Teh, M. S. Wei, A. Zettl and L. W. Lin, *Adv Mater Interfaces*, 2017, **4**.

2 Chapter: Synthesis of Single Layer Graphene on Nickel Using a Droplet CVD Process

Keywords: Graphene, Single layer, Droplet CVD, Chemical Vapor Deposition; Photocurrent

2.1 Abstract

A liquid metal "droplet" chemical vapor deposition (CVD) process is developed for the synthesis of single-layer graphene flakes utilizing molten nickel droplets (nominal diameter from 0.5 to 1μm) as the catalysts. Ultrathin nickel films melt and reflow to form nickel droplets at around 1000°C, providing liquid-phase, single-grain catalytic sites for the nucleation of graphene flakes via the carbon precipitation process. Due to the high surface area-to-volume ratio of these sub-micron sized nickel droplets, the precipitated carbon favors the formation of single-layer graphene. Experimentally, both single- and double-layer graphene flakes with low defects have been synthesized by using nickel thin films of either less or more than 100nm (up to 130nm) in thickness, respectively. The domain sizes of as-synthesized graphene flakes are found to be slightly larger than those of the underlying droplets, suggesting the outgrowth of graphene in the synthesis process. Furthermore, the synthesized graphene flakes are hybridized strongly by the nickel orbitals as suggested by a density function analysis and experimentally observed blue shifts in Raman spectra tests. When the original nickel thin film is 75 nm in thickness, the resulting nickel droplets are physically and electrically isolated, while after the CVD synthesis process, the graphene flakes are found to be electrically connected probably due to the outgrowth of graphene from the separated nickel droplets. These electrically-connected graphene sheets could be readily available for device applications without the need of transfer processes. In this work, we demonstrate the direct generation of photocurrents (up to 0.53 μA/mm2·W) due to the photo-thermal effect based on as-fabricated graphene sheets under a visible light source.

2.2 Introduction

The fabrication processes as well as the properties of graphene have been widely studied in recent years toward numerous device applications[1, 2]. Mechanical cleavage[3], epitaxial growth on SiC[4], chemical vapor deposition (CVD)[5], carbon precipitation from metals[6], and various other approaches[7-9] have all produced graphene. Among them, the CVD process using nickel or copper as the catalysts is the most promising approach for large area production and low manufacturing cost[10, 11]. It has been reported that the excess carbon near the grain boundaries of catalysts may result in defects on the resulting graphene[5]. As such, carbon solubility and grain boundary of the catalysts are two key factors affecting the resulting graphene quality. Previously, liquid metal catalysts have been studied in the CVD process to reduce the crystal lattice of catalysts for the synthesis of high quality graphene[12] and a large melted copper droplet (centimeter in size) has been tested to grow single layer graphene at 1150°C[13, 14]. Here, instead of using large-size droplets, ultra-thin metal films (20-130 nm in thickness) have been utilized as the starting structures to form small-size droplets at a temperature lower than the melting temperature of the bulk catalyst materials due to the melting point depress effect[15]. Using Nickel as an example, the droplet CVD process is processed at a temperature of around 1000°C[16] – much lower than the nickel melting

temperature at 1460°C. In the case of copper, its low wettability on the silicon oxide surface could result in deformation and folding of graphene on the copper droplets and the ultralow solubility of carbon in copper could increase the defects in graphene[14, 17, 18].

2.3 Results and Discussion

The "droplet CVD" process was used to synthesize single layer graphene flakes by using nickel as the catalyst. First, a thin nickel film was deposited by means of evaporation to control the film thickness on a silicon substrate with a SiO_2 layer (300 nm in thickness) pre-deposited as the insulation layer (**Figure 2.1a**). The high temperature environment caused the nickel film to melt and become droplets (**Figure 2.1b**). During the CVD process, we used 5 sccm of CH_4 as the carbon source, 50 sccm of H_2 and 300 sccm of Argon as the carrier gases with a processing temperature of 1000°C. Graphene flakes were formed on the top surface of the nickel droplets (**Figure 2.1c**). **Figures 2.1d** and **2.1e** are two SEM (scanning electron microscopy) images showing the synthesis results from the 40 nm-thick nickel films without and with the carbon source gas, respectively. As grown graphene sheets using the nickel droplet process is transferred by using PMMA onto a quantifoil TEM grid[19], and attached onto the amorphous carbon support, as shown in **Figure 2.1h** and **2.1i**. Since the graphene sheet on the nickel droplet is not completely flat, deformation and folding are induced as shown in the zoom in TEM image, atomic fringes are still observable, shown in **Figure 2.1j**. Raman spectrum taken directly on the TEM grid sample in **Figure 2.1k** shows the finguerprint of monolayer graphene: a primary in-plane vibrational mode G peak, disorder induced D peak, and double phonon second-order different inplane vibration 2D peak at 1580, 1350, and 2700 cm^{-1}, respectively[20]. The G/2D ratio favors an implication of monolayer when it is lower than 0.5, of double layer when it is between 0.5 to 1, and of multi-layer when it is higher than 1[21].

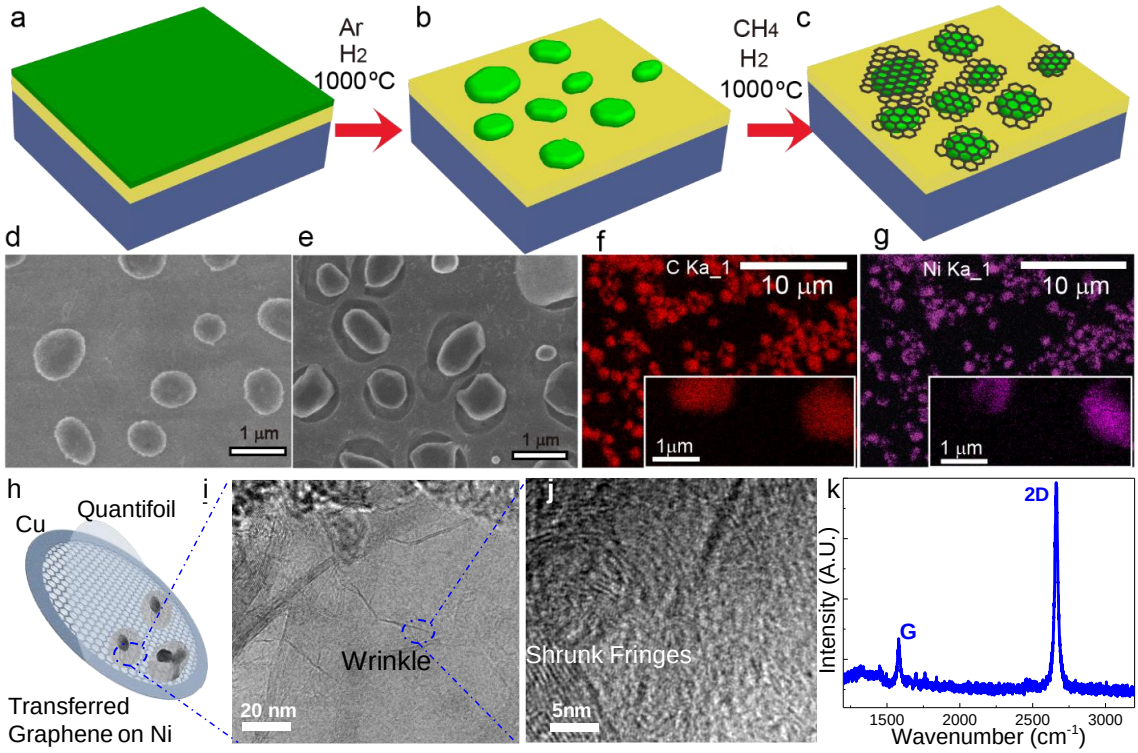

Figure 2.1 (a)-(c) Schematics showing the droplet-based CVD process: (a) deposition of a thin nickel film on the top of a silicon substrate covered by an insulating SiO_2 layer; (b) melting of the nickel to form droplets under a high processing temperature; and (c) synthesis of graphene on the nickel droplets using methane as the carbon source. SEM images of the fabricated nickel droplets after the CVD process: (d) without adding the carbon source; and (e) with the carbon source to synthesize graphene. (f, g) EDS image mapping of C_Kα1 and Ni_Kα1, respectively, showing the carbon distribution. Insets are enlarged views. (h-k) direct characterization of graphene synthesized on nickel droplets by transferring them onto a TEM grid. Quantifoil is a layer of ultrathin amorphous carbon with a grid size of 2 μm to hold the microscale graphene sheets. (i) TEM image of the transferred graphene. (j) Zoom in image of showing some areas with atomic fringes due to the deformation of graphene in the transfer process. (k) Raman spectrum on the quantifoil showing single layer graphene structures

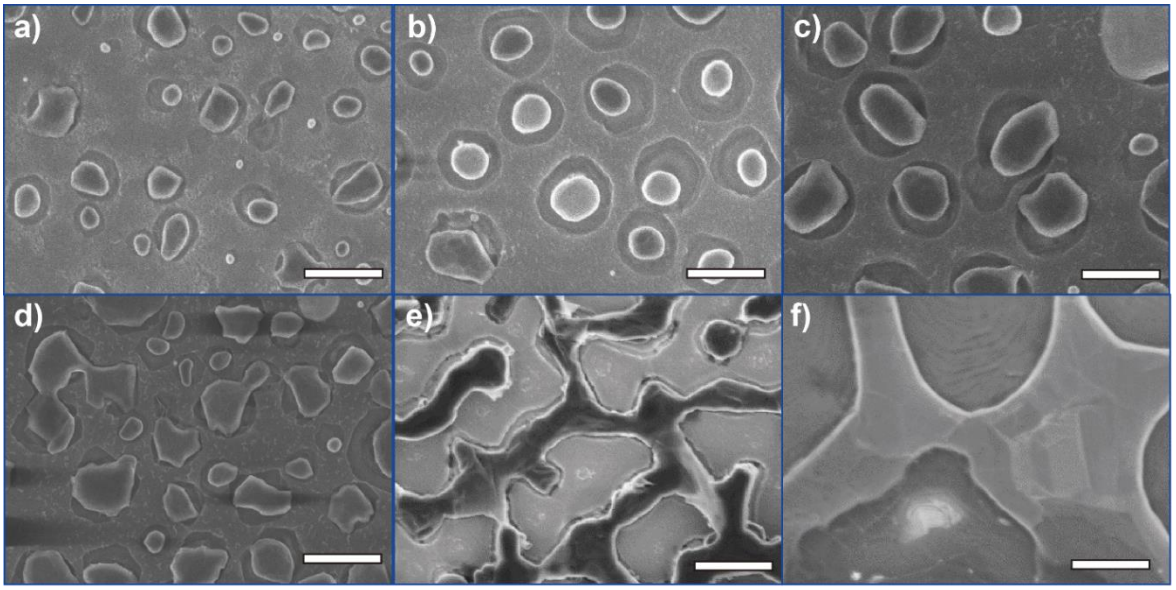

Figure 2.2 SEM images showing the size and distribution of nickel droplets after the droplet CVD process to synthesize graphene with initial film thicknesses of (a) 20; (b) 30; (c) 40; (d) 50; (e) 75; and (f) 105nm, respectively.

We tested a series of sputtered nickel thin films (1×1 cm^2 in size) with different thicknesses of 20, 30, 40, 50, 75, 105, and 130 nm for the droplet CVD process. The increase in film thickness resulted in the increase in the droplet size and the decrease in the gap distance between individual droplets (**Figure 2.2 a-f**). The average Raman spectra (10 points) of the as-fabricated samples are plotted in **Figure 2.3a** and their I_G/I_{2D} values versus film thickness are summarized in **Figure 2.3b**. It is observed that graphene flakes on nickel films with initial thickness of 20-75 nm have the characteristics of single layer as I_G/I_{2D} is less than 0.5 and I_D is low. When the initial nickel film thickness is equal or larger than 105 nm, the as-fabricated graphene flakes have I_G/I_{2D} values larger than 0.5 with the characteristics of more than one layer of graphene. For the case of the 300nm-thick nickel foil, multilayer graphene was characterized with broader 2D peak intensity and a slightly increased 2D peak intensity shift than results from samples starting with thin nickel films. The inset in **Figure 2.3b** shows the G peak intensity distributions mapping of 4×4 μm^2 on an as-fabricated sample with initial nickel film thickness of 50nm (both D peak intensity and 2D peak intensity Raman spectra mapping results are shown in **Figure 2.4a-b**). The arrows indicate the possible sites of individual nickel droplets. Coherent with **Figure 2.3b**, the FWHM of the 2D peaks increases as the initial film thickness increases (**Figure 2.5**). It is found that single layer graphene results in the FWHM of 2D peaks smaller than 55 cm^{-1} while double/multi-layer graphene shows splitting in 2D peak. Both D peak intensity and 2D peak intensity Raman spectra mapping results are shown in **Figure 2.4**. The D peak intensity corresponds to disorders/defects, while the 2D peak intensity corresponds to the inter-valley double phonon inelastic scattering.[1] The low intensity areas in **Figure 2.4a** and **2.3b** are areas without graphene.

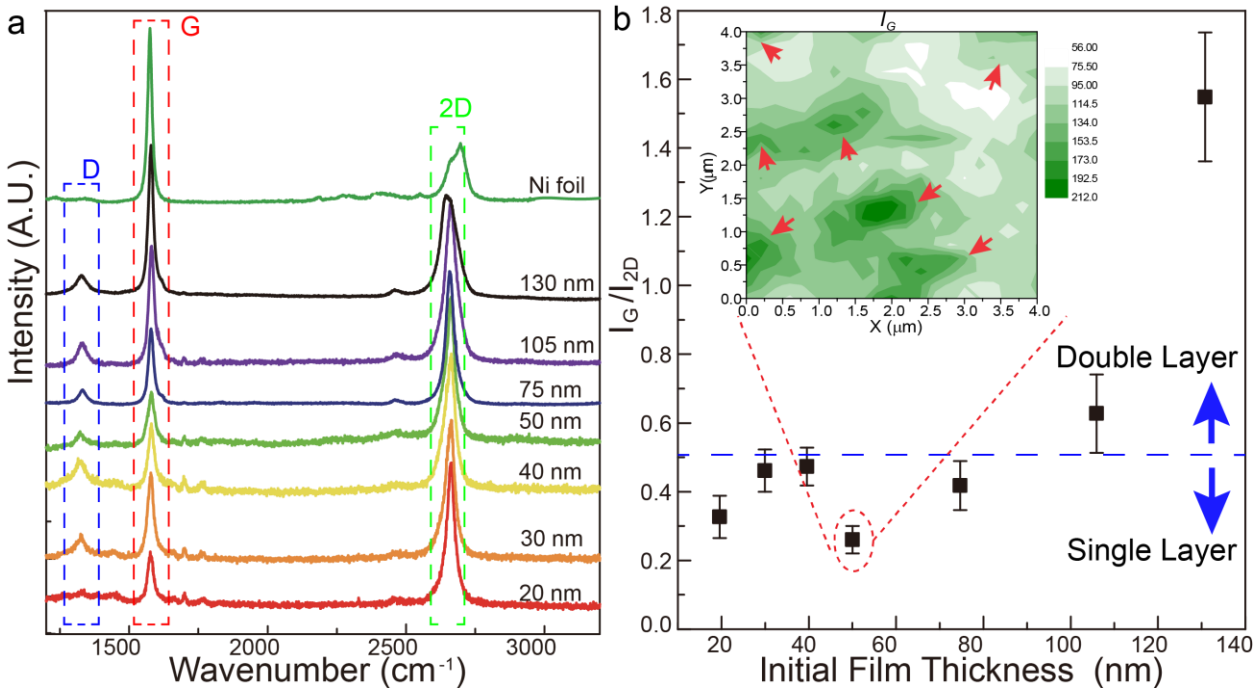

Figure 2.3 (a) Raman spectra corresponding to the droplet-based CVD growth process with initial nickel film thickness of 20, 30, 40, 50, 75, 105, 130 nm, and a 300 nm-thick nickel foil, respectively. (b) IG/I2D versus the initial nickel film thickness calculated from (a). Single layer graphene with low defects (IG/I2D >2 and low ID) was observed when the initial nickel film thickness was less than 105 nm. Double layer graphene was observed when the initial nickel film thickness was equal or larger than 105 nm. Inset: Raman spectra mapping of G peak intensity on a 4×4 □m2 area (initial nickel film thickness of 50nm). Red arrows denote possible nickel droplet sites.

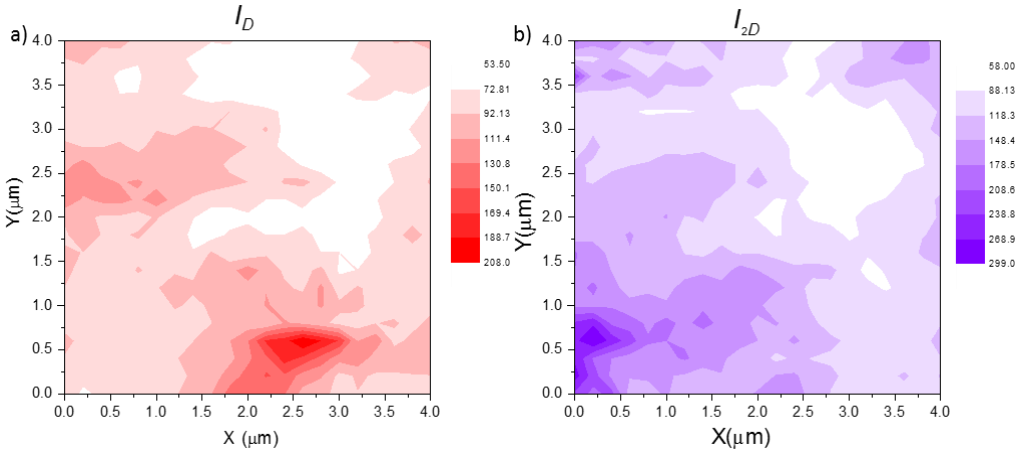

Figure 2.4 Raman spectra mapping results with sample area of 4×4μm^2: (a) I_D – D peak intensity; and (b) I_{2D} – 2D peak intensity.

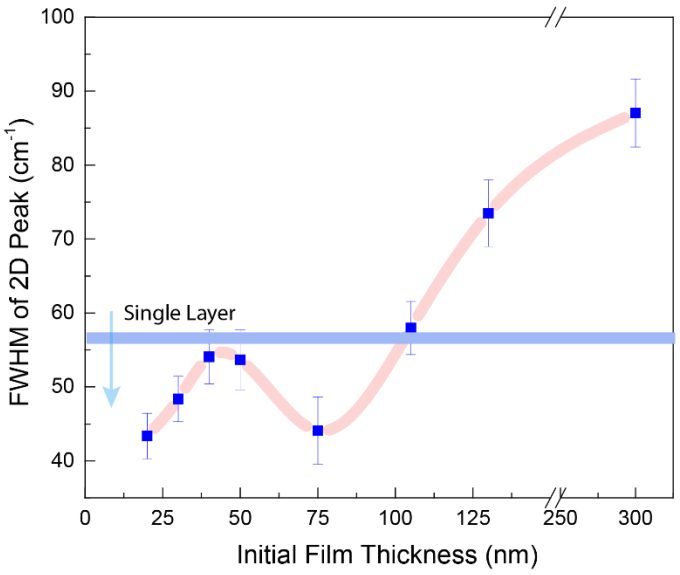

Figure 2.5 2D peak Full Width of Half Maxim (FWHM) of graphene vs initial film thickness. Single layer graphene shows narrower than 55 cm^{-1}.

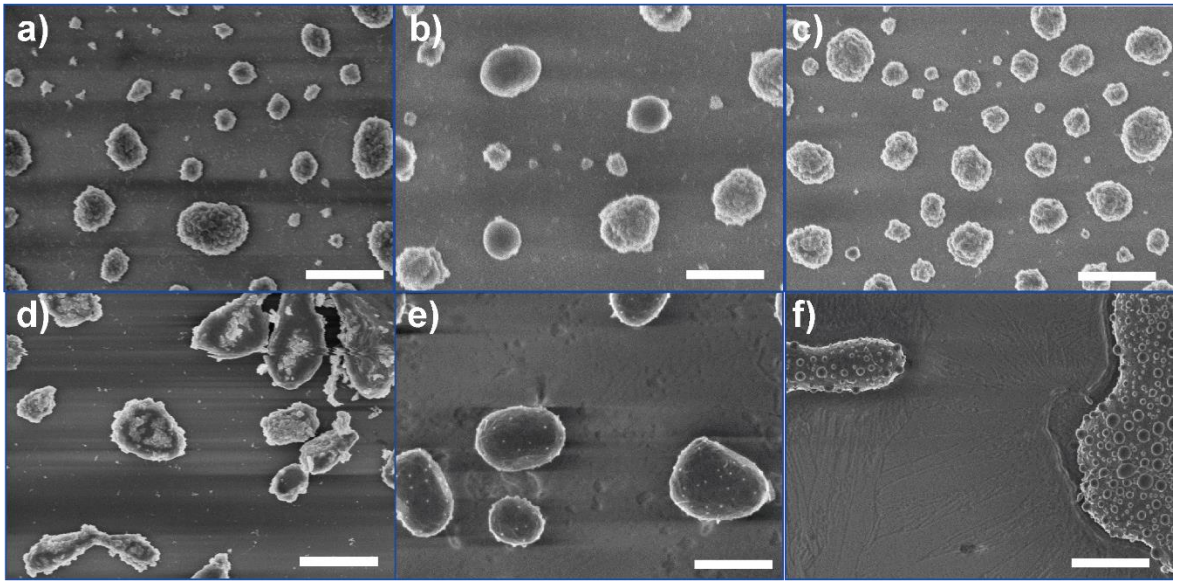

Figure 2.6 SEM images showing the size and distribution of copper droplets after the droplet CVD process to synthesize graphene with initial film thicknesses of (a) 20; (b) 30; (c) 40; (d) 50; (e) 75; and (f) 105nm, respectively.

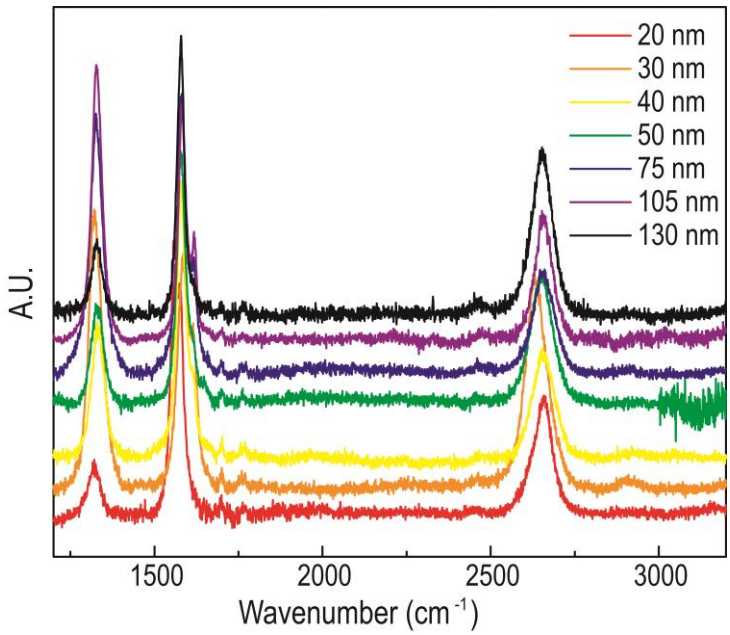

Figure 2.7 Raman spectra corresponding to the droplet-based CVD growth process with initial nickel film thickness of 20, 30, 40, 50, 75, 105, 130 nm.

The size of the droplets increases as the initial copper film thickness increases while the gap between the droplets decreases as shown in **Figure 2.6**. Copper films dewet much more fiercely than Nickel thin films, and graphene sheets wrap and fold on the surface of copper droplets. Graphene grown on copper droplets shows high intensity of D peak in Raman spectra which presents high concentration of defects, as shown in **Figure 2.7**. Graphene sheets deformed and folded badly due to the fierce copper substrate dewet, which also shift the 2D peak due to either defects doping or strain. In summary, the quality of graphene grown on copper is not as high as graphene grown on nickel droplets, especially not feasible to grow continuous large−scale graphene sheet.

It is very difficult to synthesize single layer graphene in the nickel CVD processes as the grain boundaries and thick nickel films provide large amounts of absorbed carbon atoms to result in multilayer graphene. Qualitatively, the small nickel droplets can only absorb limited amount of carbon for the possible formation of single layer graphene flakes. Quantitatively, a simplified model was used to estimate the carbon dissolution and graphene formation in the droplet CVD process. The concentration of carbon is low in the nickel-carbon phase diagram at 1000ºC and an increased value of 0.6% can be identified at the eutectic temperature at 1455ºC[22]. However, the specific carbon solubility in solid state nickel during the droplet CVD process depends on complex factors such as processing temperature, pressure and time. The AFM (Atomic Force Microscope) scanning results on the fabricated nickel droplets in **Figure 2.8** (initial nickel film thickness of 50nm) suggest that nickel droplet and the oxide surface have a contact angle of ~50 degrees (**Figure 2.8b**). Using this information, the adsorbed carbon mass in different sizes of nickel droplets were calculated and plotted with respect to the "apparent" nickel droplet diameter (from the SEM top view images) up to 1.5µm in **Figure 2.8c** based on the carbon solubility from 0.1 to 0.6%. The blue square and green hexagonal symbols are the calculated carbon masses of single

and double layer graphene, respectively, assuming all absorbed carbon masses in the specific size of droplet are precipitated out and uniformly distributed on top of the droplet to form graphene. For low carbon solubility and small nickel droplets, the amount of adsorbed carbon is not enough to form a single layer graphene. On the other hand, high carbon solubility and large nickel droplets can provide enough carbon sources to form single or even multiple layer graphene as observed. **Figure 8d** analyzes the droplet "apparent" diameter versus carbon solubility using calculated single (square symbols) and double (hexagonal symbols) layer graphene mass balance calculations assuming all carbon elements are precipitated out and uniformly distributed on top of the droplets. Below the single layer graphene line, scattered graphene flakes could still be formed to partially cover the surface area. The regions between the single layer and double layer could form single layer graphene. Above the double layer line, double layer or multilayer graphene could be obtained. In all cases, extra carbon sources absorbed by the nickel droplets could be used for the outgrowth of graphene over the bottom nickel droplets.

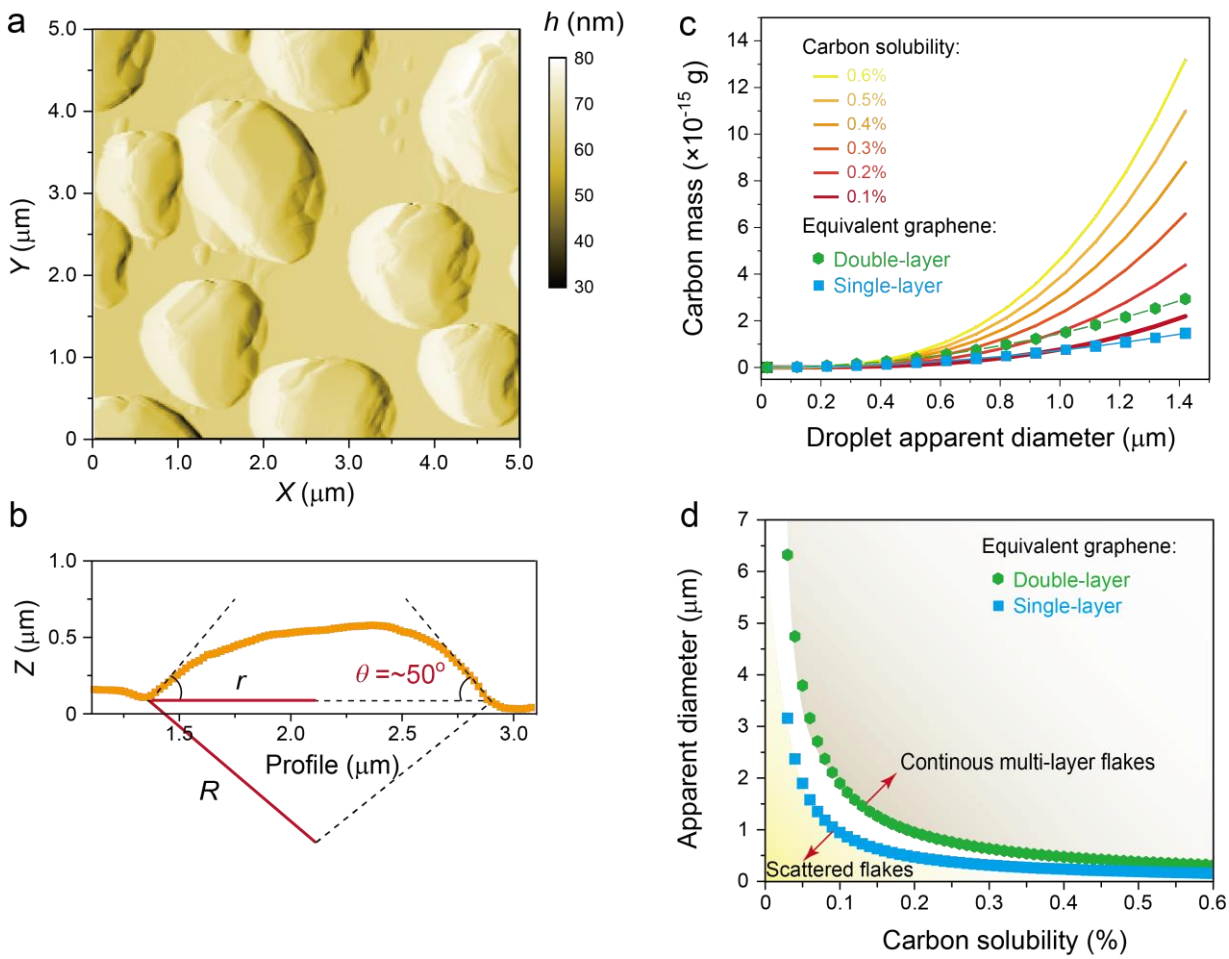

Figure 2.8 (a) AFM scanning result of nickel droplets (initial film thickness of 50 nm) within an area of 5×5 μm^2. (b) A typical droplet height profile from (a) with a 50 degree contact angle between the nickel droplet and the SiO_2 substrate. (c) The absorbed carbon mass versus nickel droplet size with varying carbon solubility in nickel from 0.1%-0.6%. Assuming all absorbed carbon elements are precipitated out and uniform distributed on top of the droplets to form graphene, the mass balance results of single (red square symbols) and double (red hexagonal symbols) layer are calculated and drawn. (d) The droplet size versus carbon solubility plot with

single and double layer graphene using the balance of carbon mass results assuming all absorbed carbon elements are precipitated out and uniformly distributed on top of the droplets to form graphene. Below the single layer line, only scattered graphene flakes can be formed without fully covering the droplet surface. Above the double layer line, double layer or multilayer graphene can be synthesized.

A simplified model is developed to estimate the carbon contents in the droplet CVD process using the basic information and assumptions in **Figure 9a**, including (a) the Ni-C phase diagram[2-3]; (b) the absorbed carbon in the nickel droplet based on the information from (a); (c) full precipitation of carbon to form uniform and full coverage of graphene on the surface of the nickel droplet; and (4) AFM scanning result on the height of the nickel droplets showing measured contact angle, θ, of 50°. Furthermore, the density of Nickel is 7.81 g·cm^{-3} in the calculations; MC is the total mass of carbon; CS is the carbon concentration; R is the radius of the "spherical crown" (droplet on top of the flat surface) derived from the droplet on the surface and contact angle; and d is the "apparent" droplet diameter from direct measurements in SEM images.

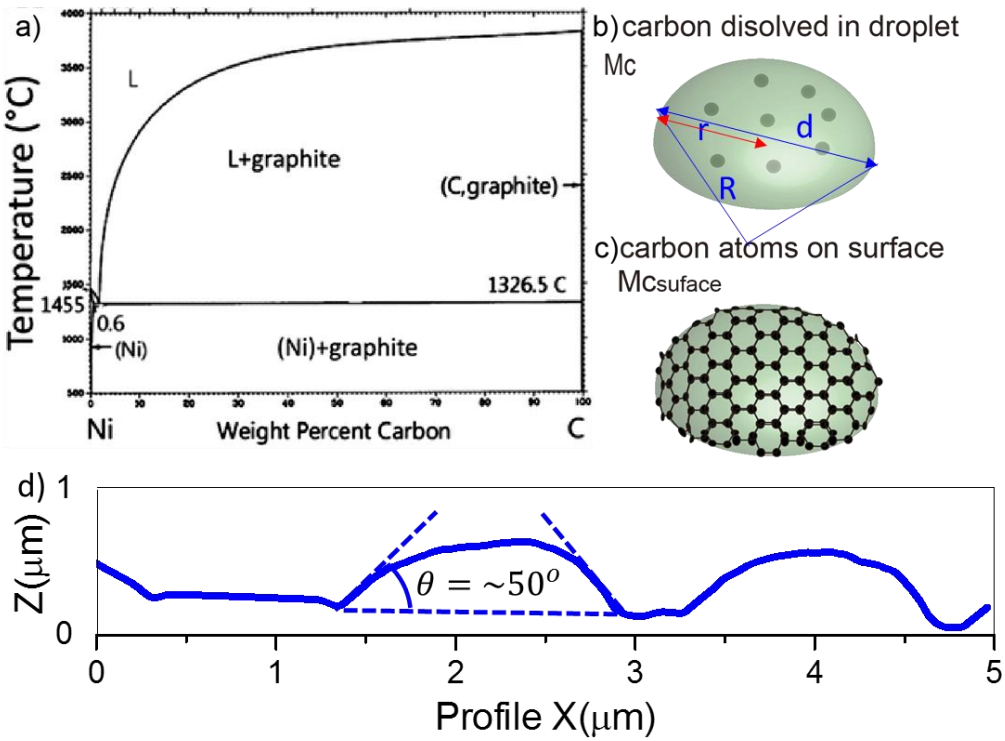

Figure 2.9 Basic information and assumptions: (a) the Ni-C phase diagram; (b) the absorbed carbon in the nickel droplet based on the processing temperature and (a); (c) full precipitation of carbon in the nickel droplet is assumed for full and uniform coverage of graphene on the surface of the nickel droplet; and (d) the surface height profile of nickel droplets from the AFM scanning results. The contact angle between nickel droplet and the SiO_2 substrate is characterized as 50°.

$$R = r/\sin\theta, d = 2r, V = \frac{\pi R^3}{3}(1-\cos\theta)^2(2+\cos\theta) \quad (1)$$

$$Mc = \rho_s C_s V = \rho_s C_s \frac{\pi R^3}{3}(1-\cos\theta)^2(2+\cos\theta) \quad (2)$$

Graphene lattice:

$$\vec{a}_1 = a(\frac{\sqrt{3}}{2}, \frac{1}{2}), \mathrm{a} = 2.46\,\mathring{\mathrm{A}} \quad (3)$$

The mass of a single layer graphene fully covering the top surface of the droplet can be calculated by the surface area. The area of a unit cell of graphene is:

$$A_c = \frac{\sqrt{3}}{2}a^2 = 5.24\times10^{-20}\,\mathrm{m}^2 \quad (4)$$

As shown in **Figure 2.9** , the surface area of a spherical crown is:

$$A_s = 2\pi R^2(1-\cos\theta) \quad (5)$$

The mass of graphene that cover the surface of a droplet is:

$$Mc, surface = \frac{A_s}{A_c} * \frac{2C_{mass}}{N_A} = \frac{A_s}{A_c} * \frac{24g}{6.02*10^{23}} \quad (6)$$

For single layer graphene,

$$R = \frac{6*2*12}{N_a\rho_s} * \frac{1}{(1-\cos\theta)(2+\cos\theta)} \quad (7)$$

$$r = R*\sin\theta = \sin\theta\frac{6*2*12}{N_a\rho_s} * \frac{1}{(1-\cos\theta)(2+\cos\theta)} \quad (8)$$

$$d = 2r = 2R*\sin\theta = 2\sin\theta\frac{6*2*12}{N_a\rho_s} * \frac{1}{(1-\cos\theta)(2+\cos\theta)} \quad (9)$$

For double layer graphene,

$$d' = 2r' = 2R'*\sin\theta = 4R*\sin\theta = 4\sin\theta\frac{6*2*12}{N_a\rho_s} * \frac{1}{(1-\cos\theta)(2+\cos\theta)} \quad (10)$$

Table 2.1 summarizes the synthesis results of different processing parameters in temperature and initial nickel film thickness. Raman spectra were used to determine if graphene flakes were successfully synthesized. It is found that the processing temperature must be higher than 950ºC to synthesize graphene in the droplet CVD process. Furthermore, large film thickness (more than 40nm in the cases of the 950ºC processing temperature) and high temperature (higher than 1000 ºC for high carbon solubility) are favorable to absorb enough carbon sources in the nickel droplets to synthesize graphene. Electrical resistance measurements were performed on samples with or without using the carbon sources in the CVD process. When the nickel film was thinner than 75nm, there was no electrical conductivity for all samples. For the 75nm-thick nickel films, the as-fabricated samples showed a sheet resistance in the range of 100Ω/☐ for the graphene flakes/nickel droplets samples and infinity for the nickel droplets-only samples. This implies that some graphene flakes have outgrown nickel droplets and physically connected to conduct electricity. The outgrowth of graphene over the nickel droplets, which could be the results of: (1) the shrinkage of nickel droplets from liquid to solid, and (2) the high diffusion constant of carbon atoms during the high temperature CVD graphene synthesis process23. For the nickel film with the thickness of 105 nm or larger, results show that nickel droplets were already electrically and physically connected.

Table 2.1 Summary of graphene synthesis results by the droplet CVD process

Thickness	Processing Temperature (°C)							
	600		750		950		1000	
20nm	×	∞	×	∞	×	∞	✓	∞
30nm	×	∞	×	∞	×	∞	✓	∞
40nm	×	∞	×	∞	✓	∞	✓	∞
50nm	×	∞	×	∞	✓	∞	✓	∞
75nm	×	∞	×	∞	☑	Ω	☑	Ω

× no graphene
✓graphene flakes
☑continuous graphene over discontinuous droplets
∞ electrically disconnected
Ω electrically connected

Photocurrent generation measurements were performed at the ambient condition on as-fabricated samples under a probe station. Photon flux of visible light was generated from the light source via the microscope (spot size: 1 mm in diameter; irradiance: 15 W mm^{-2}, **Figure 2.11a**). Two electrical probes were placed at the two opposite diagonal corners of the 1×1 cm^2 chip (**Figure 2.11b**). The light source was turned on and off with an optical chopper. If the light focus was at the center (about the same distance away from the two probe contacts), the magnitude of the photocurrent was nearly zero (blue line in **Figure 2.10a** and marked as "A"). If the light focus was close to the positive electrode, the generated photocurrent was positive ~2 μA (orange line in **Figure 2.10a** and marked as "B"). On the other hand, if the light focus was close to the negative electrode, the generated current was negative ~2 μA. By conducting the same experiments on a sample with single layer graphene from the conventional CVD process and transferred to a silicon substrate with a 285 nm-thick oxide (purchased from graphene supermarket), the photocurrent magnitude was about 2 orders of magnitude smaller than the those with light focus at the positive electrode (black line in **Figure 2.10a** and marked as "C"). We also measured the photocurrent mapping on a 1cm ×1 cm sample with a step size of 0.2 cm as shown in **Figure 2.10b** with the electrodes fixed at the two opposite corners. The symmetry of photocurrent in amplitude and direction with respect to the center line away from the two electrodes supports that temperature gradient is the key for the photocurrent generation. Analytically, the two electrodes can be treated as two heat sinks (big metal structures) maintaining at room temperature during the whole testing process. When the light focus is near the positive electrode, a higher temperature gradient is expected from the light focus to the positive electrode as compared with that from the light focus to the negative electrode. As such, the light focus spots resulted in different temperature gradients on the graphene flakes and the generated photocurrents were symmetrical both in magnitude and direction with respect to the center of the chip. Previously, photocurrents generated by graphene have been reported mainly from two different phenomena: the photovoltaic effect[24] and the photo-thermoelectric effect19. In a further test, it is found that if the on-off frequency of the light source was increased manually, the photocurrent magnitude was decreased with the bases of the photocurrent drifting higher over time (**Figure 2.11c**). These results support that the photothermal effect is the dominating mechanism in the generation of photocurrents.

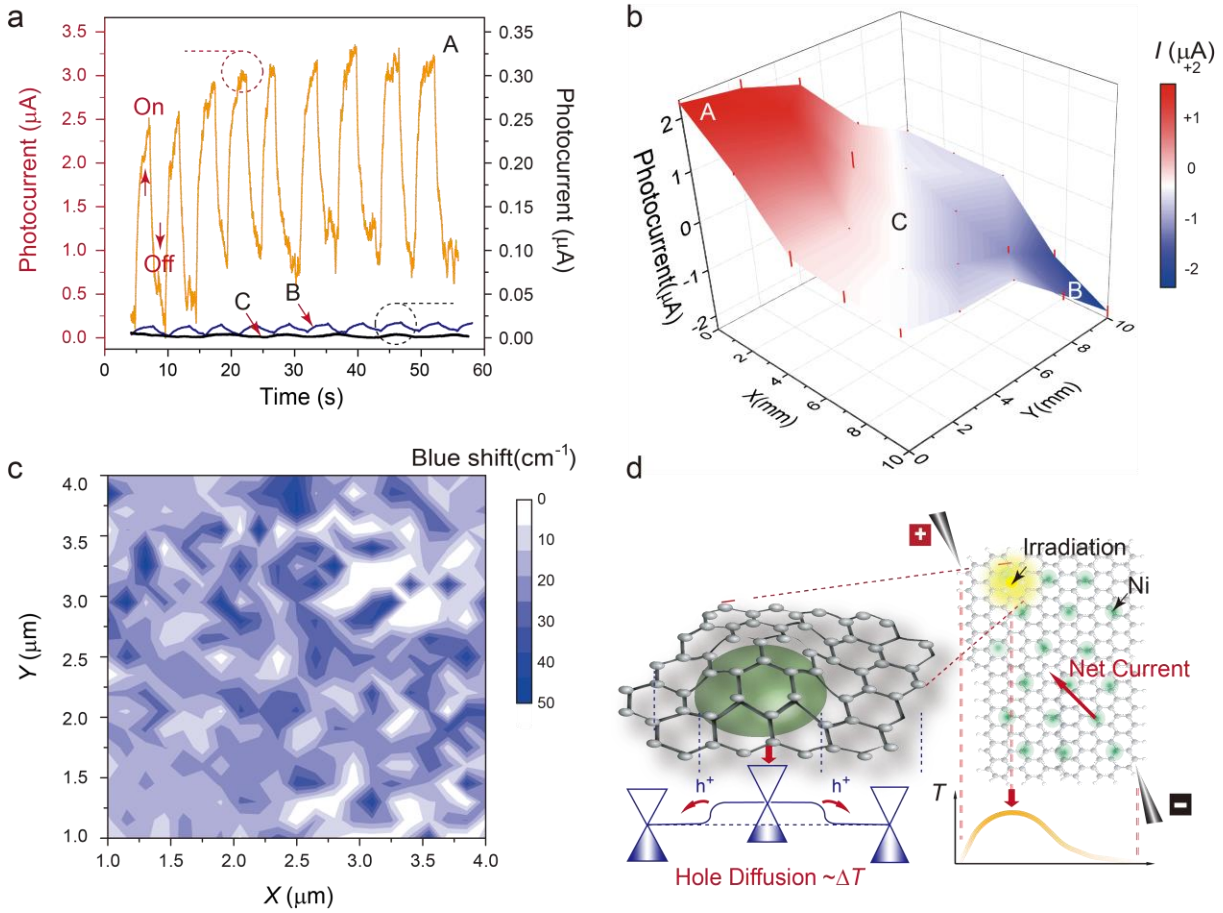

Figure 2.10 The generation of photocurrents on as-fabricated graphene flakes samples after the droplet CVD process with electrodes fixed at the two opposites, diagonal ends of the chip. (a) Photocurrents in response to light illuminations at different light focus points: (A) close to the positive electrode; (B) close to the center of the chip; and (C) from a pristine graphene. Arrows with "on' and "off" symbols are the local maximum and minimum when light is turned on and off, respectively. (b) Mapping results of photocurrents generated on a 1cm×1cm sample. A total of 25 focusing points were tested with locations shown in **Figure 2.11b**. (c) Raman spectra mapping results of the blue shift of the 2D peaks, indicating the hybridization of graphene by nickel. (d) The mechanism of photocurrent generated in graphene by assuming that the generated carriers in the doped graphene follow the average homogenous carrier concentration and hybridization level and a net current is resulted from the applied temperature gradient[25].

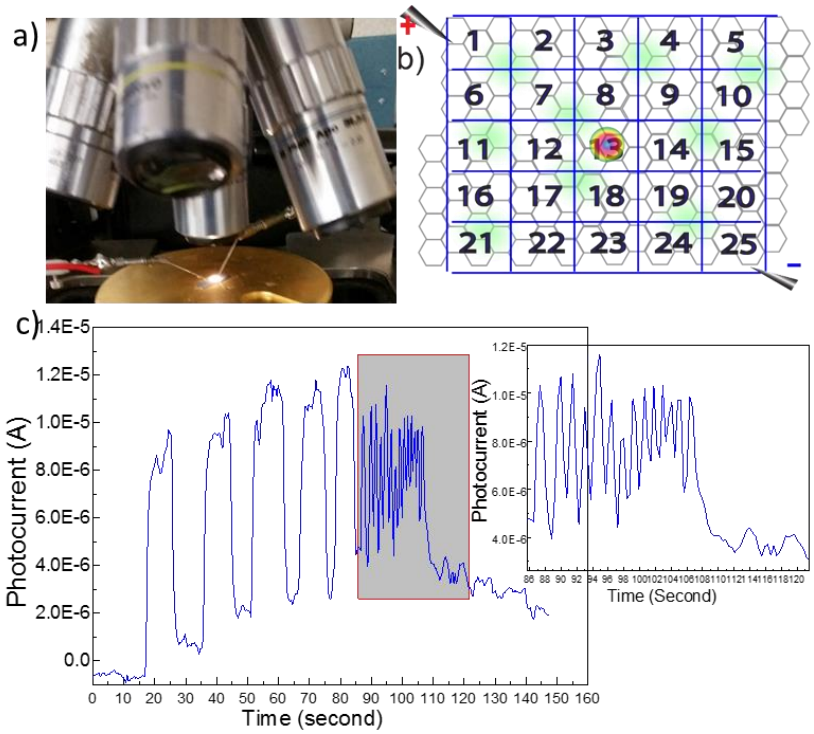

Figure 2.11 Photocurrent characterizations: (a) experimental setup; (b) 25 evenly distributed light focus spots on the sample with the two electrodes placed at the two opposite diagonal corners; (c) photocurrent generations under difference frequencies. Inset: zoom-in view of photocurrents under higher frequency showing lower amplitudes.

The photocurrent testing setup is shown in Figure 2.11. Figure 2.11b shows the locations of the electrodes at the opposite diagonal corners and the evenly distributed 25 light focus spots. When the frequency of the light source was increased manually, the photocurrent magnitude was decreased as shown in Figure 2.11c. Furthermore, the starting points of the photocurrent on each light exposure were drifted higher over time. Both phenomena imply that the thermal effect is the dominating mechanism in the generation of photocurrents.The properties of the synthesized graphene flakes are analyzed. Analytically, graphene and nickel have the work function of 4.5 eV, and 5.0 eV, respectively, and nickel can strongly hybridize the graphene [24]. A numerical simulation was performed based on a density function theory (DFT) using the Atomistix Toolkit [26] and the results showed the negative changes of Fermi level of graphene (Supplementary information, Figure 2.12). Experimentally, Raman spectra tests showed the blue-shift of the 2D intensity peak in Figure 2.10c based on the 75nm-thick initial nickel thin film for the droplet CVD process, implying that the downward movements for the Fermi level of synthesized graphene [20]. We found that the 2D intensity peak of graphene synthesized by the droplet CVD process using different nickel film thicknesses from 20-130 nm all exhibited blue shifts of the 2D intensity peak (Figure 2.12), implying a hybridization for these graphene flakes. Analytically, carriers on these graphene flakes can diffuse due to the temperature gradient [27] and the magnitude of the photothermal current is related to the temperature gradient and charge carrier concentration [25, 28]. Figure 2.10d illustrates the photothermal current generations on the as-fabricated samples, and the built-in junction

between free-graphene and hybridized-graphene separate charged carriers over recombination and thus results in a larger photothermal current. The position of the light focus spot determines the thermal gradients with respect to the two electrodes and controls not only the magnitude but also the direction of the photocurrent as demonstrated in Figure 2.4b. The Fermi level of the graphene-metal contact was simulated in Figure 2.12a. The graphene unit cell was built with a nickel atom, and the band diagrams were calculated with the density function theory (DFT). Results show a downward shift of Fermi level in graphene. Within the geometry limit of 2.2A to 5.0A, graphene shows varying Fermi level down shifts based on the metal-graphene distance in Figure 2.12. The 2D intensity peak and G intensity peak can be used to characterize the shift of fermi level. Figure 2.13 shows the amounts of 2D intensity peak blue shift for the synthesized graphene flakes by the droplet CVD process with respect to the initial nickel film thickness.

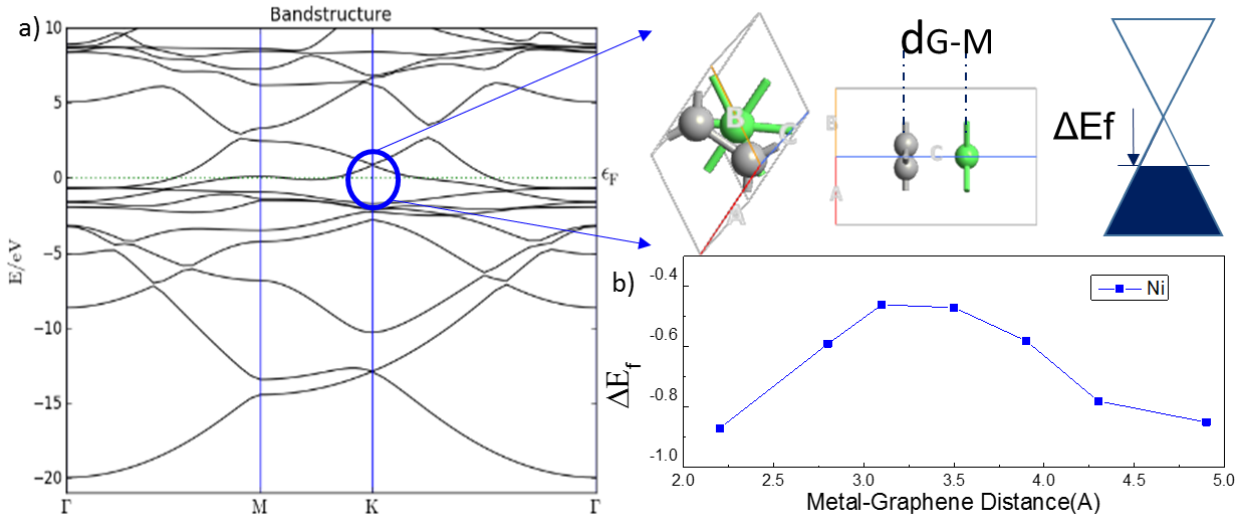

Figure 2.12 (a) Bandgap of the graphene-nickel junction. A unit cell of the nickel-graphene junction is built, in which the green atom is nickel and the grey atom is carbon. The distance between graphene-nickel $d_{G\text{-}M}$ was set as 3.5A for this calculation. Downwards shift of Fermi level indicates hybridization of graphene as shown in the zoom-in image. (b) Fermi level shift vs $d_{G\text{-}M}$.

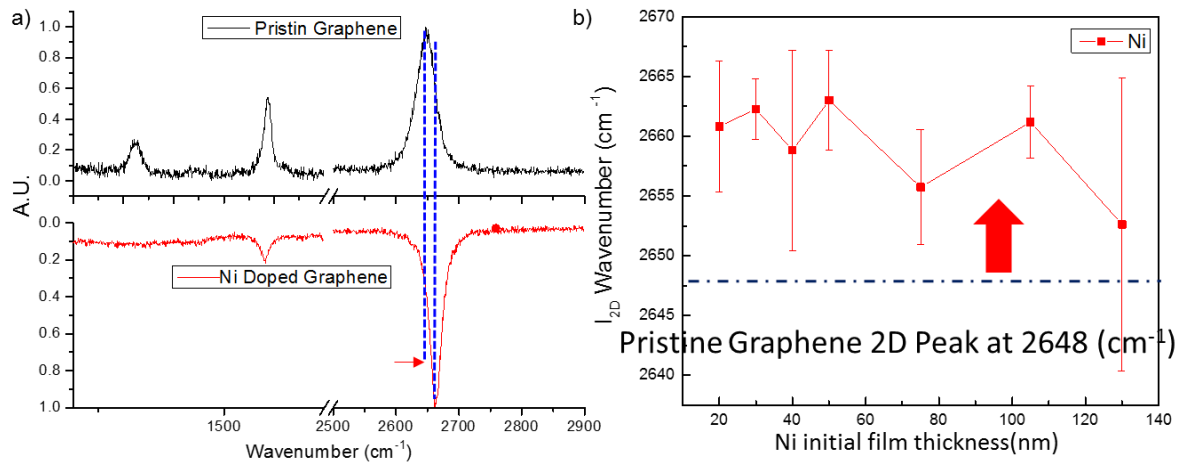

Figure 2.13 Raman spectra results showing a blue-shift of the 2D intensity peak of graphene flakes fabricated by the droplet CVD process implying hybridization from nickel.

2.4 Conclusion

We have demonstrated the synthesis single-layer graphene on nickel droplets using the CVD process. Reduced droplet size (≈1 μm) decreases the carbon absorption amounts and makes possible the as-grown graphene to be single layer. Graphene can outgrow over the boundaries of nickel droplets, forming continuous graphene layer over discontinuous nickel droplets (using 75 nm thick nickel film). Such graphene flakes can be directly used in the demonstrated photosensing device without the time-consuming transfer process by responding to visible light with generated photocurrent up to ≈0.53 μA mm^{-2} W^{-1}. We attribute this phenomenon to a photothermal effect, which is originating from graphene flakes. This has been verified by geometrically symmetric and asymmetric measurements in response to different temperature gradients. This work not only brings inspiration on self-limiting processes for the synthesis of 2D materials and the fabrication of devices bypassing the transfer process, but also investigates the photothermal effect induced by in situ hybridization instead of double gate tuning in former literatures[21].

2.5 Experimental Section

Synthesis of graphene: First, nickel thin films of 20, 30, 40, 50, 75, 105, and 130 nm, respectively, have been deposited onto a silicon substrate with an insulation layer of 300nm-thick thermal oxide on top, using thermal evaporation (NRC evaporator). During the CVD process, carrier and reduction gases of Ar:H2 (300:55 sccm) are first flowed into the furnace under a heating profile of 20 ºC/min, using a quartz tube furnace (Lindburg). When temperature is stabilized for the pyrolysis reaction at 1000 ºC, 5 sccm of CH4 is added as the carbon source for 10 minutes to synthesize graphene. Afterwards, the furnace is cooled down at a speed of 20 ºC/min with the protection gases of H2 and Ar flowing in the tube. Samples are removed when the furnace is cooled to room temperature.

Transfer of graphene onto the TEM foil: PMMA (495 A2) is spin coated on graphene sheets grown by the nickel droplet process at a speed of 3000 rpm; cured at 150 oC for 1 min; and then put in 1:10 HF:H2O to etch away silicon oxide. The floating PMMA/graphene film is flipped with graphene side on top. The copper grid is placed onto the sample with nickel particle and graphene

area under microscope, and one drop of IPA is dipped on the sample to attach TEM grid onto the PMMA sample. After the sample is baked at 80 oC for 1 min to dry the TEM grid onto graphene, PMMA is removed by acetone.

Characterization of graphene: Scanning electron microscopy and Energy-dispersive X-ray spectroscopy (EDS) images under FEI QuantaTM. The Raman Spectroscopy (Renishaw inVia Raman microscope) mapping results are done with 633 nm laser. Mapping on a 4μm×4μm sample area, scanning 200cm-1 wavenumber near 1500cm-1 and 2700cm-1, which include the D, G, and 2D peak. Resolution of the Raman spectroscopy spot is 0.3μm while the motion stage moves at a 0.2 μm step. Atomic Force Microscopy is done on 5μm×5μm sample area using the Asylum research AFM.

Characterization of photocurrent: Photocurrent is recorded with Agilent 34401A with DMM software to output digital data. Tests have been performed in a probe station (Wentworth Laboratories), and the illumination of visible light is executed by ECO-Light 150 with a reduced power at 15W. Limit of the lens focus spot is ~1mm diameter, and the light is shined on different sample area to study the symmetry of the photocurrent generation. Two probes as the electrodes and sample holder stage are moving synchronically with the same step insuring the two probes are at the edge of the sample. Frequency of the light source is changed mechanically.

Reference

1. A. K. Geim and K. S. Novoselov, *Nature Materials*, 2007, **6**, 183-191.
2. X. Zang, Q. Zhou, J. Chang, Y. Liu and L. Lin, *Microelectron Eng*, 2015, **132**, 192-206.
3. K. S. Novoselov, A. K. Geim, S. V. Morozov, D. Jiang, M. I. Katsnelson, I. V. Grigorieva, S. V. Dubonos and A. A. Firsov, *Nature*, 2005, **438**, 197-200.
4. M. H. Oliveira, J. M. J. Lopes, T. Schumann, L. A. Galves, M. Ramsteiner, K. Berlin, A. Trampert and H. Riechert, *Nat Commun*, 2015, **6**.
5. J. H. Lee, E. K. Lee, W. J. Joo, Y. Jang, B. S. Kim, J. Y. Lim, S. H. Choi, S. J. Ahn, J. R. Ahn, M. H. Park, C. W. Yang, B. L. Choi, S. W. Hwang and D. Whang, *Science*, 2014, **344**, 286-289.
6. L. Baraton, Z. B. He, C. S. Lee, C. S. Cojocaru, M. Chtelet, J. L. Maurice, Y. H. Lee and D. Pribat, *EPL*, 2011, **96**.
7. R. M. Jacobberger, B. Kiraly, M. Fortin-Deschenes, P. L. Levesque, K. M. McElhinny, G. J. Brady, R. Rojas Delgado, S. Singha Roy, A. Mannix, M. G. Lagally, P. G. Evans, P. Desjardins, R. Martel, M. C. Hersam, N. P. Guisinger and M. S. Arnold, *Nat Commun*, 2015, **6**.
8. P. W. Sutter, J. I. Flege and E. A. Sutter, *Nature Materials*, 2008, **7**, 406-411.
9. J. Cai, C. A. Pignedoli, L. Talirz, P. Ruffieux, H. Söde, L. Liang, V. Meunier, R. Berger, R. Li, X. Feng, K. Müllen and R. Fasel, *Nat Nanotechnol*, 2014, **9**, 896-900.
10. D. Geng, H. Wang and G. Yu, *Advanced Materials*, 2015, **27**, 2821-2837.
11. Z. Yan, Z. Peng and J. M. Tour, *Accounts of Chemical Research*, 2014, **47**, 1327-1337.
12. G. Ding, Y. Zhu, S. Wang, Q. Gong, L. Sun, T. Wu, X. Xie and M. Jiang, *Carbon*, 2013, **53**, 321-326.
13. D. Geng, B. Wu, Y. Guo, L. Huang, Y. Xue, J. Chen, G. Yu, L. Jiang, W. Hu and Y. Liu, *Proceedings of the National Academy of Sciences of the United States of America*, 2012, **109**, 7992-7996.

14. A. R. Harutyunyan, *Proc. Natl. Acad. Sci. USA*, 2012, **109**.
15. K. K. Nanda, *Pramana - Journal of Physics*, 2009, **72**, 617-628.
16. A. Ismach, C. Druzgalski, S. Penwell, A. Schwartzberg, M. Zheng, A. Javey, J. Bokor and Y. Zhang, *Nano Lett*, 2010, **10**, 1542-1548.
17. T. M. Paronyan, E. M. Pigos, G. Chen and A. R. Harutyunyan, *Acs Nano*, 2011, **5**, 9619-9627.
18. H. Kim, C. Mattevi, M. R. Calvo, J. C. Oberg, L. Artiglia, S. Agnoli, C. F. Hirjibehedin, M. Chhowalla and E. Saiz, *Acs Nano*, 2012, **6**, 3614-3623.
19. P. Y. Huang, C. S. Ruiz-Vargas, A. M. Van Der Zande, W. S. Whitney, M. P. Levendorf, J. W. Kevek, S. Garg, J. S. Alden, C. J. Hustedt, Y. Zhu, J. Park, P. L. McEuen and D. A. Muller, *Nature*, 2011, **469**, 389-392.
20. L. M. Malard, M. A. Pimenta, G. Dresselhaus and M. S. Dresselhaus, *Physics Reports*, 2009, **473**, 51-87.
21. A. C. Ferrari, J. C. Meyer, V. Scardaci, C. Casiraghi, M. Lazzeri, F. Mauri, S. Piscanec, D. Jiang, K. S. Novoselov, S. Roth and A. K. Geim, *Phys Rev Lett*, 2006, **97**.
22. C. Mattevi, H. Kim and M. Chhowalla, *Journal of Materials Chemistry*, 2011, **21**, 3324-3334.
23. D. Wang, H. Tian, Y. Yang, D. Xie, T. L. Ren and Y. Zhang, *Scientific Reports*, 2013, **3**.
24. E. J. H. Lee, K. Balasubramanian, R. T. Weitz, M. Burghard and K. Kern, *Nat Nanotechnol*, 2008, **3**, 486-490.
25. P. Wei, W. Bao, Y. Pu, C. N. Lau and J. Shi, *Phys Rev Lett*, 2009, **102**.
26. M. Brandbyge, J. L. Mozos, P. Ordejón, J. Taylor and K. Stokbro, *Physical Review B - Condensed Matter and Materials Physics*, 2002, **65**, 1654011-16540117.
27. N. M. Gabor, J. C. W. Song, Q. Ma, N. L. Nair, T. Taychatanapat, K. Watanabe, T. Taniguchi, L. S. Levitov and P. Jarillo-Herrero, *Science*, 2011, **334**, 648-652.
28. P. Dollfus, V. H. Nguyen and J. Saint-Martin, *Journal of Physics Condensed Matter*, 2015, **27**.

3 Chapter: TiS_2 Coated Carbon Nanotube Hybrid Electrodes Enable High Energy Density Pseudocapacitors

Keyword: transition metal dichalcogenide; titanium disulfide; supercapacitor; energy density

3.1 Abstract

Electrochemical supercapacitors often have high power density and long operation lifetime but limited energy density while pseudo-capacitive materials based on the fast surface redox reactions are widely studied to enhance their energy storages. Several reported systems exhibit high capacitance but restricted operating voltage windows usually no more than 1V in aqueous electrolytes. Here, we demonstrate that vertically aligned carbon nanotubes (VACNT) with uniformly coated titanium disulfide(TiS_2) composite electrodes can extend the working range over 3V for stable capacitive behaviors to achieve a high capacitance of 195 F/g in a Li-rich electrolyte. A symmetric cell has an energy density of 60.9 Wh/kg - the highest among pseudocapacitors using metal oxides, conducting polymers, 2D transition metal carbides (MXENE) and other transition metal dichalcogenides. Nanostructures prepared by an atomic layer deposition (ALD)/sulfurization process facilitate ion transports and surface reactions to result in a high-power density of 1250 W/kg and a stable operation over 10,000 cycles. A flexible solid-state supercapacitor prepared by transferring the TiS_2-VACNT composite film onto Kapton tape is demonstrated to power a 2.2 V LED for 1 minute.

3.2 Introduction

Transition metal dichalcogenide (TMDC) materials such as MoS_2, WS_2, and $MoSe_2$, have been widely studied in electrochemical applications as sensors[1], catalysts[2], and energy storage materials[1, 3]. Among all TMDCs, TiS_2 is the lightest and cheapest[4] with the following potential benefits for lithium-based energy storage systems: (1) highest energy density storage capability among TMDCs[4], (2) fast ion transportation rate[5], (3) low volume expansion during reversible charge-discharge cycles[6], and (4) no phase change during lithium ion intercalation[4]. However, TiS_2 suffers from mechanical degradation during the ionization and deionization and has less desirable electrical conductivity[7]. Coating TiS_2 onto 3D highly conductive network such as vertical aligned carbon nanotube (VACNT) will promote the intrinsic conductivity, further increase the surface area and increase the mechanical stability which are essential for the electrode design in electrochemical reactions[8]. Potential methods include chemical vapor deposition (CVD)[9], electro- and electro-less plating[10], and atomic layer deposition (ALD)[11]. The CVD and plating-based processes encounter challenges in uniform coverage and crystallinity while the ALD deposition can achieve uniform and conformal coverage on porous, high aspect-ratio structures such as VACNT forests [12]. While the conventional ALD of TiS_2 uses $TiCl_4$ and highly toxic H_2S as precursors with the production of sulfur that contaminates ALD chambers[11], here we developed a two-step process that combines ALD of TiN [13] with a following CVD sulfurization to fabricate TiS_2 composite-coated VACNT electrodes with desired nanostructures. Further characterizations

demonstrate that the pseudocapacitive electrodes show a capacitance of 195 F/g within a potential range of 3 V in a lithium-rich aqueous electrolyte, corresponding to an energy density of 60.9 Wh/kg for a symmetric cell, which is exceptional among reported pseudocapacitors.

The structure of the TiS_2 coated VACNT hybrid electrodes is illustrated in **Figure 3.1a**, in which a TiN layer is deposited by ALD and sulfurized to be TiS_2 composite via annealing in sulfur powder at relatively low temperature (300 ºC) and maintain conformal coating on VACNTs. Such electrodes show high electrochemical capacitance due to the intercalation of Li-ion with TiS_2 composite. Furthermore, the electrode material successfully operates within a large potential window of 3V in a lithium rich "water-in-salt" electrolyte[14, 15]. As such, the energy density of the supercapacitor cell, proportional to the capacitance multiplies voltage square, outperforms most state-of-art pseudocapacitors using metal oxides, metal chalcogenides, and metal carbide[16-23] with comparable results to Li-ion batteries (**Figure 3.1b**). TiS_2-VACNT composite in ultra-high concentration LiTFSI electrolyte represents a specific energy 900 times that of a bare VACNT using a 0.5 M H_2SO_4 electrolyte, and shows advantage over other electrodes of similar structures made of VACNT forests coated with pseudocapacitive materials, such as RuO_x[12], TiN[13], and MoS_2[17] in capacitance, energy density, and power density. Moreover, TiS_2 composite coated on CNT inherit the low phase transformation rate in lithiation and de-lithiation cycles[4], and maintain low deformation ratio (<5%) and high capacitance retention (~95%) after 10,000 cycles of cyclic voltammetry test (**Figure 3.1c**).

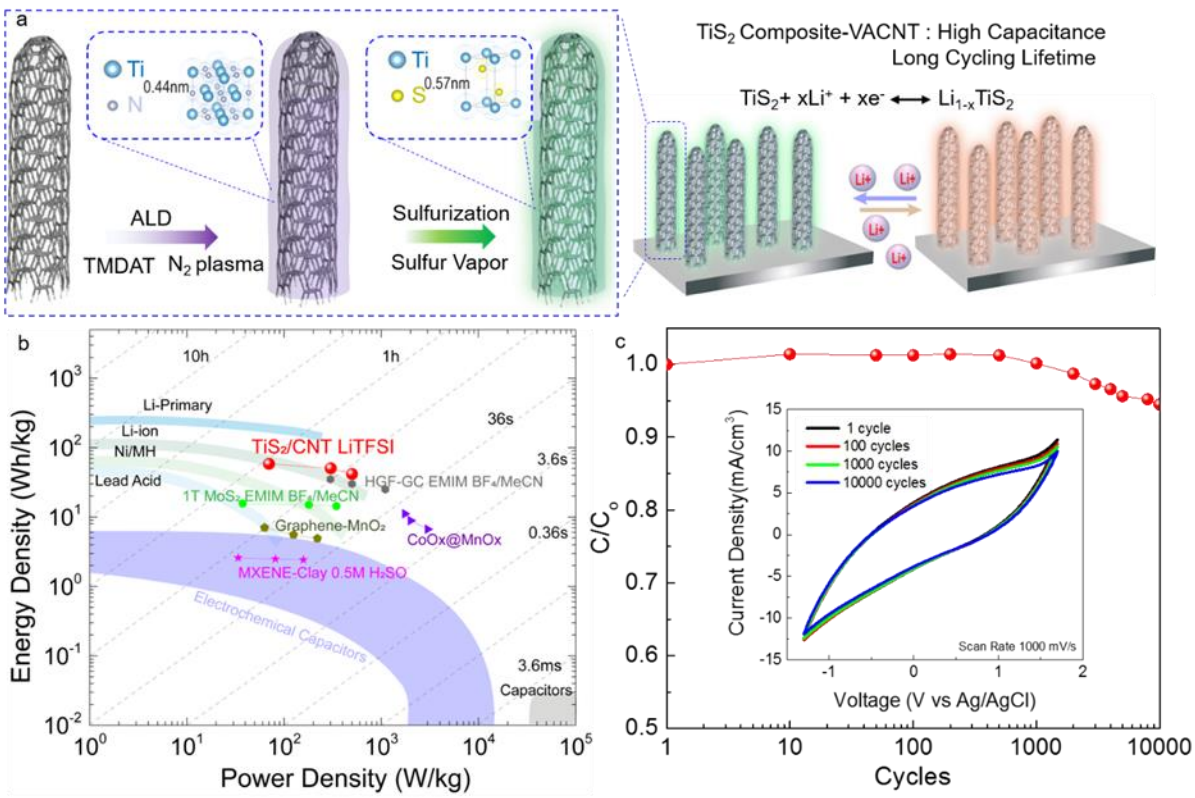

Figure 3.1 TiS_2-VACNT hybrid fabrication process and advantage as Pseudocapacitor electrodes. (a) TiS_2-VACNT composite electrodes synthesized by a two-step process: TiN is coated onto VACNT by atomic layer deposition and converted to TiS_2 composite in a sulfur vapor environment. The high capacitance energy storage in Li+ electrolyte is achieved by electron-

double-layer and TiS_2 Composite-Li intercalation. (b) Ragone plot for the state-of-art energy storage systems showing TiS_2-VACNT composite with the highest energy density among various families of non-carbon materials, including metal oxides, metal chalcogenides, and metal carbide-based system [16-23]. (c) Long term cyclability of the TiS_2-VACNT composite electrode in the 21 m LiTFSI electrolyte.

3.3 Results and Discussion

The conductive, porous VACNT forest is grown on a silicon or stainless steel substrate[8] and the diameter of an as-grown CNT is 13±5 nm (**Figure 3.2**). Afterwards, 500 cycles of ALD TiN are deposited for a uniform and conformal coating of TiN with a final TiN/CNT diameter of 130±15 nm (**Figure 3.3**). Deposition rate varies from 0.06 nm/cycle to 0.25 nm/cycles depending on temperature and cycle numbers; the average growth rate for 500 cycles is ~0.11 nm/cycle and ~0.12 nm/cycle for 800 cycles (**Figure 3.3**).[24, 25] Under sulfur vapor annealing at 300 ºC for 30 minutes, the amorphous TiN layer is converted to polycrystalline TiS_2 composite (**Figure 3.4a**) and maintains conformal coating on CNTs (**Figure 3.4b**). High resolution transmission electron microscopy (HRTEM) (**Figure 3.4c**) reveals that the resulting materials are hexagonal-shaped structures with characteristic polycrystalline diffraction rings, in-plane 0.3 nm lattice distance, and (001) zone axis of the CdI_2 type (P 3 - M 1) symmetry. X-ray Diffraction (XRD) shows standard peaks of TiS_2 composite with the low angle at 16.6º due to the (001) stacking structures, and the (110) and (101) peaks by using a Co X-ray diffraction source (**Figure 3.4**). Split Ti_2p peaks indicate composite Ti^{4+} and Ti^{3+} (residual TiN) with different spin-orbital splitting showing different energy difference (**Figure 3.4e**). **Figure 3.2f** reveals S_2p$^{1/2}$ and S_2p$^{3/2}$ spin splitting with energy different of 1.39 eV. Sulfur peaks of S_2s at the binding energy of 228.8 eV and S_2p at the binding energy of 164.8 eV are observed after 1 and 3 times of repeated sulfur annealing while the relative distance and intensity of the peaks are almost the same (**Figure 3.5**), implying that additional sulfurization does not contribute to further material conversions from TiN to TiS_2 composite.

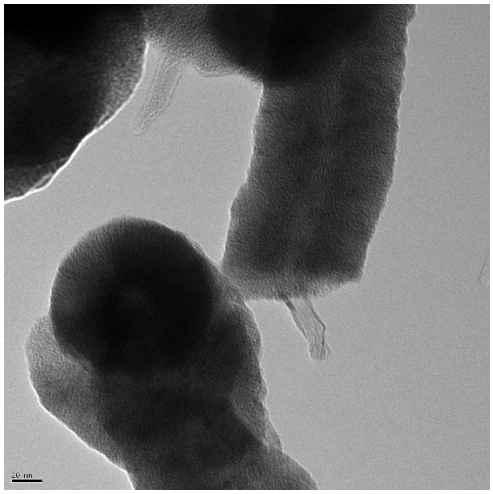

Figure 3.2 Transmission electron microscope (TEM) image of TiN coated CNT, scale bar 20 nm.

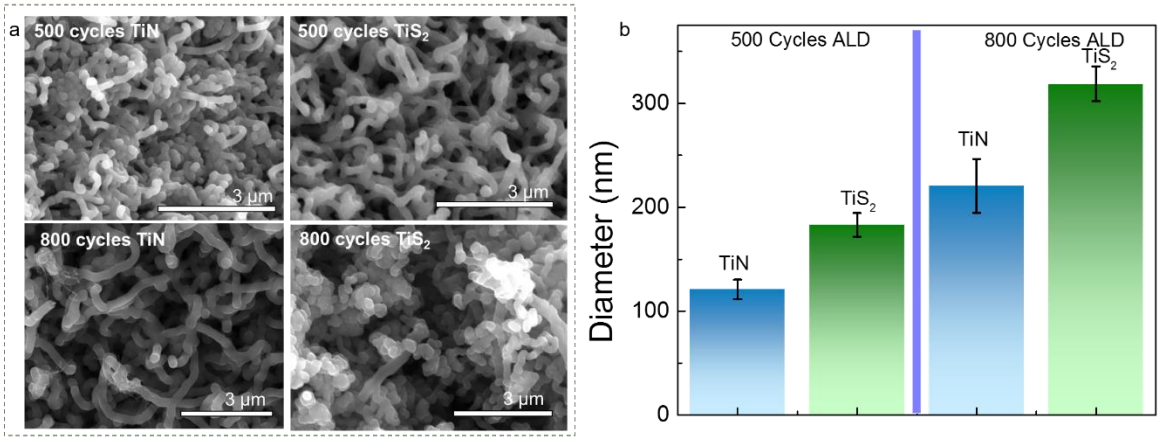

Figure 3.3 (**Left**)Top view SEM images of TiN-VACNT electrodes after 500 and 800 ALD cycles of TiN coatings and after the sulfur annealing process to convert TiN to TiS_2 composite. (**Right**) Diameters of the fabricated TiN-VANCT and TiS_2-VACNT hybrid electrodes.

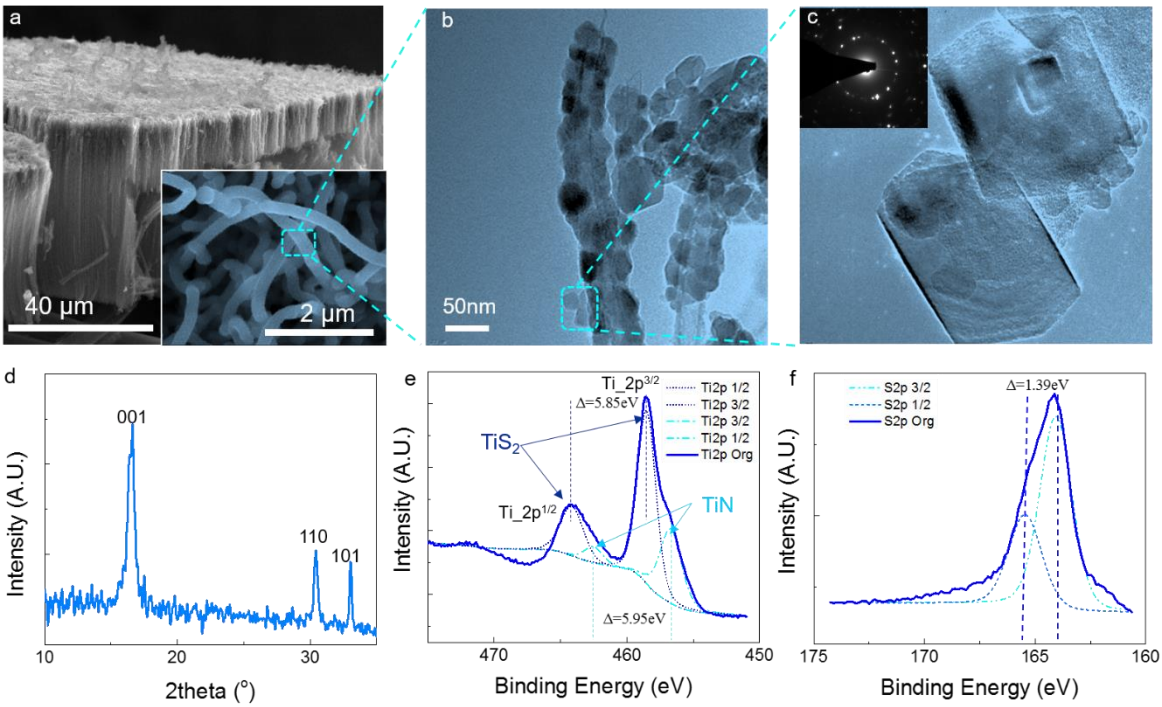

Figure 3.4 **Material characterization of the TiS_2-VACNT composite electrodes**. (a) SEM image after a 500-cycle ALD TiN deposition process followed up with a sulfurization step; (Inset) magnified SEM image showing individual electrodes with diameter of 210±13nm. (b) TEM image of CNT coated with sulfurized TiS_2 composite particles. (c) Zoomed in TEM image of hexagonal TiS_2 composite nanoparticles in (b). (d) XRD showing the (001) peak at 16.6°, (110) at 30.4° and (101) at 33.1°. Enlarged lattice parameters of TiS_2 composite than TiS_2 could be attributed to the lattice deformation induced by nitrogen atoms. (e) X-ray photoelectron spectroscopy (XPS) spectrum for TiS_2 composite-VACNT, in which split Ti_2p$^{1/2}$ and Ti_2p$^{3/2}$ peaks indicate different

composition of TiS_2 and TiN. (f) XPS spectrum of sulfur peak of TiS_2 composite, with S_2p$^{1/2}$ and S_2p$^{3/2}$ split peaks.

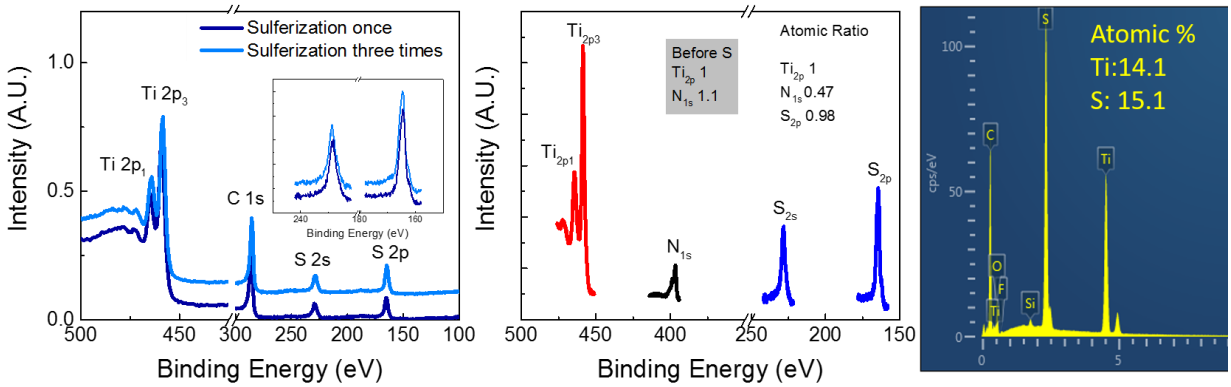

Figure 3.5 X-ray photoelectron spectroscopy (XPS) and Electron dispersion spectrum(EDS) of the TiS_2-VACNT composite electrodes.

50–60 nm-thick TiN film from the 500-cycle ALD process is effectively converted to TiS_xN_y after one sulfur vapor annealing process at 300ºC for 30 minutes, which results in roughly ~53% diameter increment (**Figure 3.3**). Atomic ratios of N to Ti in X-ray photoelectron spectroscopy changes from 1.1 to 0.47, implying a ~60% conversion rate from TiN to TiS_2. S to Ti ratio is 0.98–1.07 from EDS (electron dispersion spectrum) (**Figure 3.4**) and XPS results, implying 50% out of the 60% converted product is TiS_2 composite**.** The impurities, which are limited in quantity, are neither effectively reflected in XRD nor electrochemical tests (**Figs. 3.2, 3.3 & 3.4**). Integrated peak area of TiS_2_2p$^{3/2+}$ to TiN_2p$^{3/2}$ is 1.1:1, indicating a rough estimation of $(TiS_2)_{1.1}$(TiN) composition which could be normalized as $TiS_{1.05}N_{0.48}$. Such result is coherent with electron dispersion spectrum (EDS), and the conversion is estimated to be 55±5% (**Figure 3.5**). Density of TiS_2, ρ_{TiS_2} , is 3.22 g/cm^3, while the density of TiN, ρ_{TiN} , is 5.40 g/cm^3. The dimeter of the partially converted TiS_2-VACNTs composite expands due to the decrease of density. The diameter change is shown in **Figure 3.3**. The diameter of 500-cycle TiN-VACNT structures is 130nm±12nm and the diameter of the TiS_2-VACNT composite structures is 186±10 nm (~1.43×). Similarly, the diameter of 800-cycles TiN-VACNT structures is 220nm±20 nm and the diameter of the TiS_2-VACNT composite structure is 318±15nm (~1.44×).

In **Figure 3.6a**, cyclic voltammetry (CV) results show that TiS_2 composite-VACNT in 21 m LiTFSI electrolyte exhibits over ~100 times the specific capacitance (per projected surface area) of as-grown VACNT electrode in 0.5M H_2SO_4 electrolyte. Two key mechanisms are believed to assist this significant increase: (1) intercalation of Li-S into and out of the TiS_2 composite and (2) increasing the working voltage window from 1 V to 3 V. It is found that the specific capacitance increases ~4 times from the VACNT-H_2SO_4 system to the VACNT-LiTFSI system, and 26.8 times from the VACNT-LiTFSI system to the TiS_2 composite-VACNT-LiTFSI system; the total increase is more than 100 times higher capacitance. Furthermore, the length of VACNT is found to slightly affect the performances of the TiS_2 composite-VACNT electrode systems (**Figure 3.6c** and **Figure 3.7**). The system made of 4 µm-thick VACNT grown on stainless steel has about 15%

higher specific capacitance (195 F/g) as compared with that of the system made of 40 µm-thick VACNT grown on silicon (168 F/g). Systems made of shorter VACNT electrodes could benefit from increased sulfur diffusion in the annealing process for the conversion of TiS_2 composite and smoother ion diffusion process during the charge/discharge process. In the fitted capacity vs reverse of scan rate square root in Figure 6c, the larger constant of $v^{1/2}$ than the interception constant indicate is near 2:1 portion of diffusive to capacitive behavior in the cyclic voltammetry curve which is reasonable with the nature of Li^+-Ti-S intercalation.

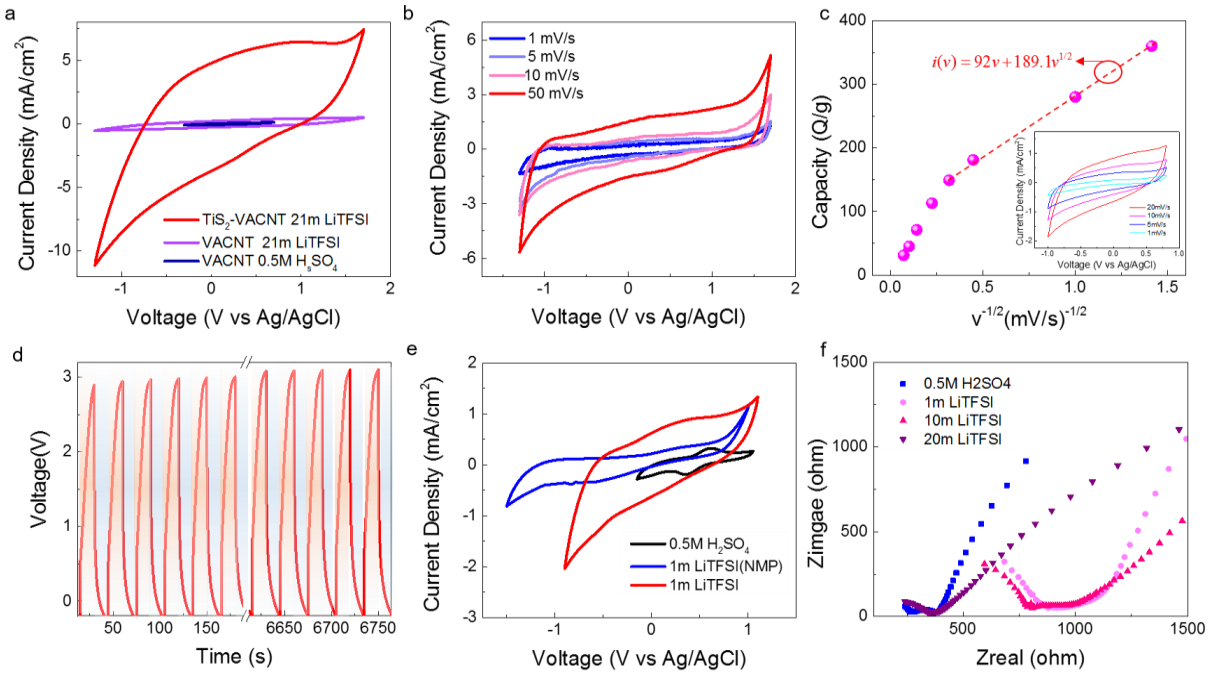

Figure 3.6 Electrochemical testing results of TiS_2-VACNT composite electrodes in the 21 m LiTFSI electrolyte. (a) cyclic voltammetry (CV) results from three systems: as-grown VACNT electrodes in 0.5 M H_2SO_4 electrolyte, in 21 m LiTFSI electrolyte, and TiS_2-VACNT composite electrodes in 21 m LiTFSI electrolyte. (b) CV results of TiS_2-VACNT composite electrode in 21 m LiTFSI electrolyte under different scanning rates from 1 to 50 mV/s. (c) Analysis on the energy storage capacity vs $v^{-1/2}$. (d) Repeating chronopotentiometry charge-discharge tests of TiS_2 omposite/CNT in 21 m LiTFSI with discharging current density of 300µA/cm^2. (e) and (f) CV and Nyquist plots of TiS_2-VACNT composite electrodes in multiple electrolytes.

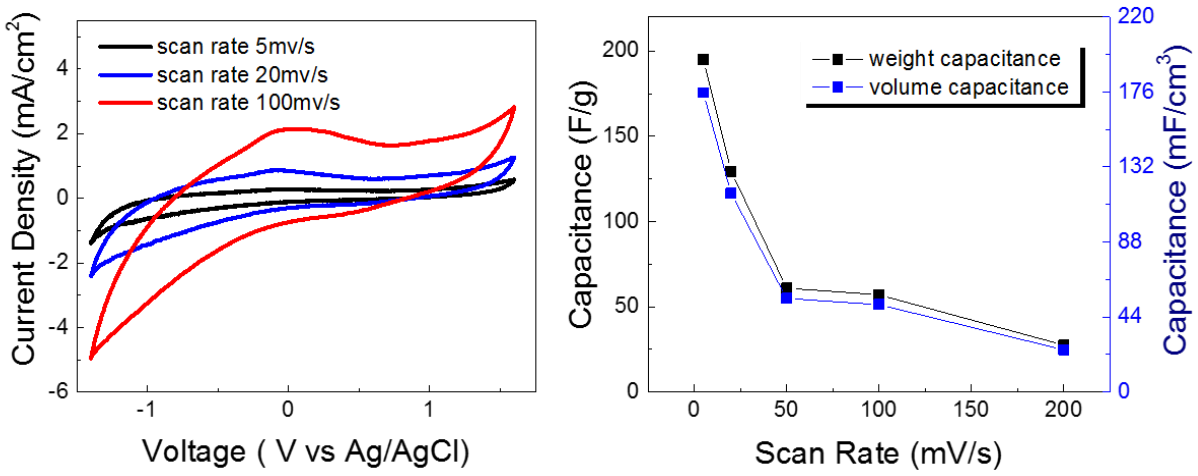

Figure 3.7 Testing results of TiS_2-VACNT composite electrodes grown on the stainless-steel substrate using a 10 nm-thick Al_2O_3 passivation layer. In our previous research, Fe/Al/Mo/SiO_2 substrates are used for VACNT growth which generally yields >10μm VACNT. To shorten the CNT forest, stainless steel pieces employed as both supporting layer and catalyst layer with a passivation layer of 10 nm Al_2O_3. Compared to former multi-evaporation processes, single-step passivated stainless steel is capable of higher throughput onto flexible substrates which can be directly packaged into electrochemical cells.

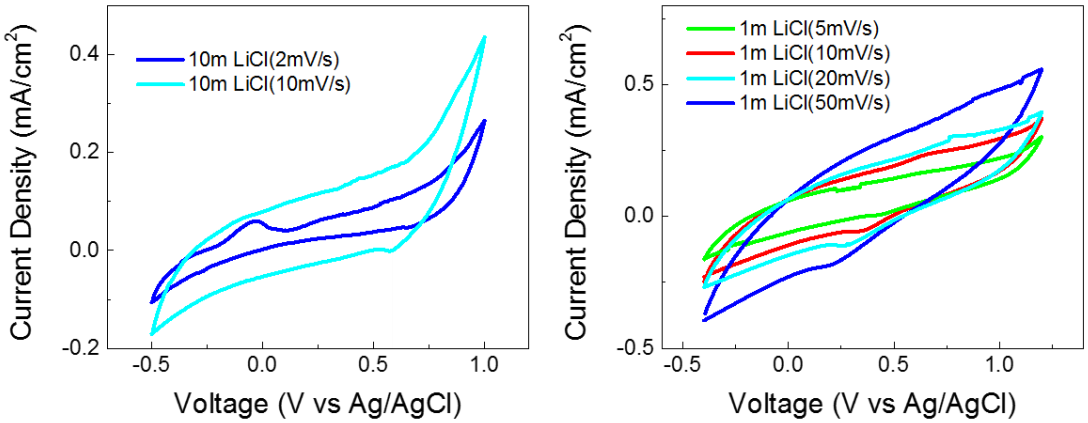

Figure 3.8 (a) Cyclic Voltammetry tests of the TiS_2-VACNT composite electrode systems in the 10m LiCl electrolyte with different scan rates. (b) Cyclic Voltammetry tests of TiS_2-VACNT electrode systems in the 1m LiCl electrolyte with different scan rates.

The absence of lithiation-delithiation peak on the CV curve (**Figure 3.6b**) could be attributed to the higher surface area introduced by VACNT and the complex composition introduce many other phase that could shift the intercalation peak positions. Similarly, if the 10m LiCl electrolyte is used as the electrolyte (**Figure 3.8**), no lithiation peaks are observed at 10 mV/s with only a small

peak at 2 mV/s. It is estimated that the density of the TiS_2-VACNT composite electrodes is 0.9 g/cm^3 such that the chronopotentiometry current density of 1 mA/cm^2 is equivalent to 1.11 A/g (**Figure 3.9**). When a 1.5 mA/cm^2 current density source is used, it takes about 15 seconds to charge/discharge the system to 3 V (**Figure 3.6d**). It is found that the TiS_2-VACNT composite network helps to mechanically stabilize the system during the cycling tests: > 95% of original capacitance is maintained after 10,000 operation cycles. There is also no obvious change in the morphology of the electrodes (**Figure 3.10**). Furthermore, the system made of an 800-cycle ALD TiN does not show obvious improvement of specific capacitance as compared with the system made of 500-cycle ALD TiN and longer sulfurization annealing does not significantly improve performance (**Figure 3.11**).

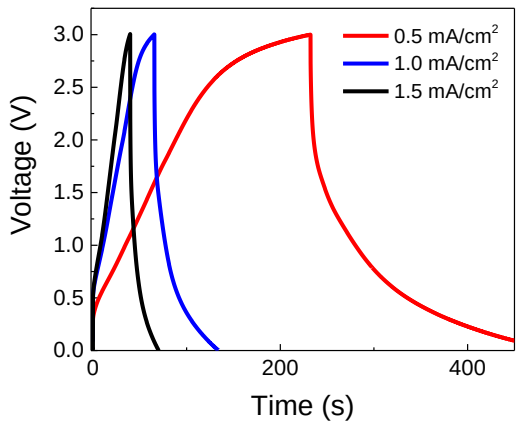

Figure 3.9 Chronopotentiometry charge-discharge curve of a TiS_2-VACNT electrode system in 21m LiTFSI electrolyte at varying current densities.

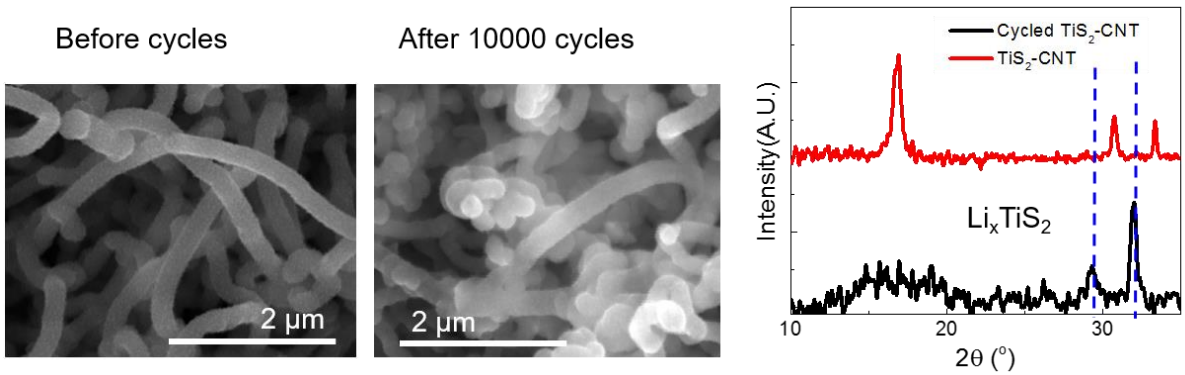

Figure 3.10 (Left) SEM images of the TiS2-VACNT hybrid electrodes before and after the 10,000-cycle CV test showing increasing diameter (~ 10% 186±13nm to 200±15nm) without significant morphology change. (Right) XRD illustrating partial lithiation of TiS_2 after 10,000 CV cycles. The (001) peak is broadened and shifted, while the (110) and (101) peaks shifted from 30.4o to 29.4o and 33.1o to 31.9o respectively, indicating lattice deformation of 3.1% and 4.5%.

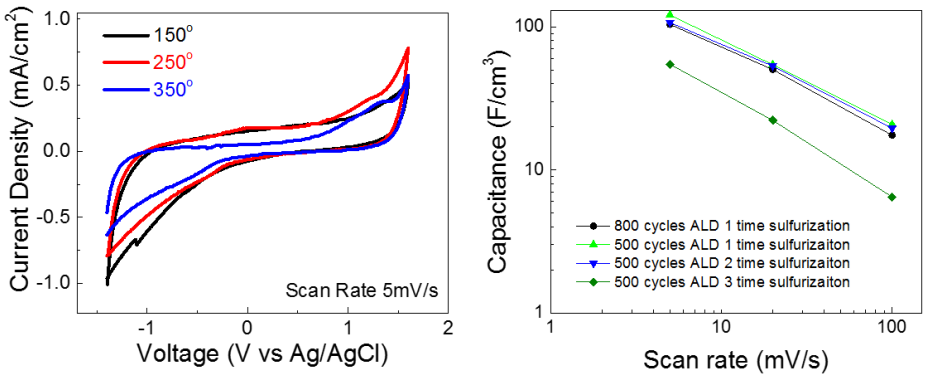

Figure 3.11 (Left) CV tests of the TiS_2-VACNT composite electrode systems under different temperature, showing similarity in capacitance after the integration of the current density curve. Results show that the single sulfurization and double sulfurization provide similar specific capacitance. However, the triple sulfurization processes decrease the specific capacitance, which could be induced by the increased oxidation in thermal annealing. (**Right**) The measured specific capacitance of the TiS_2-VACNT electrode systems with different processing parameters. It is found that the 1, 2, or 3 times of sulfur vapor annealing process results produce little differences on the electrochemical testing results.

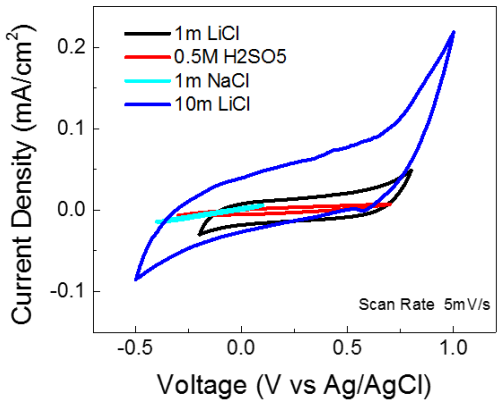

Figure 3.12 cyclic voltammetry test results of TiS_2-VACNT electrode systems in different electrolytes.

Effects of different electrolytes, 0.5M H_2SO_4, 1 m LiTFSI in NMP(N-Methyl-2-pyrrolidone), and 1 m LiTFSI (**Figure 3.3e**), were observed under different operation voltage windows and organic NMP based electrolyte provide slightly higher working window. However, the TiS_2-VACNT composite electrode system in 1 m LiTFSI electrolyte (dissolved in NMP) can produce only about one-third of capacitance density than that of the same electrode system in the 1 m LiTFSI electrolyte dissolved in DI water (Table 1) due to the lower ionic activity in organic solvent[26]. Other key results from the Li^+-rich electrolytes are summarized in Table 1. Working voltage window was found to scale with Li^+ concentration as the activity of water molecule is suppressed by the high concentration of cathodic Li^+ and anodic $TFSI^-$ or Cl- (additional results in **Figure 3.12**). As a result, the hydrogen evolution reaction (HER) and oxygen evolution reaction (OER) depopulate to broaden the stable operation voltage window[15]. Specifically, high

concentrations of LiTFSI extend the electrochemical window from 1.9V (1 m) to 3V (21 m), and high concentrations of LiCl extend the window from 1.4V (1 m) to 2.35 V (20 m). Furthermore, the large TFSI anion forms higher Helmholtz layer potentials to increase the threshold of oxygen evolution swing to 1.7 V (Cl^- solution occurs at 1.05 V). On the other hand, electrolytes based on H_2SO_4 and NaCl (H^+ or Na^+ ions) do not exhibit intercalation with TiS_2 composite. In fact, H^+ increases the probability of hydrogen evolution by lowering overpotential in the hydrogen evolution reaction (HER), decreasing the electrochemical voltage window. Furthermore, high LiTFSI concentration increases the conductivity of ions and lowers electrolytic impedence[27] (**Figure 3.3f**). These characteristics in high-concentration LiTFSI solution work to improve both energy density and power density of Li-ion-based storage systems.

The electrochemical voltage window is further determined by the coated active material (VACNT works as an inert electrode). Experimentally, stable ranges of -1.3 V to 1.7 V vs Ag/AgCl (1.9 V to 4.9 V vs Li/Li+) for the TiS_2-VACNT composite electrodes under the 21 m LiTFSI electrolyte are observed (**Figure 3.13a**), higher than the other three tested pseudocapacitive materials, RuO_x, MoS_2, and TiN. Both RuO_x-VACNT and MoS_2-VACNT electrode systems act as HER/OER catalysts and decrease the stable operation voltage window[28, 29]. The TiN-VACNT electrode system shows an undesirable broad electrochemical peak near -0.4 V which could be attributed to either hydrolysis or TiN-TiO_2 impurity transition reactions due to the instability of TiN in acidic media[30]. As such, the TiS_2-VACNT composite electrode system provides unique characteristics in the 21 m LiTFSI: (1) a large stable electrochemical operation voltage window, (2) high capacitance density, (3) high power density, and (4) high energy density as compared with the other electrode systems. Specifically, experimental results show the TiS_2-VACNT composite system can result in the largest enclosed area in the CV tests than those of tested RuO_x-, MoS_2-, and TiN-VACNT systems with a scanning rate of 100 mV/s (**Figure 3.13b**), and has the highest capacitance density under various scan rates (**Figure 3.13c**). Although RuO_x is considered one of the highest capacitance materials[31], it is incapable of effective Li^+ intercalation in Li-rich electrolytes. MoS_2 has a higher density (5.06 g/cm^3) than that of TiS_2 composite (supplementary materials) which leads to unfavorable gravimetric capacitance and energy density. In this work, MoS_2-VACNT electrodes are also shown to suffer from poor coverage onto the individual CNT electrodes as most of the deposition forms a layer on the top of the VACNT structure (**Figure 3.14**). TiN shows good electrical conductivity but its electrochemical performance is not comparable with TiS_2 composite in Li^+ or non-Li^+ electrolytes. **Figure 3.13d** summarizes the nominal energy density and working potential window for the tested electrodes presented in this paper. **Figure 3.13e** shows the measured energy density and power density of all tested electrodes under different scan rates to show high energy density and high power density of the different electrodes. **Figure 3.13f** records the relationships between capacitance density, energy density, and power density for all tested electrodes.

As a practical demonstration, a full symmetric cell device is constructed using a two-electrode design on filter paper (Fisher Scientific, P5 grade) under a broad range of scan rates from 2 to 100 mV/s (**Figure 3.15a**). The Nyquist plot shows the internal resistance to be about 1000 Ω, consistent with single cell impedance testing result of 400 Ω (**Figure 3.15b**). By transferring two TiS_2-VACNT composite film structures onto Kapton tape with filter paper as the separator, a flexible, fully operational cell is built. The semi-solid 21 m LiTFSI/5% PVA electrolyte is applied to measure a capacitance of 60 mF/cm^2 at a scan rate of 15 mV/s. This device is able to power a 2.2 V LED for 1 min (**Figure 3.15c**).

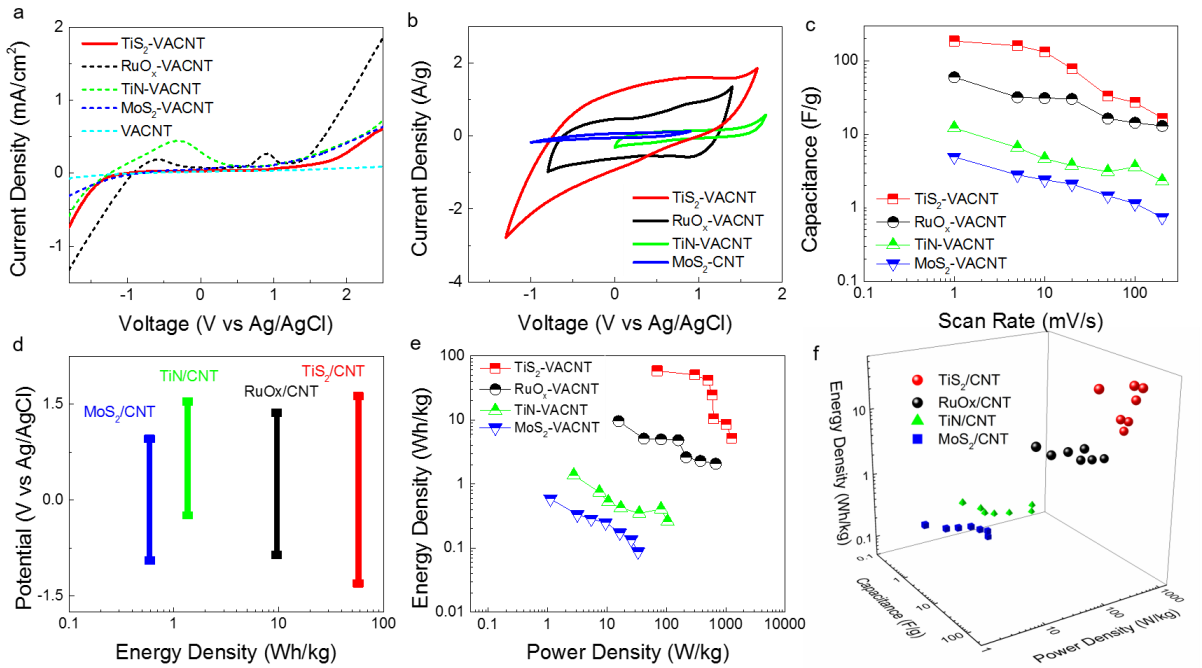

Figure 3.13 TiS_2-VACNT composite electrodes outperform other VACNT-based electrodes coated with high-energy pseduocapacitive materials such as RuO_x, TiN, and MoS_2. (a) Linear sweep voltammetry (LSV) results of as-grown VACNT, TiS_2 composite-, RuO_x-, TiN-, and MoS_2-VACNT electrodes in 21 m LiTFSI electrolyte under a scan rate of 5 mV/s. Both TiS_2 composite-VACNT and pristine VACNT electrodes exhibit a 3V stable operation window, while other electrodes have either broad redox peaks or hydrolysis reactions at a low voltage to reduce the electrochemical operation window (b) Measurement results of the energy density, power density, and capacitance density of the four VACNT electrodes coated with different materials. (c) CV results of four different electrodes in 21 m LiTFSI electrolyte under a scan rate of 100 mV/s. (d) Capacitance density vs. scan rate of the four electrode systems. (e) Operation voltage window vs. energy density for the four electrode systems. (f) Measured energy density vs. power energy density of the four electrode systems.

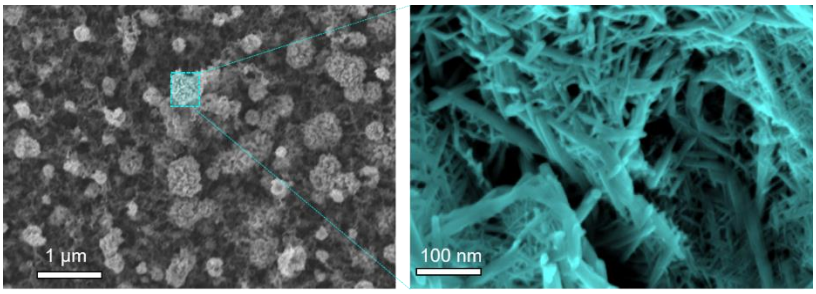

Figure 3.14 (**Left**) SEM image MoS_2 flower grown on top of VACNT forest. (**Right**) Zoomed in image illustrating the nanowire structure of (**Left**).

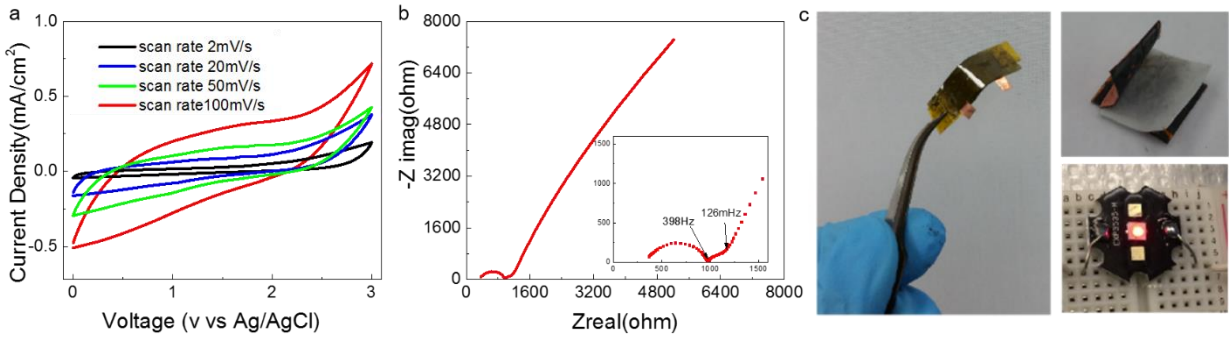

Figure 3.15 Demonstration of potential application: (a) CV of a symmetric full cell made with two-electrode design with a filter paper as the separator in 21 m LiTFSI electrolyte. (b) Impedance measurement results (c) A flexible, fully operational cell built by transferring two TiS2 composite-VACNT film structures onto Kapton tape with a filter paper as separator in LiTFSI/PVA/H_2O electrolyte. The cell can power a 2.2V LED for 60 seconds.

Table 3.1 TiS_2 composite-VACNT electrodes in different electrolytes. (NMP: N-Methyl-2-pyrrolidone)

V vs Ag/AgCl	Min potential (V)	Max potential (V)	Potential window (V)	Capacitance F/g (10mV/s)
0.5 M H_2SO_4	-0.2	1.0	1.2	10.4
1 m NaCl	-0.4	0.1	0.5	0.2
1 m LiCl	-0.4	1.0	1.4	18.75
10m LiCl	-0.5	1	1.5	30
20m LiCl	-1.3	1.05	2.35	80
1 m LiTFSI	-0.8	1.1	1.9	86
10m LiTFSI	-1	1.2	2.3	102
21 m LiTFSI	-1.3	1.7	3	120
1 m LiTFSI in NMP	-1.5	0.9	2.4	31.25

In this paper, we attribute the exceptional energy density of TiS_2-VACNT hybrid systems to the large working voltage window and intercalation-induced capacitance. Although some oxide materials (such as RuO_x and MnO_x) also provide high capacitance, smaller operation voltage windows in conventional acidic and basic electrolytes limit their energy density (**Table 2**). Using conventional organic solvent may promotes cell voltage by eliminating hydrolysis but low ionic conductivity and diffusion coefficient degrade the performance[32]. Since the aqueous electrolyte can be easily made in ambient conditions to eliminate possible safety issues, the TiS_2-VACNT composite electrode system with 21 m LiTFSI electrode is preferable to conventional Li^+-rich solutions for various systems. Three factors allow for exceptionally high energy density (reaching a maximum of 60.9 Wh/kg) for TiS_2-VACNT composite electrodes: (1) large electrochemical voltage window of 3 V due to the chemical stability of TiS_2 composite in ultra-high concentration, 21 m LiTFSI electrolyte; (b) effective intercalation of Li^+ into TiS_2-VACNT composite for high gravimetric capacitance of 195 F/g; and (c) nano-crystallinity of TiS_2 composite and ultra-high

surface area of VACNT framework promotes surface reactions instead of bulk behavior for a maximum power density of 1250 W/kg and cycleability of more than 10,000 charge/discharge cycles with >95% capacitance retention. TiS_2-VACNT composite electrodes are compared with prepared RuO_x-, MoS_2-, TiN- and VACNT electrode systems and compared with other published works of various high-performance oxide, chalcogenide, and MXENE energy storage systems. The TiS_2-VACNT composite electrode system in 21 m LiTFSI electrolyte achieves the highest maximum energy density among these supercapacitors. Furthermore, by decreasing the thickness of TiS_2 composite while increasing surface area of the highly porous VACNT network, we are able to achieve high power density. As a result, the large volumetric deformation during the charge/discharge operations is prevented to preserve the long-term stability of TiS_2 composite. So far, only a few graphene/activated graphene with extremely high surface area reported slightly higher energy density in organic electrolyte or ionic liquid [33 34]. With further efforts to modify the composition of TiS_2 composite and decrease the impurities/defects, the performance of hybrid TiS_2 composite-VACNT LiTFSI systems might be further enhanced.

Table 3.2 Comparisons of state-of-art high capacitance, high energy density materials

	Ref.	Electrode	Electrolyte	Material Capacitance (F/g)	Cell Voltage (V)	Energy (Wh/kg)
Metal Oxides	22	RuO_2	1M H_2SO_4	1300	1	45.1
	35	MnO_2	1M Na_2SO_4	1380	0.9	38.8
2D Metal Carbide/Sulfide	18	Ti_3C_2Tx	1M H_2SO_4	245	0.55	2.57
	36	MoS_2	0.5M Li_2SO_4	140	1	4.9
			1M $TEABF_4$	40	3.5	17
	This paper	TiS_2/CNT Composite	21m LiTFSI	195	3	60.9

3.4 Experiment Session

Synthesis of TiS_2-VACNT composite electrodes:A thermally grown silica layer on silicon serves as the basis of the VACNT substrate. A 50/10/5 nm Mo/Al/Fe thin film is evaporated as the catalyst layer and VACNTs are grown by CVD in a carbon-rich environment. The height (thickness) of the VACNT forest is controlled by processing time[8]. Alternatively, the VACNT electrodes are synthesized on a stainless-steel substrate with a passivation layer of atomic layer deposited (ALD) Al_2O_3 (Cambridge Fiji F200 Plasma ALD). The same ALD tool is used to coat TiN onto the VACNT framework, with TDMAT (0.05 s) and N_2 plasma (5 s, 300W) as precursors and 5 s argon purge at 300ºC. The TiN-VACNT forest is annealed in sulfur vapor at 150 ºC, 250 ºC, 300 ºC, or 350 ºC in a furnace (Lindbergh Thermal) for 30 minutes.

Synthesis of RuO_x-VACNT electrodes: RuOx is deposited onto the VACNT electrodes using ALD with bis(ethylcyclopentadienyl)ruthenium(II) ($Ru(EtCp)_2$) and oxygen (O_2) as precursors.

Pulse times for $Ru(EtCp)_2$ and O_2 are 1s and 10s, respectively, with 5s argon gas purge. During the ALD process, substrates were heated to temperatures ranging from 270 ºC to 400 ºC[12].

Synthesis of MoS_2-VACNT electrodes: MoS_2 is grown by a second CVD process, using stoichiometric sulfur and MoO_3 as precursors and 300sccm of Ar as the carrier gas. The holders for sulfur, MoO_3, and CNT are separated in different locations and heated to 400 ºC, 650 ºC and 650ºC, respectively.

Materials Characterization: Scanning electron microscopy (SEM, FEI Quanta 3D), Transmission electron microscopy (TEM, FEI Tecnai) are employed to study the morphology and structure of as-grown VACNT, TiN-VACNT, and TiS2 composite-VACNT. X-ray diffraction (XRD, Bruker D8) is performed to study the crystallinity and X-ray photoelectron spectroscopy (CHI) is used to study the surface element components of samples.

Electrochemical testing: Ag/AgCl is used as the reference electrode to study VACNT, TiN-, TiS2 composite-, RuO_x and MoS_2-VACNT electrode systems for comparisons in different electrolytes. Linear sweep voltammetry, cyclic voltammetry, chronopotentiometry, and EIS impedance tests are performed by an electrochemistry workstation (Gamry Ref 600) with different modules.

Specific Capacitance and Specific Energy Calculation:

The specific capacitance values were derived from the cyclic voltammetry measurements by[12]:

$$C_{sp} = \frac{\int_{V_1}^{V_2} i(V)dV}{(\Delta V)mv}$$; in which

$i(V)$: current density (A/g);

ΔV : voltage window(V); V_2, V_1 : initial and final voltage in CV.

m : electrode mass(g); v : scan rate (V/s).

Energy and power density were derived from the symmetric two-electrode model in which:

Energy Density (Wh/kg): $E = \frac{C_{sp}(\Delta V)^2}{8(3600)}$;

Power Density (W/kg): $P = \frac{3600E}{t}$; in which

ΔV : cell voltage (V);

t : discharge time (s);

Density measurement/estimation of TiS_2-VACNT, TiN-VACNT. RuO_x-VACNT, and MoS_2-VACNT.

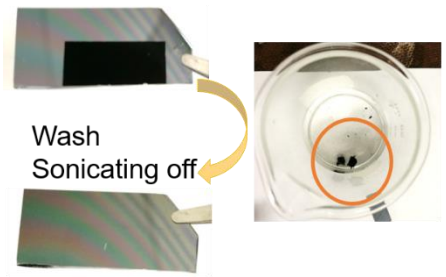

Test	Before mg	After mg
1	459.5	451.2
2	459.9	450.9
3	459.8	451.1
Average	459.7	451.1
Sample area: 2.53cm^2; Height: 40±3.5μm		

Figure 3.16 (Left) illustration of TiS_2-VACNT density measurement. (Right) mass change.

As illustrated in **Figure 3.16**, the density of TiS_2-VACNT is calculated as 0.849 g/cm^3. Referring to a similar estimation method in a former paper[12], mass density of VACNT is 9.1×10^{-3} mg/cm^2-μm with a number density of 41 CNTs/ μm^2, and diameter 13±5nm. The density of RuO_x-VACNT with outside diameter of 64nm is ~0.85g/cm^3, and the TiN-VACNT is calculated as below. Density of MoS_2-VACNT is measured similarly with TiS_2-VACNT composite, in which weight of wafer is measured before and after washing out the as grown MoS_2-VACNT. By deriving the sample surface are and height of CNT, the density is estimated as ~1.0 g/cm^3.

As-deposited TiN-VACNT (500 cycles ALD)	
Mass of TiN per CNT	$M_{TiN} = \frac{1}{4}\pi\left(d_{TiN-CNT} - d_{CNT}\right)^2 \rho_{TiN} = 5.8\times10^{-14} g/\mu m/CNT$
Density of TiN	$\left(41\ CNT/\mu m^2\right)\times(5.8\times10^{-14} g/\mu m/CNT) = 0.2378 mg/cm^2\mu m$
Density of TiN-VACNT	$0.2378 mg/cm^2\mu m + 9.1\times10^{-3} mg/cm^2\mu m = 0.2468\ mg/cm^2\mu m$ $\sim 0.25\ mg/cm^2\mu m = 2.5\ g/cm^3$

Reference

1. M. Pumera and A. H. Loo, *Trac-Trend Anal Chem*, 2014, **61**, 49-53.
2. J. Zhang, S. H. Liu, H. W. Liang, R. H. Dong and X. L. Feng, *Adv Mater*, 2015, **27**, 7426-+.
3. S. Y. Chen, C. X. Zheng, M. S. Fuhrer and J. Yan, *Nano Lett*, 2015, **15**, 2526-2532.
4. G. A. Muller, J. B. Cook, H. S. Kim, S. H. Tolbert and B. Dunn, *Nano Lett*, 2015, **15**, 1911-1917.
5. Z. W. Seh, J. H. Yu, W. Y. Li, P. C. Hsu, H. T. Wang, Y. M. Sun, H. B. Yao, Q. F. Zhang and Y. Cui, *Nat Commun*, 2014, **5**.
6. E. A. Suslov, O. V. Bushkova, E. A. Sherstobitova, O. G. Reznitskikh and A. N. Titov, *Ionics*, 2016, **22**, 503-514.
7. E. J. Frazer and S. Phang, *J Power Sources*, 1981, **6**, 307-317.

8. Y. Q. Jiang, P. B. Wang, X. N. Zang, Y. Yang, A. Kozinda and L. W. Lin, *Nano Lett*, 2013, **13**, 3524-3530.
9. M. S. Whittingham and J. A. Panella, *Mater Res Bull*, 1981, **16**, 37-45.
10. J. Chen, S. L. Li, Z. L. Tao and F. Gao, *Chem Commun*, 2003, DOI: 10.1039/b300054k, 980-981.
11. V. Pore, M. Ritala and M. Leskela, *Chem Vapor Depos*, 2007, **13**, 163-168.
12. R. Warren, F. Sammoura, F. Tounsi, M. Sanghadasa and L. W. Lin, *J Mater Chem A*, 2015, **3**, 15568-15575.
13. E. Kao, C. Yang, R. Warren, A. Kozinda and L. W. Lin, *Sensor Actuat a-Phys*, 2016, **240**, 160-166.
14. L. M. Suo, O. Borodin, T. Gao, M. Olguin, J. Ho, X. L. Fan, C. Luo, C. S. Wang and K. Xu, *Science*, 2015, **350**, 938-943.
15. L. Smith and B. Dunn, *Science*, 2015, **350**, 918-918.
16. P. Simon and Y. Gogotsi, *Nat Mater*, 2008, **7**, 845-854.
17. M. Acerce, D. Voiry and M. Chhowalla, *Nat Nanotechnol*, 2015, **10**, 313-318.
18. M. Ghidiu, M. R. Lukatskaya, M. Q. Zhao, Y. Gogotsi and M. W. Barsoum, *Nature*, 2014, **516**, 78-U171.
19. J. P. Liu, J. Jiang, C. W. Cheng, H. X. Li, J. X. Zhang, H. Gong and H. J. Fan, *Advanced Materials*, 2011, **23**, 2076-+.
20. G. H. Yu, L. B. Hu, M. Vosgueritchian, H. L. Wang, X. Xie, J. R. McDonough, X. Cui, Y. Cui and Z. N. Bao, *Nano Letters*, 2011, **11**, 2905-2911.
21. Y. X. Xu, Z. Y. Lin, X. Zhong, X. Q. Huang, N. O. Weiss, Y. Huang and X. F. Duan, *Nat Commun*, 2014, **5**.
22. C. C. Hu, K. H. Chang, M. C. Lin and Y. T. Wu, *Nano Letters*, 2006, **6**, 2690-2695.
23. M. Toupin, T. Brousse and D. Belanger, *Chem Mater*, 2004, **16**, 3184-3190.
24. J. Musschoot, Q. Xie, D. Deduytsche, S. Van den Berghe, R. L. Van Meirhaeghe and C. Detavernier, *Microelectron Eng*, 2009, **86**, 72-77.
25. S. W. Choi, C. M. Jang, D. Y. Kim, J. S. Ha, H. S. Park, W. Koh and C. S. Lee, *J Korean Phys Soc*, 2003, **42**, S975-S979.
26. A. Lewandowski, A. Olejniczak, M. Galinski and I. Stepniak, *J Power Sources*, 2010, **195**, 5814-5819.
27. M. Lovric, M. Hermes and F. Scholz, *J Solid State Electr*, 1998, **2**, 401-404.
28. S. D. Tilley, M. Schreier, J. Azevedo, M. Stefik and M. Graetzel, *Adv Funct Mater*, 2014, **24**, 303-311.
29. D. H. Deng, K. S. Novoselov, Q. Fu, N. F. Zheng, Z. Q. Tian and X. H. Bao, *Nat Nanotechnol*, 2016, **11**, 218-230.
30. Y. J. Han, X. Yue, Y. S. Jin, X. D. Huang and P. K. Shen, *J Mater Chem A*, 2016, **4**, 3673-3677.
31. V. Augustyn, P. Simon and B. Dunn, *Energ Environ Sci*, 2014, **7**, 1597-1614.
32. M. Chintapalli, K. Timachova, K. R. Olson, S. J. Mecham, D. Devaux, J. M. DeSimone and N. P. Balsara, *Macromolecules*, 2016, **49**, 3508-3515.
33. Y. W. Zhu, S. Murali, M. D. Stoller, K. J. Ganesh, W. W. Cai, P. J. Ferreira, A. Pirkle, R. M. Wallace, K. A. Cychosz, M. Thommes, D. Su, E. A. Stach and R. S. Ruoff, *Science*, 2011, **332**, 1537-1541.
34. C. G. Liu, Z. N. Yu, D. Neff, A. Zhamu and B. Z. Jang, *Nano Letters*, 2010, **10**, 4863-4868.

4 Chapter: Direct Laser Synthesis of Two-Dimensional Transition Metal Carbides in Ambient Environment

Keywords: Laser ablation; nanoflake; transition metal carbides; molybdenum/tungsten carbide; supercapacitor; harsh environment.

4.1 Abstract

Recent scientific and technological advancements have successfully synthesized structurally two-dimensional metal carbides bringing the conventionally bulky TMCs to graphene-like materials for potential applications as superconductors and catalysts as well as energy storage and light-phonon systems. However, large-scale synthesis of high quality TMCs remains a challenge. We address and develop a method for the direct synthesis of ultrathin metal carbides by using laser ablation. The process involves using a CO_2 Infrared (IR) laser to ablate transition metal ions embedded in a gel solution of a biocompatible polymer. This approach can successfully produce TMCs (such as MoC_x, WC_x and CoC_x) of metastable phases, including Mo_3C_2 and β-W_2C, which generally require extremely high energy. Local temperatures of above 1900 K can be reached with this method by using an IR laser in ambient conditions. The lattice structures of the laser induced Mo, W and Co carbides are thin with the form of 2D flakes, their meso-scale 3D structures are 'sponge-like'. The resulting hierarchical porous structure is conductive with high surface area - two desirable characteristics as electrodes in energy storage applications. For example, experimental tests have revealed that the gravimetric capacitance of laser-induced Mo_3C_2 can reach 100 F/g, while the higher thermal stability of refractory materials enable exceptional stable behavior of the supercapacitor from -50 ºC to 300 ºC using semi-solid LiTFSI-PVA as electrolyte. This is a broad operation range achieved by a non-ceramic supercapacitor system.

4.2 Introduction

Transition metal carbides, such as tungsten carbide and molybdenum carbide, are classified as metallic conductor owing to their 10^1 μΩ cm resistivity[1]. Carbides such as Mo_2C, WC and Co_3C have melting points above 2500 K and high Young's modulus on the order of 10^2 GPa, which makes them ideal materials for applications in harsh environmental conditions especially as electrodes in high temperature and high pressure environments[1]. Recently, 2D transition metal carbides (MXenes), a new class of material, have been demonstrated to provide high specific capacity [2, 3]. Unfortunately, the fabrication process of MXenes, including temperatures as high as 1600 ºC to a MAX phase powder followed by an HF etching[4], is rather complex and tedious. MAX phase is the shorten form for $M_{n+1}AX_n$, where M represents transition metal ions and X is either C or N[5]. The first and most commonly developed routine for the MXENE fabrication starts from the MAX phase, which is later etched by HF to remove the A layer to form $M_{n+1}X_nT_x$(T: OH, OOH and other surface termination groups)[3]. MAX structures derived MXENEs have shown exceptional energy storage capability due to their high surface area, high conductivity, and rich surface

functional groups[6]. Even though up to tens of MAX phases mainly in the 312 family have been discovered, the materials 211 family are much broader and there are also other higher order MAX phase family as shown in **Table 4.1**.

Table 4.1 Current $M_{n+1}AX_n$ phases, ("211", "312", and "413") and valence electron configuration for the M and A elements[7].

A element	s^2 (group 12)	s^2p^1 (group 13)	s^2p^2(group 14)	s^2p^3(group 15)	s^2p^4(group 16)
211 phases					
M 3*d*	Ti_2CdC	Sc_2InC			Ti_2SC
		Ti_2AlC	Ti_2GeC		
		Ti_2GaC	Ti_2SnC		
		Ti_2InC	Ti_2PbC		
		Ti_2TlC			
		V_2AlC	V_2GeC	V_2 PC	
		V_2GaC		V_2AsC	
		Cr_2AlC	Cr_2GeC		
		Cr_2GaC			
		Ti_2AlN			
		Ti_2GaN			
		Ti_2InN			
		V_2GaN			
		Cr_2GaN			
M 4*d*		Zr_2InC	Zr_2SnC		Zr_2SC
		Zr_2TlC	Zr_2PbC		
		Nb_2AlC	Nb_2SnC	Nb_2PC	Nb_2SC
		Nb_2GaC		Nb_2AsC	
		Nb_2InC			
		Mo_2GaC			
		Zr_2InN			
		Zr_2TlN			
M 5*d*		Hf_2InC	Hf_2SnC		Hf_2SC
		Hf_2TlC	Hf_2PbC		
		Ta_2AlC	Hf_2SnN		
		Ta_2GaC			
312 phases					
M 3*d*		Ti_3AlC_2	Ti_3SiC_2		
		V_3AlC_2 (or $(V,Cr)_3AlC_2$)	Ti_3GeC_2		
			Ti_3SnC_2		
M 5*d*		Ta_3AlC_2			
413 phases					
M 3*d*		Ti_4AlN_3	Ti_4SiC_3		
		V_4AlC_3	Ti_4GeC_3		
		Ti_4GaC_3			
M4d		Nb_4AlC_3			
M5d		Ta_4AlC_3			

In general, the family of transition metal carbide materials is much larger than the MAX phase family, as many carbides with different stoichiometry cannot be derived from MAX phase. The existing of MAX phase depends highly on the kinetic stability, as well as the competing stability

of other phases [8]. For example, Mo_3C_2 is one of many Molybdenum carbide phases but there is no reported or known Mo_3AC_2 phase. Meanwhile, although Tungsten carbide is very hard and stiff as widely applied for the protection of machine tools, there is no report on tungsten based MAX. Other methods to make two-dimensional transition metal carbides include chemical vapor deposition and solution based reactions[9, 10]. Herein, we demonstrate a versatile process to fabricate transition metal carbides by using a laser to speedily convert the embedded ions in a self-assembled hydrogel network (**Figure 4.1**). Both transition metal ions and polymer can absorb IR laser energy, to generate temperatures up to 2000 K within a short time of of 5×10^{-5} seconds[11] to "explosively" vaporizes solvent and part of the materials leading to the observed nanoscale porosity and a carbonized metal/gel matrix.

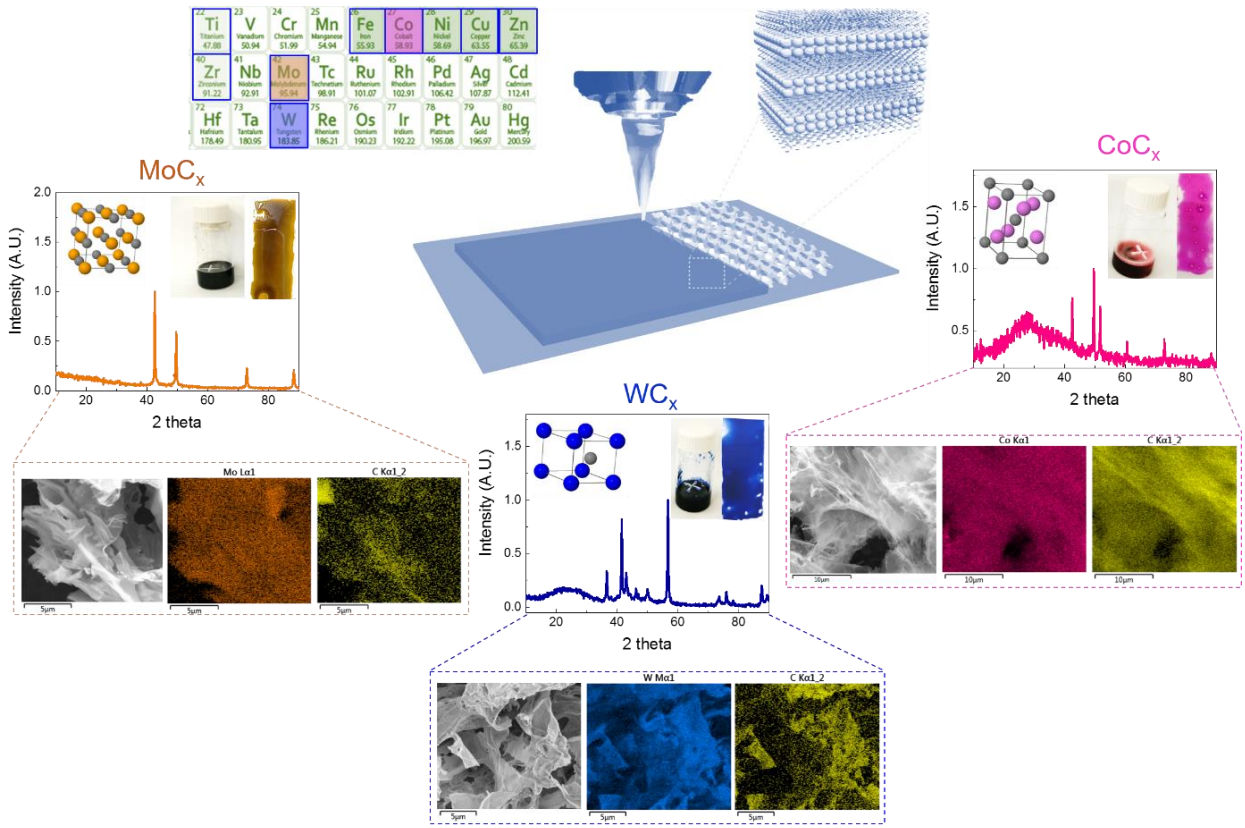

Figure 4.1 Schematic of the process for laser-induced transition metal carbides. The X-ray diffractograms and SEM images of MoC_x, WC_x, and CoC_x produced show highly porous flake structures with thin thickness.

4.3 Results and Discussion

Different metal ions with a concentration of 2M have been dissolved in DI water together with 60 wt% percent of gelatin. The solution is then spin-coated onto a substrate and heated at 80ºC for 30min to induce a layer-by-layer, self-assembly process for the gelatin[12]. The resulting film has smooth surface of 100µm in thickness as shown in **Figure 4.1**. Using Mo^{5+} ion precursor as an example, ultrathin carbide sheets with a composition of Mo_3C_2 are formed after the ablation by CO_2 laser (wavelength of 10.6µm), as shown in **Figure 4.2**. Graphene is also observed based on

the Raman spectrum analysis. The carbide sheet consists of nanoparticles with different orientations as observed in the diffraction pattern analysis and the typical particle size is around 5~10 nm. We attribute the "2D" flake formation to two key mechanisms: (a) the layer-by-layer assembly of the gelatin network due to the triple helical nature of gelatin which has been demonstrated before in the self-assembly process [12] as the scaffolds; (b) both gelatin and the specific metal ion have high IR absorption in the specific wavelength range to achieve high reaction temperature. The laser power and duration (speed) also affect the heating process and temperature and it can be analyzed using a first-principle heat transfer model. The temperature distribution is circular and symmetric as shown in Finite Element Analysis results (**Figure S4.1-S4.3**). The approximate time scale of the ambient plasma interaction to from particles is estimated within the range of μs to ms[13].

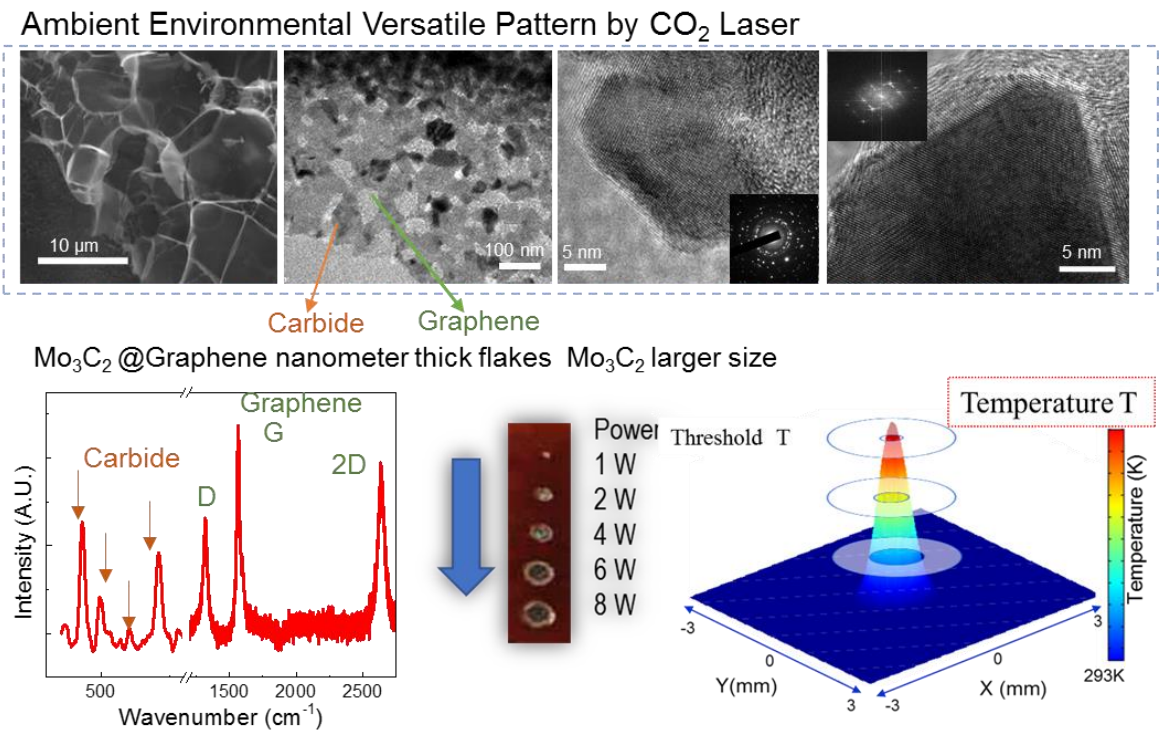

Figure 4.2 Characterizations of laser ablated Mo-gelatin gel. (**Top**) SEM and Low resolution TEM of ablated Mo-gelatin, and High resolution TEM of laser ablated Mo_3C_2, illustrating the fcc crystal lattice of Mo_3C_2. (**Bottom left**) Raman spectrum showing vibration at low wavenumber (carbide), and typical graphene peaks. (**Bottom right**) Typical temperature distributions for the laser ablation process.

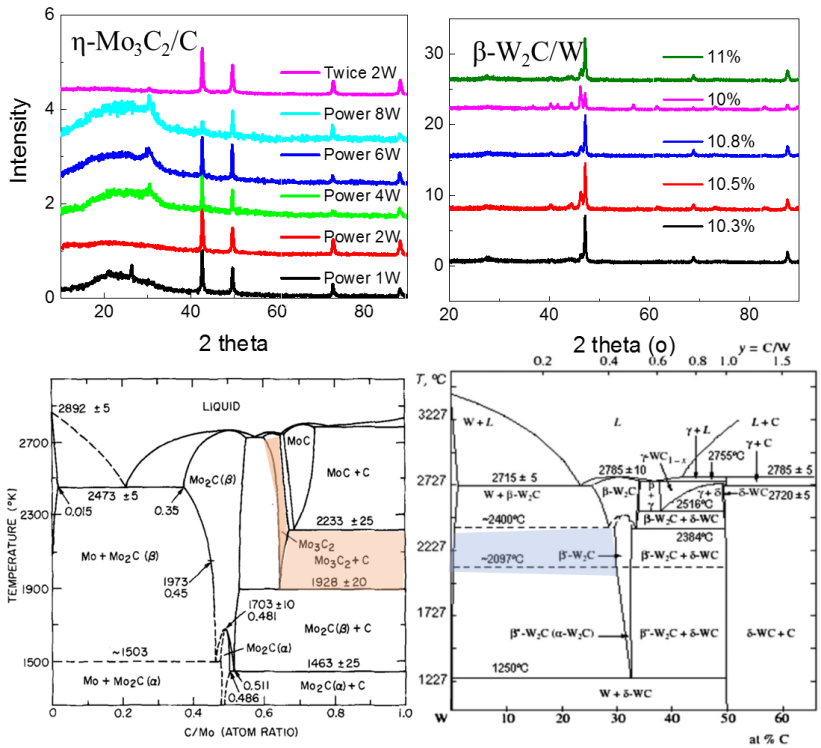

Figure 4.3 (**Top**) Meta-stable phase of Molybdenum and Tungsten carbide from XRD characterizations, (% corresponds to laser power percentage 100%=40W). (**Bottom**) phase diagram of Mo-C and W-C.

Traditional methods for depositing Mo and W carbide thin films include chemical reaction of metals with CH_4/H_2 gas and the reactive sputter deposition using the glow discharging methods such as metal organic chemical vapor deposition (MOCVD) and combustion synthesis[1]. A rapid initial uptake can sometimes lead to the formation of the carbon-deficient, metastable phase of Mo/W and C composites instead of the thermodynamically stable MoC_x/WC_x phases. Once the metastable phase is formed, it can lead to the coarsening of particles and degradation of the nano-structure. Metastable phases of transition metal carbides have been synthesized via pulsed-laser-induced reactive quenching at liquid-solid interfaces[14]. Synthesized and isolated metastable phase metal carbides generally require extremely high energy as previously performed. As shown in **Figure 4.3**, the product of η-Mo_3C_2/C has much higher Gibbs free energy than the common α-Mo_2C and β-Mo_2C. In order to form Mo_3C_2, the temperature could reach over 1900K. Similarly, the β-W_2C/W phases also require higher energy, temperature, and high carbon uptake from the phase diagram. The process of laser ablation can produce Molybdenum carbides with a wide process window in the tested parameters from 1W to 8W of laser power (**Figure 4.3**). The residual amorphous carbon amount (from the XRD analysis) are minimized for an applied power of 2W for the best yield of pure Mo_3C_2. The peak shift measured from 28° (at 1W) to 32° (at 4-8W) relates to the formation of graphite from accumulated graphene. Similarly, the change is laser power results in similar tungsten phase and the W concentration varies as over ablated W_2C could decompose back to carbon and tungsten while further studies are required.

Figure 4.4 shows the concentration of gelatin is essential to form metal carbides. High concentration of gelatin above a threshold can result in metal carbides in the form of Mo_3C_2, while

low concentration of gelatin (below 10%) and result in MoO_2 and lower energy Mo_2C. Low concentration of gelatin increases the oxidation process instead of the carbonization process. Such phenomena could be attribute to a few possibilities: the salting out effect Mo in between layers of gelatin template requiring lots of gelatin "ligands" for the carbonization process and the absorption of IR by gelatin plays an essential role to raise the temperature for the right conversion process. Different types of polymer are also studied, including gelatin, Polyvinylpyrrolidone (PVP) and Polyethylene glycol (PEO) and it is found that only gelatin can produce ultrathin metal carbides with nanoscale flake structures. Gelatin, being a combination of peptides, contains a lot more functional groups than PVP and PEO, such as amino groups, hydroxyl groups, carboxyl groups and more[15], which can effectively coordinate with transition metal ions (such as Mo^{5+}). Triple helix chains in gelatin can fold and unfold in response to temperature to form highly ordered 2D structures by the self-correcting assembly process. As a result, the conversion of transition-metal ions takes place between the layers of gelatin scaffolds to nanometer thick connecting sheets. Furthermore, the IR absorption of PVP/PEO is lower than gelatin and this decreases the process temperature. In the simplified model, it was assumed that the chemical reaction takes place within a time constant of 10μs[16]. With an ablation time of 5×10^{-5} s (50 μs), PVP-Mo and PEO-Mo can only generate much lower temperature.

Figure 4.4 shows the Mo-gelatin composite has the highest IR absorption at the typical wavelength at 10.6 μm as compared with Mo-PVP and Mo-PEO solutions. The strong interaction of transition metal d orbital with polymer matrix at the wavelength of the IR laser help raise the temperature for the successful conversion of metal carbides. For example, both W^{6+} and Co^{2+} gelatin mixtures have been successfully demonstrated to form metal carbides in the form of MC_x (M = W, Co). Among the metal ions in the periodic table in **Figure 4.1**, Mo, W, Co are found to be good materials to make metal carbides in the preliminary tests. One key reason is the strong far-IR absorption (10.6 μm for CO_2 laser) by the metal-gelatin complex to generate high temperature. Specifically, Mo^{5+} ions have the [Kr]4d1 ground state, of which the degeneracy of d-orbital can induce a strong absorption band near 1000 cm^{-1}(10 μm). The W^{5+} ion with a same shell band structure can be reduced from W^{6+} also contributes strong absorption in the far-IR range. On the other hand, preliminary experimental results show good absorption of the Co^{2+}-gelatin complex in the far-IR range over the pure Co^{2+} ions probably due to the strong ligand-Co stretching and vibration in the matrix material. Both **Table 4.2** and **Figure 4.5** summarize results on various metal ions mixed with different polymers under the CO_2 laser. Metal ions in the same group with similar band structure results in similar product after the laser ablation process (W/Mo, Fe/Ni, Ti/Zr). The Ti^{4+} and Zr^{4+} in the gelatin hydrogel are converted to composite materials of both carbide and oxide while Ni^{2+} and Fe^{3+} are converted to metal oxide with small portions of carbide. On the other hand, Zn^{2+} doesn't produce crystalline phase. We attribute these to two key mechanisms: (a) "effectiveness" of energy absorbed by the metal-gelatin template which is decided by the absorption of ion, polymer and metal-ligand interactions; and (b) the activation energy of carbonization and the reduction reactions. Using Mo^{5+} and Ti^{4+} as two examples, Mo-gelatin can be effectively converted to Mo_3C_2 for temperature above 2000 ºK, while the ineffective energy conversion in the Ti-gelatin solution only activates the reduction process to a more stable TiO_4 phase.

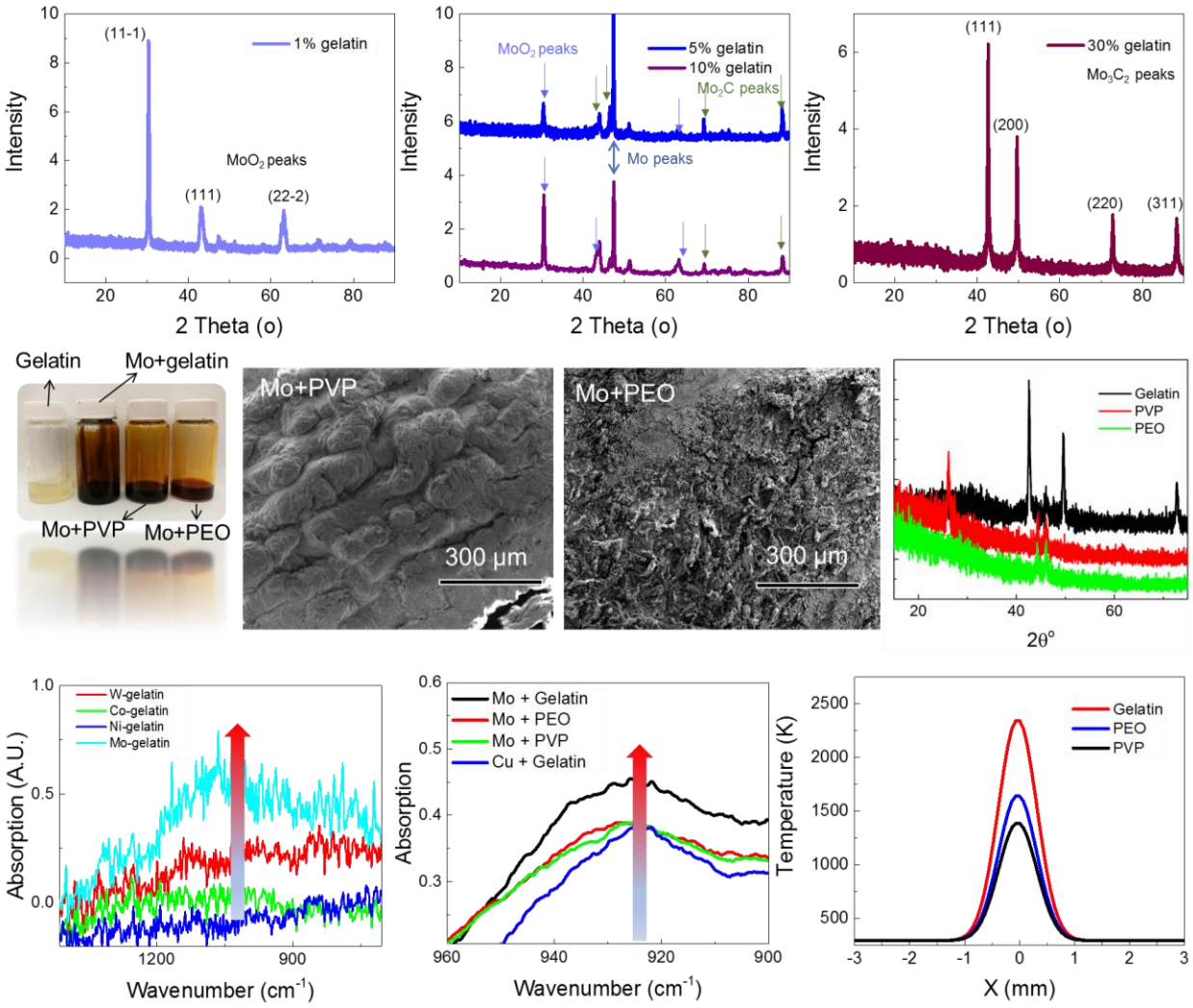

Figure 4.4 (**Top**) Laser ablation product from 2M Mo^{5+} gel with difference concentration of gelatin. (**Middle**) Comparison of gelatin, PVP and PEO as the mixing solutions in Mo-rich hydrogel and the laser ablation results. Optical image of the Mo-gelatin, Mo-PVP, and Mo-PEO and SEM images of Mo-PVP, Mo-PEO after 2W laser ablation showing no obvious porous structures. XRD analyses showing only Mo-gelatin mixture can produce Mo_3C_2. (**Bottom**) FT-IR absorption of different Mo-polymer complex, showing higher absorption of Mo-gelatin at 10.6 μm. Simulated temperature of Mo-Gelatin assuming the activation time constant is 5×10^{-5}s, showing a Gaussian distribution of temperature. Temperature profile of Mo-gelatin, Mo-PVP and PEO-PVP ablated by a 2W IR laser, with a focus radius of 100 μm (0.2 mm in diameter).

Table 4.2 Summary of the composition of various tested hydrogels and their obtained products with laser ablation.

Salt Precursor	Solvent	Polymer media	Product
$MoCl_5$ (2M)	DI water	Gelatin	Mo_3C_2
$MoCl_5$ (2M)	DI water	PVP	NA
$MoCl_5$ (2M)	DI water	PEO	NA
WCl_6 (1M)	NMP	Gelatin	W_2C+WC
$CoSO_4$(2M)	DI water	Gelatin	Co_2C+Co
$NiSO_4$(2M)	DI water	Gelatin	Ni+NiO_x+NiC_x
$FeCl_3$ (2M)	DI water	Gelatin	Fe+FeO_x+FeC_x
$Zr(NO_3)_4$ (2M)	DI water	Gelatin	ZrC+ZrO_2
$Zn(NO_3)_2$ (2M)	DI water	Gelatin	NA
Tetrabutyl Titanate	NMP	Gelatin	TiC+TiO_2

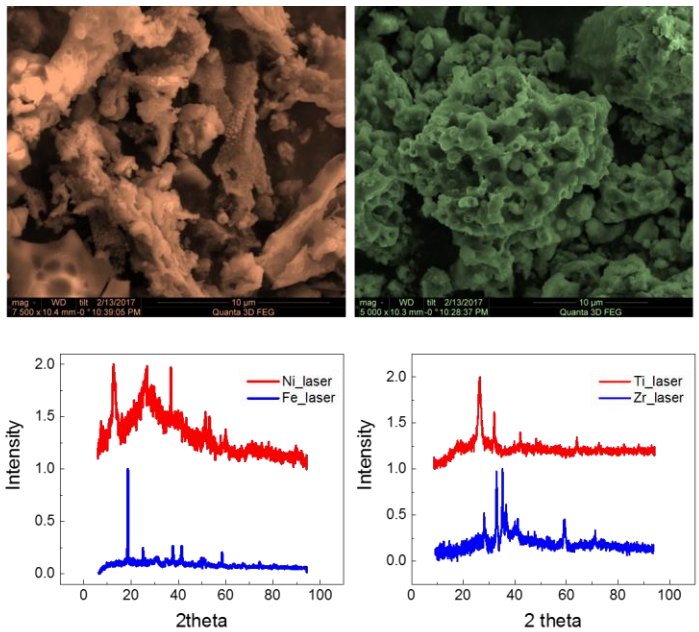

Figure 4.5 (**top-left**) and (**top-right**) SEM images of particles and structure of laser ablated iron-gelatin and nickel-gelatin films. (**bottom-left**) XRD of samples in (**top-left**) and (**top-right**). (**bottom-right**) XRD of oxide/carbide hybrid by using the Ti^{4+} and Zr^{4+} precursor.

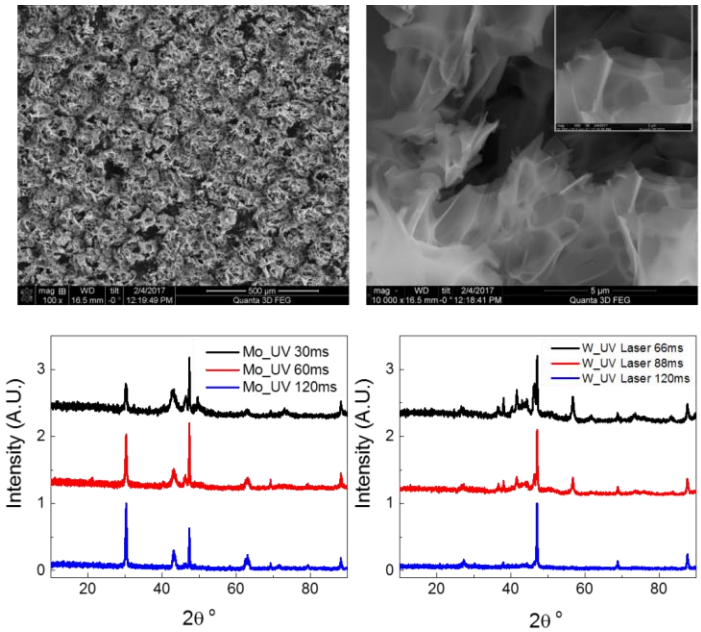

Figure 4.6 SEM of fabricated metal/metal oxide film by using a UV laser. (**top-left**) and (**top-right**) SEM image of UV laser ablated Mo-gelatin template. The inter-pulse distance in UV laser is much higher than in the IR laser, and thus induced separated "sculpture" rather than continuous film. (**bottom-left**) XRD of Mo-gelatin with different burning time, showing consist product of $Mo/MoO_2/Mo_2C$ composites. (**bottom-right**)) XRD of W-gelatin with different exposure time, showing consist product of $WC/W/WO_3$ composites.

Results from UV laser of 1 Watt ablated Mo-gel and W-gel show metal/oxide/carbide composistes instead of carbide phases (**Figure 4.6**). The hypothesis is that UV laser induces less thermal effect as it is generally used in photovoltaic applications rather than photothermal applicatons and the induced temperature is much lowered than the synthesis temperature for metal carbides. Furthermore, the typical time constant of the photovoltaic reactions is shorter than the photothermal process, while the coupled , reduction, decomposition and thermal dissipation processes make the long duration heating process quite complicated and complex for the analyses.

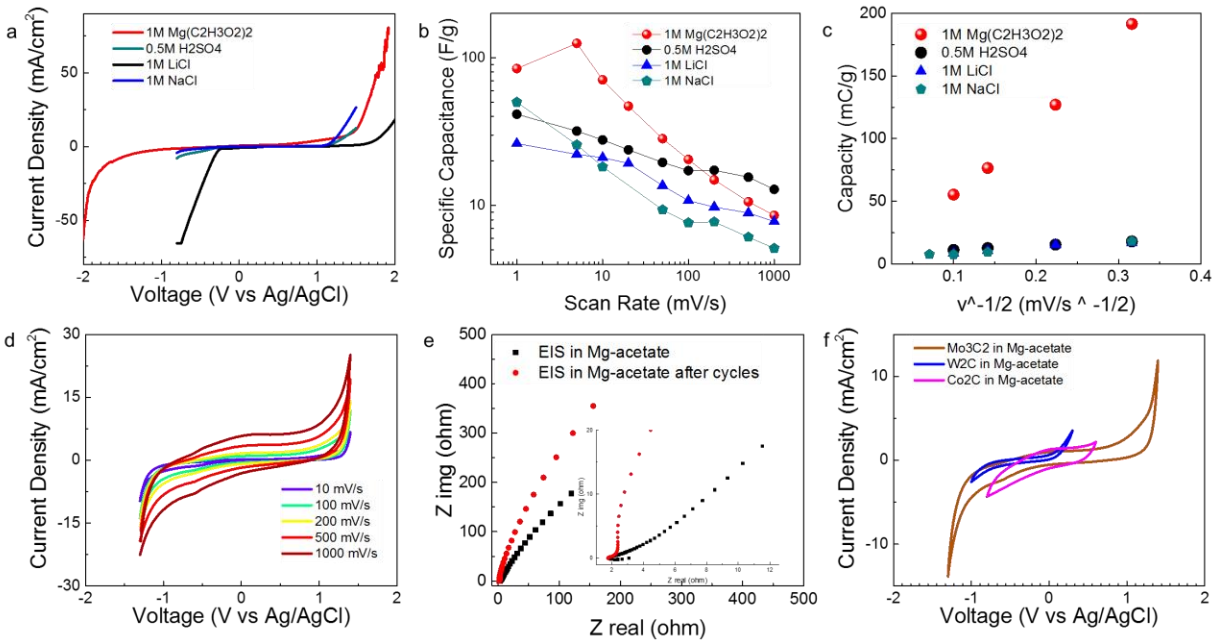

Figure 4.7 Energy storage capability of carbide material in different electrolytes. (a) Linear sweep voltamentry results of Mo_3C_2 electrode in magnesium acetate, sodium chloride, sulfuric acid and lithium chloride. (b) &(c) strong intercalation of Mo_3C_2 with Mg^{2+} based electrolyte, leading high specific capacitance. (d) Cyclic voltammetry performance of Mo_3C_2 electrodes in the Mg^{2+} electrolyte. (e) EIS of (d). (f) Mo_3C_2 outperform the other two carbides in the Mg^{2+} solution.

As fabricated metal carbide can be casted onto a carbon paper with 1% binder of PVDF dissolved in NMP to test their electrochemical energy storage performances in four electrolytes. Using molybdenum carbide (Mo_3C_2) as an example, the porous structure provides exceptionally high surface area and exposed edges, which result in a high specific capacitance up to 100 F/g in 1M Mg-acetate, **Figure 4.7**. Comparing to other electrolyte for the Mo_3C_2 electrode, Mg-acetate shows the highest specific capacitance, which is due to the stronger intercalation of Mo_3C_2 with Mg^{2+} ions[17]. While the Mg-acetate also broaden the stable electrochemical window to result in higher energy density. In addition, during the high temperature ablation process, some of the gelatin scaffold is partially converted to graphene to help improving the flexibility and conductivity. The process can be conducted by spin-coating the Mo-gelatin solution on a polyimide (PI) tape to construct Mo_3C_2 electrodes directly onto a flexible substrate by laser ablation as shown in **Figure 4.8**.

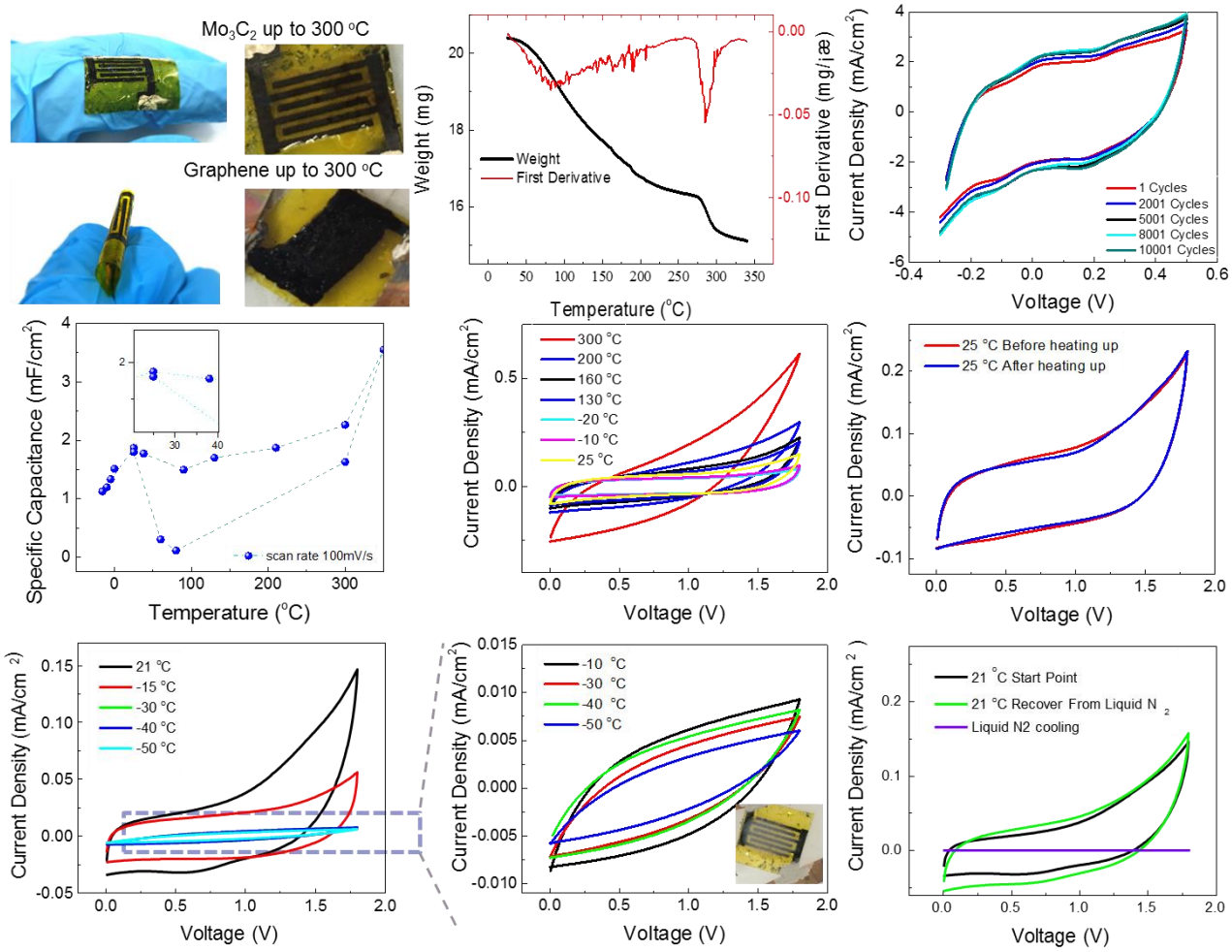

Figure 4.8 Electrochemical applications of Mo_3C_2. (a) Pictures of a flexible supercapacitor engraved onto a PI tape. The molybdenum carbide electrodes could withstand a high temperature of 300 ºC while the laser ablated graphite fails to work at high temperature. (b) TGA of the high a concentration Li electrolyte (LiTFSI 20m, 5%PVA), showing stability up to 300 ºC. (c) Long term stability of supercapacitors made of Mo_3C_2 in 0.5M H_2SO_4 electrolyte for 10,000 cycles. (d) Specific capacitance recovers during the temperature cycle. (e,f) High temperature performance of the Mo_3C_2 electrodes. (g-i) Low temperature performance of the Mo_3C_2 electrodes.

The converted film achieves low electrical resistivity around 50 Ω/□ and the micro supercapacitor prototypes has good specific capacitance under a discharge rate of 1mV/s in 0.5 M H_2SO_4, with a cycling life of more than 10,000 cycles (**Figure 4.9**). The good stability of the carbide allows the micro supercapacitor to operate over a wide temperature range, using a 5% PVA and 20M Li+ ion as the electrolyte. It is believed that Mo_3C_2 can intercalate with Li+ ions with good thermal stability. As an example, supercapacitors based solely on laser induced graphene[18] were degraded and shorted during high temperature tests at 300 ºC. On the other hand, supercapacitors based on Mo_3C_2 electrodes show little changes in the cyclic voltammetry (CV) measurements at 25 ºC before and after heating up to 300 ºC (**Figures 4.9e,f**). Experimental tests

are also carried out at low temperatures to reveal that the Mo_3C_2-based supercapacitor maintains functionality down to -50 ºC, with no irreversible damages to the electrodes as the recovery of the CV curves after defrosting. However, the measurements showed a sharp decay in capacitance below -30 ºC due to the low ion mobility in the freezing electrolyte.

4.4 Experimental Sessions

Preparation of transition metal ion and hydrogel solutions: $MoCl_5$, WCl_6, $CoSO_4$, $NiSO_4$, $FeCl_3$, $Zr(NO_3)_4$, $Zn(NO_3)_2$ (all purchased from Sigma Aldrich) were dissolved in DI water or NMP with a concentration of 2M. The hydrogel was made by dissolving the chemical solutions in either gelatin, PVP or PEO with 60% wt concentration.

Synthesis of metal carbide by laser ablation: the metal-gel precursor was spin-coated onto a glass substrate and cured at 80 ºC for 1 hr to make a thin film, which was subsequently ablated by laser (IR 2W; UV 1W).

Materials Characterization: Scanning electron microscopy (SEM, FEI Quanta 3D), Transmission electron microscopy (TEM, FEI Tecnai) were employed to study the morphology and structure. X-ray diffraction (XRD, Bruker D8) was performed to study the crystallinity, and X-ray photoelectron spectroscopy (CHI) was used to study the surface element components of samples.

Electrochemistry test: Ag/AgCl was used as the reference electrode to study prototype supercapacitors using fabricated metal carbides as electrodes in different electrolytes. Linear sweep voltammetry, cyclic voltammetry, chronopotentiometry, and EIS impedance tests were performed by an electrochemistry workstation (Gamry Ref 600) with different modules

4.5 Appendix

Temperature Simulation

Material setups

	Density (Kg/m^3)	Thermal conductivity (W/m·K)	Specific Heat (J/Kg·K)	Absorption at 10.6μm (a.u.)	Simulation Heat Power (W) (set 4W)
$MoCl_5$+Gelatin	720	0.375-0.61 [1]	1600 [2]	0.35	1.4
$MoCl_5$+PVP	1144	0.27 [3]	3963 [4]	0.32	1.28
$MoCl_5$+PEO	1210	0.15	2974-3410 [5]	0.31	1.24

Simulation setups

- Equivalent heat source: Gaussian Pulse

- Physics: Heat Transfer in Solids (including radiative transfer)
- Mesh type: Physical standard, fine size from 2.0E-6 to 2.0E-5m
- Laser spot radius: 0.1mm (200µm)
- Cutting speed: neglect
- Emissivity: 0.8

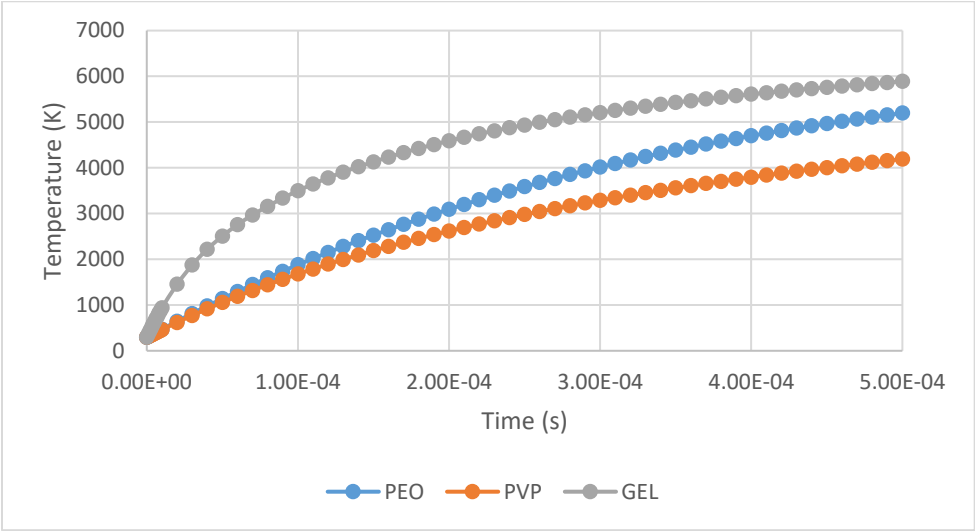

Figure S4.1: Temperature versus time (time interval: 1e-5s, 0 to 5E-4s)

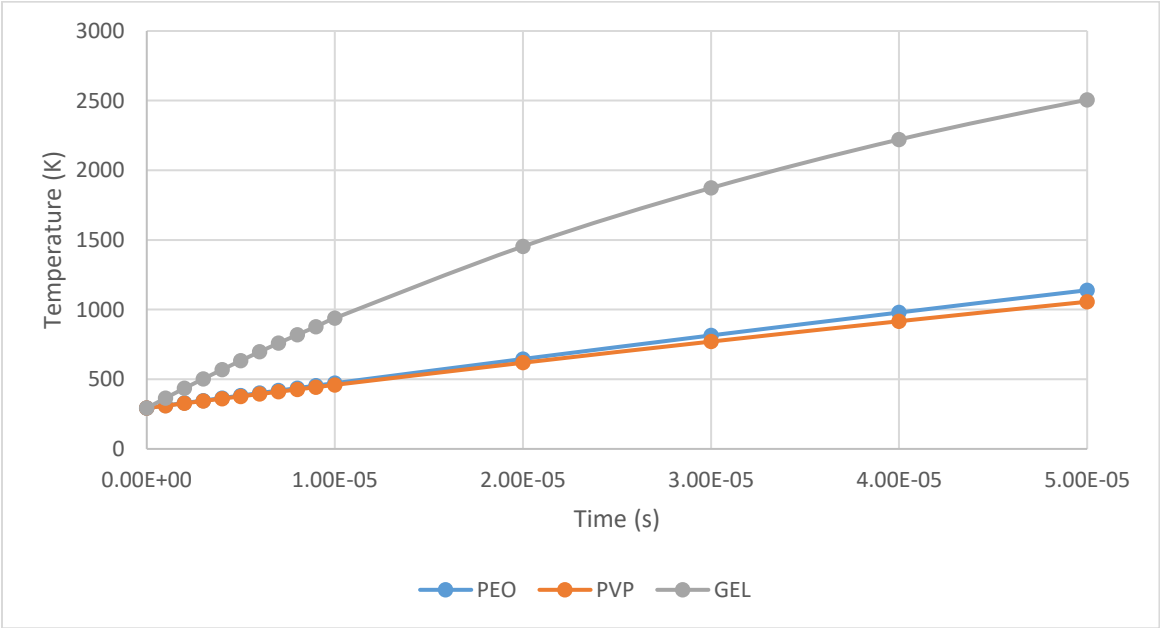

Figure S4.2: Temperature versus time (time interval: 1E-6s, 0 to 5E-5s)

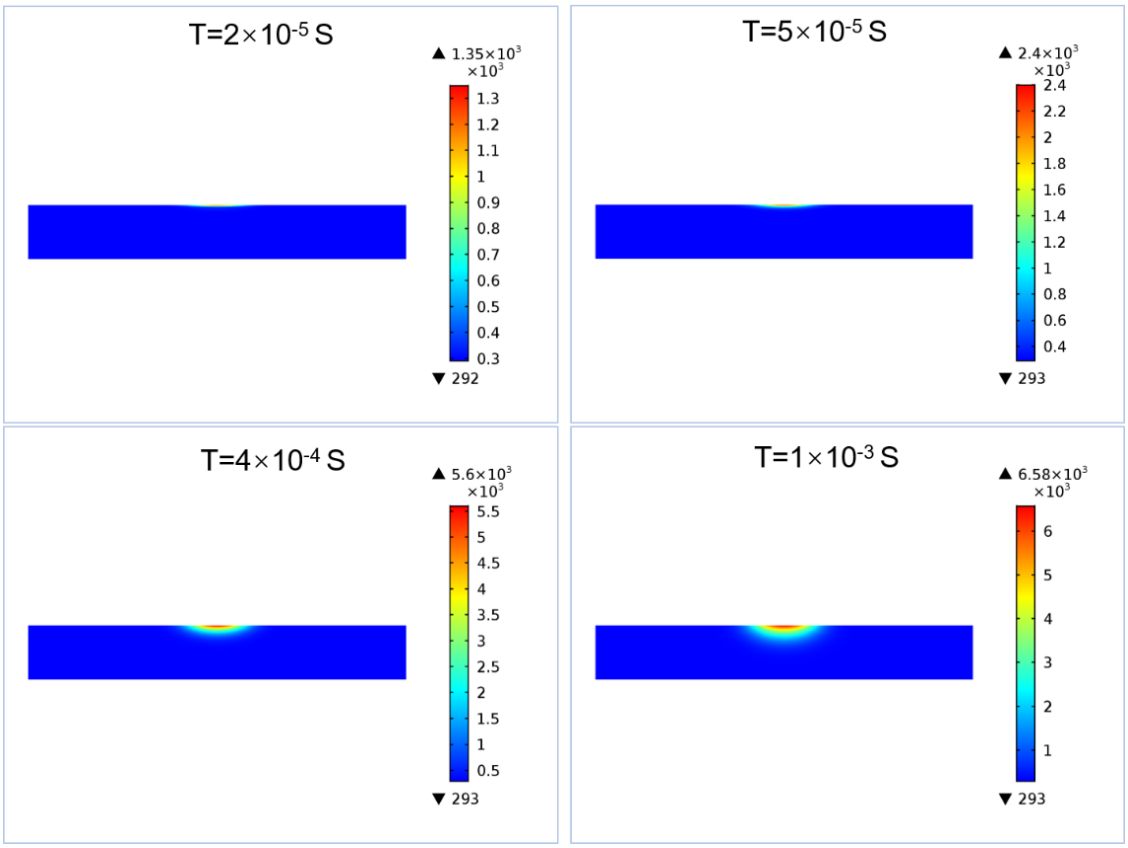

Figure S4.3: cross-section view of a Mo-gelatin sample illustrating the vertical temperature profile with different time scale based on the heat transfer simulation results.

Reference

1. S. T. Oyama, in *The chemistry of transition metal carbides and nitrides*, Springer, 1996, pp. 1-27.
2. M. Naguib, J. Come, B. Dyatkin, V. Presser, P. L. Taberna, P. Simon, M. W. Barsoum and Y. Gogotsi, *Electrochemistry Communications*, 2012, **16**, 61-64.
3. M. Ghidiu, M. R. Lukatskaya, M. Q. Zhao, Y. Gogotsi and M. W. Barsoum, *Nature*, 2014, **516**, 78-U171.
4. M. Khazaei, M. Arai, T. Sasaki, C. Y. Chung, N. S. Venkataramanan, M. Estili, Y. Sakka and Y. Kawazoe, *Advanced Functional Materials*, 2013, **23**, 2185-2192.
5. M. Naguib, O. Mashtalir, J. Carle, V. Presser, J. Lu, L. Hultman, Y. Gogotsi and M. W. Barsoum, *Acs Nano*, 2012, **6**, 1322-1331.
6. O. Mashtalir, M. Naguib, V. N. Mochalin, Y. Dall'Agnese, M. Heon, M. W. Barsoum and Y. Gogotsi, *Nature Communications*, 2013, **4**.
7. P. Eklund, M. Beckers, U. Jansson, H. Högberg and L. Hultman, *Thin Solid Films*, 2010, **518**, 1851-1878.
8. A. S. Ingason, M. Dahlqvist and J. Rosen, *J Phys-Condens Mat*, 2016, **28**.
9. Y. Gogotsi, *Nat Mater*, 2015, **14**, 1079-1080.
10. C. Xu, L. Wang, Z. Liu, L. Chen, J. Guo, N. Kang, X.-L. Ma, H.-M. Cheng and W. Ren, *Nat Mater*, 2015, **14**, 1135-1141.

11. R. S. Kappes, F. Schonfeld, C. Li, A. A. Golriz, M. Nagel, T. Lippert, H. J. Butt and J. S. Gutmann, *Springerplus*, 2014, **3**.
12. L. E. R. O'Leary, J. A. Fallas, E. L. Bakota, M. K. Kang and J. D. Hartgerink, *Nat Chem*, 2011, **3**, 821-828.
13. S. S. Harilal, J. R. Freeman, P. K. Diwakar and A. Hassanein, *Springer Ser Opt Sci*, 2014, **182**, 143-166.
14. S. B. Ogale, P. P. Patil, D. M. Phase, Y. V. Bhandarkar, S. K. Kulkarni, S. Kulkarni, S. V. Ghaisas and S. M. Kanetkar, *Phys Rev B*, 1987, **36**, 8237-8250.
15. J. Bello, H. R. Bello and J. R. Vinograd, *Biochimica et Biophysica Acta*, 1962, **57**, 222-229.
16. A. Royon, Y. Petit, G. Papon, M. Richardson and L. Canioni, *Opt Mater Express*, 2011, **1**, 866-882.
17. M. R. Lukatskaya, O. Mashtalir, C. E. Ren, Y. Dall'Agnese, P. Rozier, P. L. Taberna, M. Naguib, P. Simon, M. W. Barsoum and Y. Gogotsi, *Science*, 2013, **341**, 1502-1505.
18. J. Lin, Z. W. Peng, Y. Y. Liu, F. Ruiz-Zepeda, R. Q. Ye, E. L. G. Samuel, M. J. Yacaman, B. I. Yakobson and J. M. Tour, *Nature Communications*, 2014, **5**.

5 Chapter: Foldable Paper Electronics by Direct-Write Laser Patterning

Keywords: Foldable paper electronics; laser; molybdenum carbides; electret generator; paper supercapacitor.

5.1 Abstract

In this chapter, non-conductive papers are converted to patterned conductors by using an IR or UV laser without burning the paper into ashes. Gelatin mediated Mo ion ink is applied to the paper as the sources, which are then converted to highly conductive Molybdenum carbide (Mo_3C_2) and graphene paper (MG-paper) as conductive electrode under the laser patterning process. This process generates nanoscale pores due to the high local temperature and the conductive flakes can be transferred to other substrates for possible pressure and gas sensor applications. The conductivity of converted electrodes shows less than 30% decay after 800 cycles of bending tests. Several devices have been demonstrated successfully, including direct patterned electret generators, van-shape foldable generators, and interdigitated supercapacitors with foldable structures assembled by the Origami mechanisms for three-dimensional electronic circuits.

5.2 Introduction

In the past decade, great amount of attentions have focused on clean energy and clean techniques. Recyclability and disposability become essential considerations for materials and devices[1]. Wasted paper have been demonstrated in making disposable electronics to inspire works in the area of paper electronics[2]. Paper-based energy generators[3, 4], energy storage devices including batteries[5, 6] and supercapacitors[7-9], sensors and actuators[10, 11], low cost diagnosis devices[12] and microfluidics systems[13] have all been investigated. These works have been based on the additional depositions of functional materials on paper such as wax printing[14], evaporation, and lithography process to change the properties of non-conductive papers. Previously, the possibility of converting wasted papers to graphene has also been reported with the additional evaporation of Ag as the contract pads for good conductivity together with a high temperature annealing process. A new scheme is proposed and demonstrated here by rinsing paper in a non-conductive polymer solution with embedded metal ions and selectively converting them to conductive materials by direct-write laser patterning under the ambient environment as shown in **Figure 5.1**.

Figure 5.1 illustrates the fabrication process. Paper is first rinsed with Mo^{5+} ions/polymer ink, in which the ions are trapped on the polymer network of hydrogel. As-prepared sample is then scanned by a laser beam with different power and different scanning rates. The ions are converted to Molybdenum carbide on papers with arbitrary design patterns using the assist of computer-aided design tools. Modified process parameters can produce the high conductivity of about 20 ohm/square, and resilience to the folding deformation for more than 800 cycles. Micro-meter resolution also enables the capability of direct fabrication of active devices on paper, including piezo-electret generators, supercapacitors and on-paper electrochemical detectors. Furthermore,

the foldable nature of paper can construct deformable origami structures[15] and assemble the different components with higher element density by using 3-dimensional designs[16]. As an example, several generators can be folded as a van structure to provide 4 times higher current (80 μA) and voltage (100 V) outputs. Despite the comprehensive assembly process, two on-paper supercapacitors are folded in parallel from a single piece of paper to increase the energy storage capability. In addition, a pulse wave sensor, heavy metal ion detector and gas sensor are demonstrated using laser-patterned electrodes on paper.

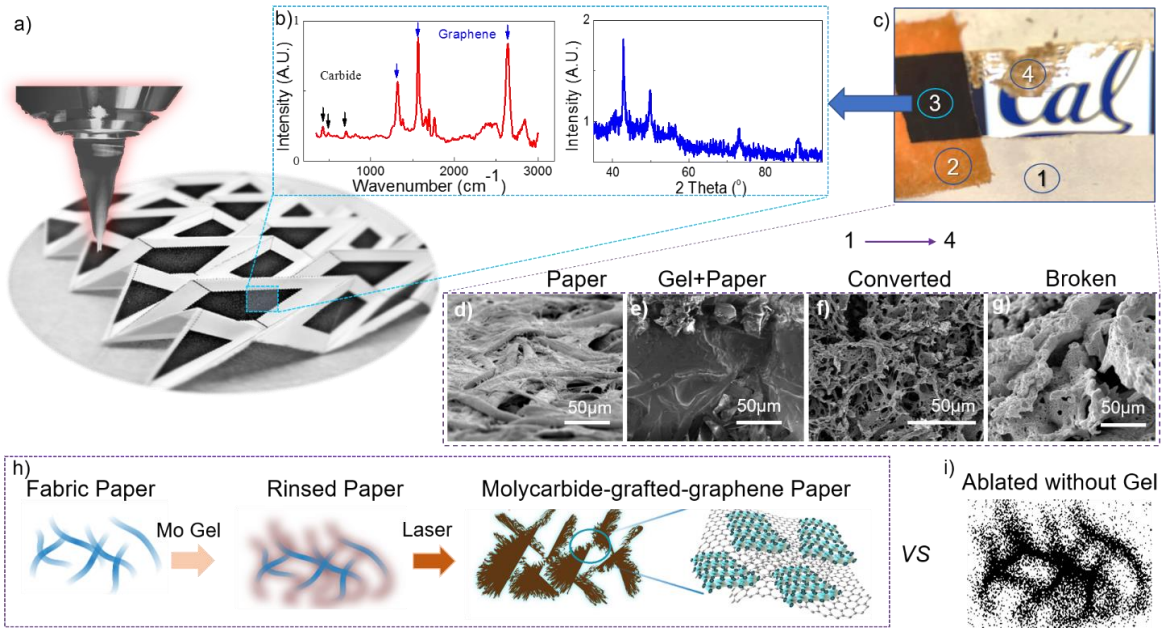

Figure 5.1 (a) Illustration of a prototype origami structure made by the laser direct conductive electrodes on a non-conductive paper substrate. (b) Raman and XRD of laser patterned paper with a coating of Mo-gel, as shown in area #3 in (c). (c) Optical image of different areas of a paper, area #1 as pristine paper, area #2 as Mo-gel rinsed paper, area #3 as laser converted paper and area #4 as laser ablated paper without Mo-gel. (d-g) SEM images of the areas in (c), respectively, showing micro structures of untreated and treated papers. (h) The illustration of microscopic fabric structures in paper filled with Mo-gelatin gel and converted to porous structures composed of Mo_3C_2 and graphene. (i) Pristine paper without the Mo-gelatin gel coating is burnt into ashes and broken into non-connected structures.

5.3 Results and Discussion

5.3.1 Characterization

Different types of common papers have been tested as the substrates. The resistance of samples on different paper is calculated using the current-voltage (IV) curve by a 2-probe source meter (Keithley 2400). The measured sheet resistances of conductors made from different paper substrates are shown in **Figure 5.2a** and the SEM pictures of different papers after rinsing with the Mo-gel inks and after laser ablation are shown in **Figure 5.3**. Six types of papers are tested in our experiments, including filter paper, two kinds of nonwoven paper, paper towel, A4 paper (85g) and scientific wiper. The filter paper has the best conductivity with a sheet resistance of 45.3Ω/sq

due to its good water absorption capability, large thickness and good mechanical strength to keep the Mo-gel ink during laser patterning process. In comparison, scientific wiper also absorbs ink well but it is thin with low mechanical strength such that the samples can be easy destructed under the laser ablation. Considering both the conductivity and mechanical strength, unless otherwise specified, we used A4 paper as the substrate in the following experiments.

To optimize our direct-write laser patterning process, the recipe of the custom-made Mo-gel ink and the parameters of the laser engrave process are investigated. The results of sheet resistance are shown in **Figure 5.2b**. Gelatin-based ink gives the lowest sheet resistance (51.3 Ω/sq), or best conductivity. On the other hand, PEO (15.8 MΩ/sq) and PVP (7.56 MΩ/sq) both result in high sheet resistance. The sheet resistance of different Mo ion concentration is tested in **Figure 5.2c** and the inset is the corresponding optical image of samples after the laser engraving process. We can see an obvious tendency between the Mo ion concentration and sheet resistance. With the increasing of Mo ion concentration from 0.5 M to 1 M, the sheet resistance reduces by about 50%. When the Mo^+ concentration increases, the sheet resistance decreases and saturated at around 3 M. The color of samples after the laser ablation process also gives an intuitive indication of the conductivity. The original ink with Mo ion is brown and the processed paper after the conversion process is black. The sheet resistance of using different laser power and scanning rate is shown in **Figures 5.2d** and **5.2e**. The combination of laser power and scanning rate in the fabrication process decides the energy applied in each 'spot'. On the one hand, if laser power is high or the scanning rate is low, the substrate paper is prone to be burnt. If the laser power is low or the scanning rate is high, the input energy on the ink is not enough to convert the Mo ions to molybdenum carbide. Considering the laser power and the scanning rate as a whole and the efficiency of this fabrication process is proportional to the scanning rate, we choose 2W and 250 mm/s as the process parameters in this chapter. Furthermore, unless otherwise specified, we used gelatin as the polymer and 2.5M Mo ion as the ink. To demonstrate the stability of our direct-write electronics, the folding test is conducted and the sheet resistance during the 800 times folding tests is shown in **Figure 5.2f** and the conductivity decreases about less than 20% after 800 times folding in our tests. **Figure 5.3** are SEM images of paper at different regimes, with and without the Mo-Gel solution, and after the laser conversion process. The zoomed in SEM image of the converted paper area clearly shows vary porous structure and the TEM image of converted paper area shows nanoscale particles. **Figure 5.4a** shows IV curves of conductors made on different paper substrates and converted from Mo-gel with a concentration of 2M/L and using a 2W laser running at a 250mm/s scanning rate. The IV curve of an A4 paper converted from the Mo-gel solution with different concentrations is shown in **Figure 5.4b** by using laser with power of 2W and scanning rate of 250 mm/s. **Figure 5.4c** shows IV curves of converted electrodes on an A4 paper after repeated bending cycles of 800 cycles.

Figure 5.5 shows the electron dispersion spectrum of MG-paper converted from different polymer gel and paper rinsed in the 3M Mo-gel shows the highest Mo concentration while paper rinsed in the 2.5M Mo gel shows the highest concentration of carbon. The high concentration of carbon in MG-paper converted rinsed in 2.5M Mo gel could help to explain its high conductivity. Higher Mo concentration will increase the IR absorption and for the conversion to Mo_3C_2 in MG-paper which increase conductivity when the Mo concentration is relatively low, under 2M in this study. However, fabric paper and gelatin scaffold is also partially converted to multiple layers of graphene with even higher conductivity, such that higher concentration of Mo ions absorb IR more effectively and decrease the component of carbon. Higher concentration solutions are not studied

due to the solubility limit of $MoCl_5$ in DI water. **Figure 5.6** shows SEM images of MG-paper converted from different types of paper, with different fabrication parameters.

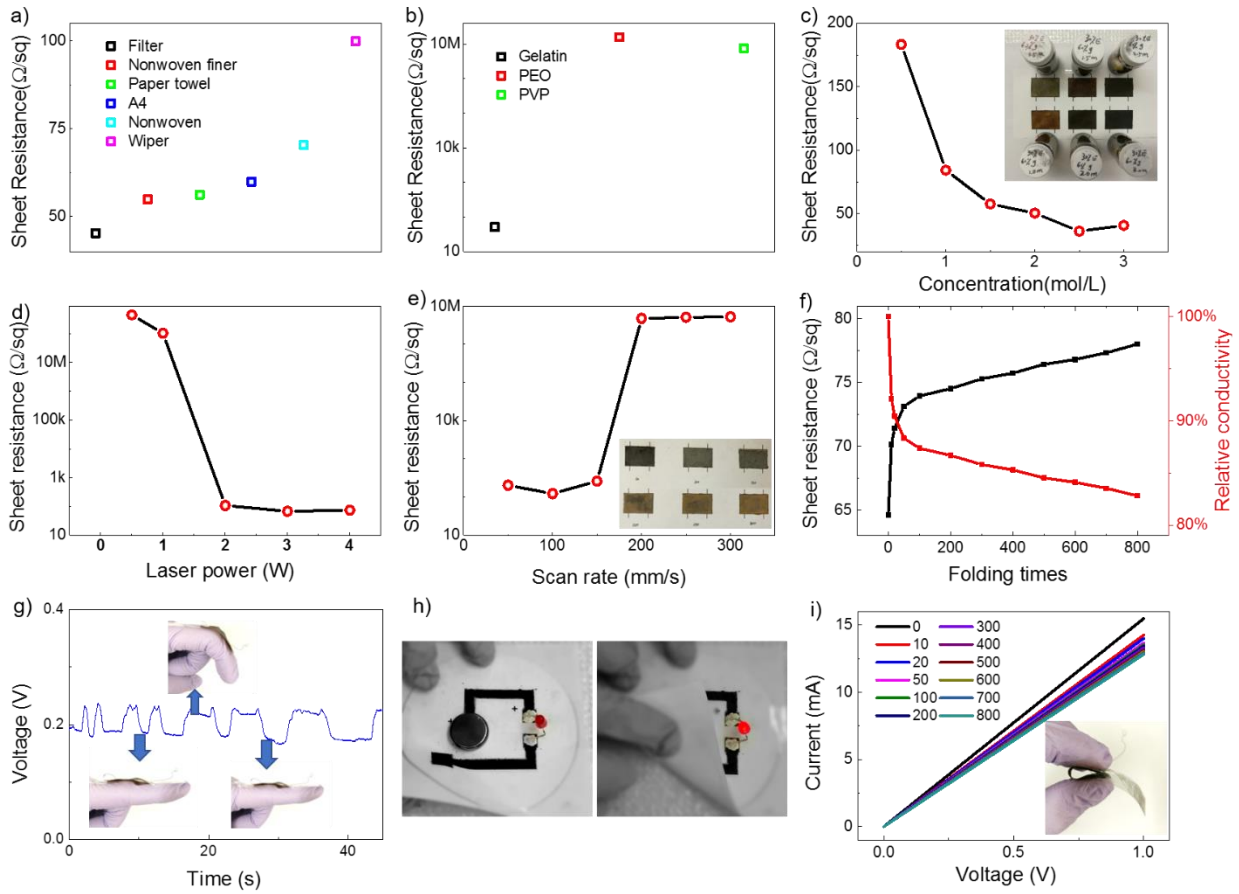

Figure 5.2 Sheet resistance of samples after the laser ablation process: (a) different types of paper (2W, 250mm/s, 2mol/L Mo 60% gelatin 30% ethanol); (b) with solutions with different polymers (A4 paper, 2W, 250mm/s, 2mol/L Mo 30% ethanol); (c) with different concentration of Mo ions (A4 paper, 2W, 250mm/s, 60% gelatin 30% ethanol); (d) under different laser powers (A4 paper, 250mm/s, 2mol/L Mo 60% gelatin 30% ethanol); (e) different laser scanning rates (A4 paper, 2W, 2mol/L Mo 60% gelatin 30% ethanol) and (f) after folding for different cycles (A4 paper, 2W, 250mm/s, 2mol/L Mo 60% gelatin 30% ethanol). (g) Resistivity changes in the bending-recovery process. (h) Simple example of folding laser write patterns to a functional circuit. (i) IV curve of laser converted MG-paper showing conductivity is resilient to the folding operations.

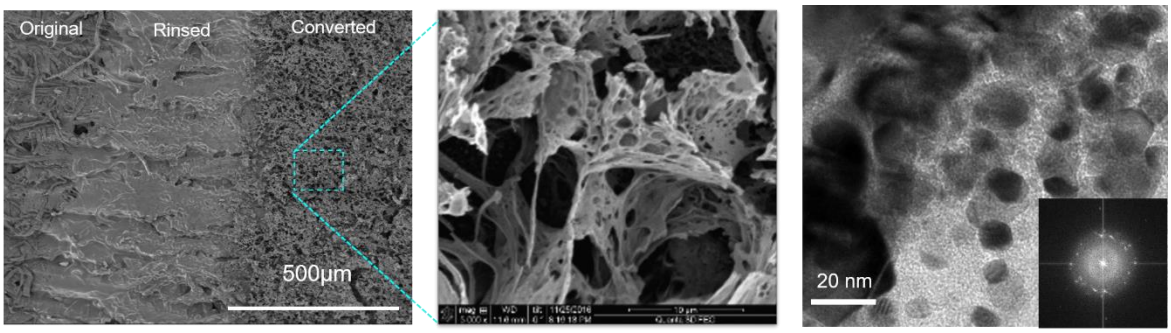

Figure 5.3(**Left**) SEM image of paper at different regimes. (**Middle**) Zoomed in SEM image of the converted paper area. (**Right**) TEM images of converted paper area showing nanoscale carbide particles.

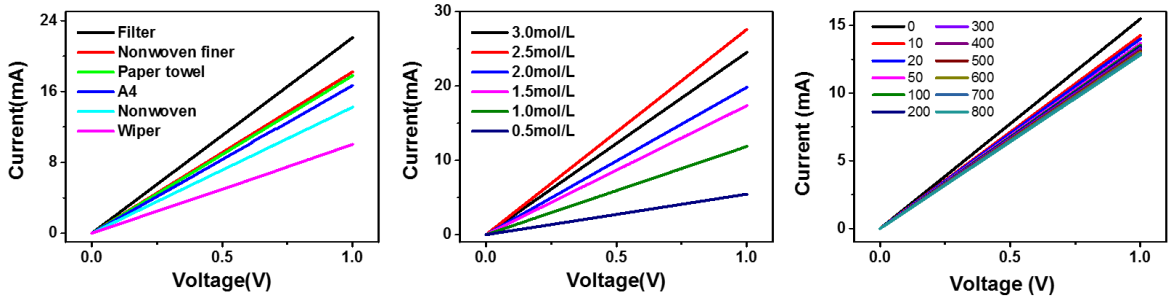

Figure 5.4 (**Left**) IV curves of different paper converted from Mo-gel with a concentration of 2M/L and using a 2W laser running at a 250mm/s scanning rate. (**Middle**) IV curve of an A4 paper converted from the Mo-gel solution with different concentrations by using laser with power of 2W and scanning rate of 250 mm/s. (**Right**) IV curve of converted electrodes on an A4 paper after repeated bending cycles of 800 cycles.

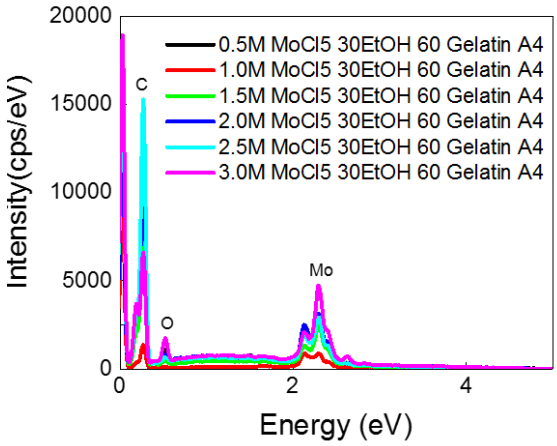

Figure 5.5 Electron dispersion spectrum of MG-paper converted from different polymer gel. MG-paper from 3M Mo-gel shows the highest Mo concentration while paper rinsed in 2.5M Mo gel shows highest concentration of carbon.

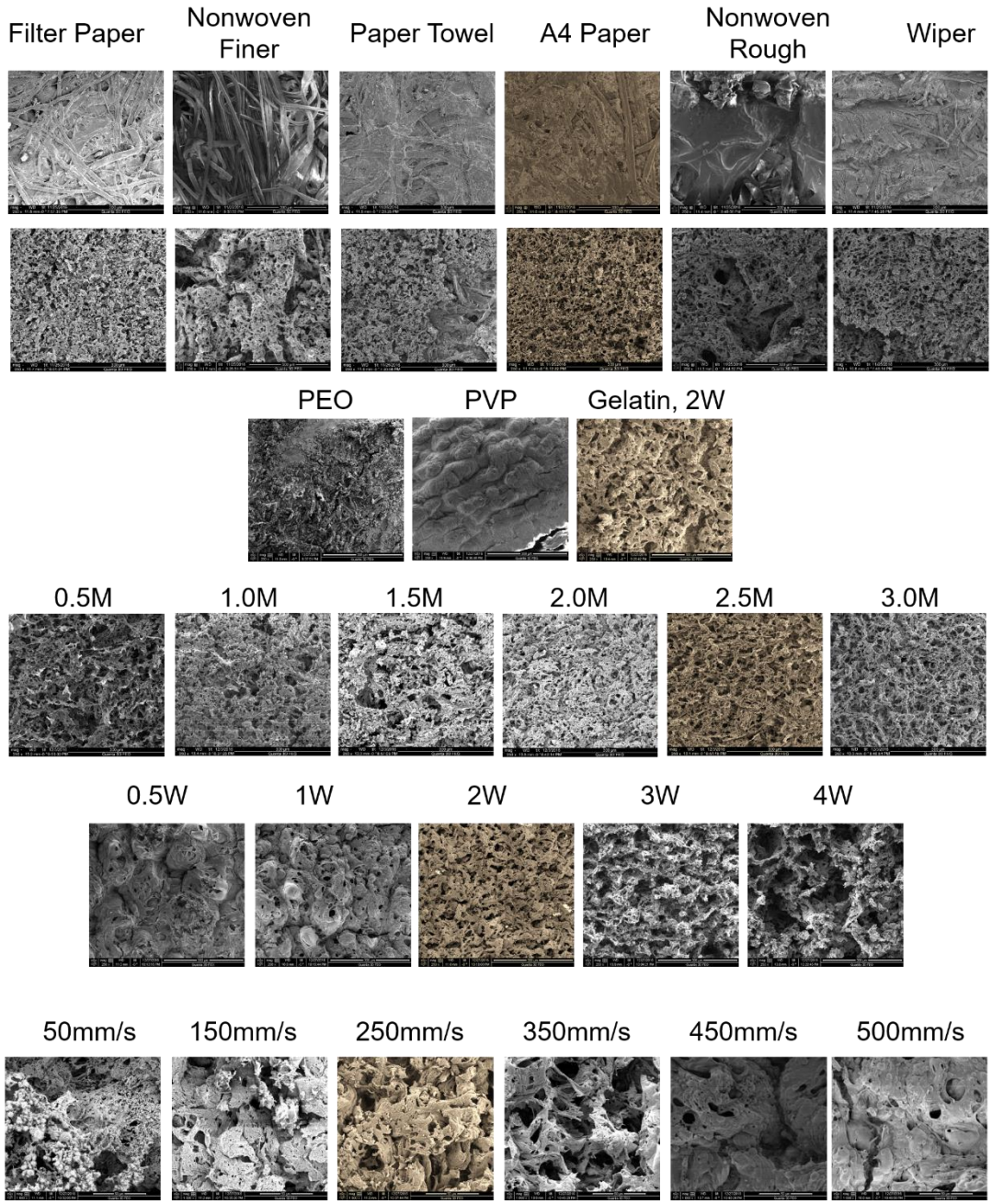

Figure 5.6 SEM images of MG-paper converted from different types of paper, with different fabrication parameters. (**First Row**) SEM images of six different types of paper rinsed in polymer ink and after converted to conductors. (**Third Row**) SEM images of A4 paper ablated by the IR laser which have been rinsed in the Mo-gel solutions with PVP, PEO and gelatin as the media. (**Fourth Row**) MG-paper converted from A4 paper rinsed by gelatin mediated gel with different concentration of molybdenum ions. (**Fifth Row**) MG-paper converted from A4 paper treated with different laser power. (**Sixth Row**) MG-paper converted from A4 paper treated with 2W laser power at different scanning speeds.

5.3.2 Applications

Paper Based Triboelectric Generators

A piezo-electret generator with direct-write laser patterned electrodes is demonstrated. The structure and working mechanism of such generator is shown in **Figure 5.7a**. The sandwich-like generator consists of three layers. The upper and middle layers are electrodes made of paper-based molybdenum carbide. The middle layer is polytetrafluoroethylene (PTFE) film, working as the electret material that can keep net charges. The PTFE film can be charged either by corona charging or a tissue wiping process and it will hold negative charges. The three layers form two capacitors in series. The capacitance and quantity of electric charge of the upper and lower capacitor can be calculated according to Equations (1) and (2). In equilibrium, the upper and lower electrodes are at the same potential, namely two capacitors have the same voltage. When we press on the generator, the distance between the PTFE film and the upper electrode is changed, which changes the capacitance of the upper capacitor. Since the entire charging quantity on PTFE can be seen as a constant, the relative distribution of charging on upper and lower electrodes will change as shown in Equation (3). Thus the charge will move from one electrode to the other. During the process of pressing, the distance of the PTFE and upper electrode is decreased and the upper electrode will attract more positive charge. Thus positive charge moves from the lower electrode to the upper one, which causes a positive current from lower electrode to the upper one in the external circuit. This current will be generated until a new equilibrium of charge distribution between the two electrodes is achieved. In the releasing process, the current flows in the opposite direction. The distance of the PTFE and upper electrode is increased and the upper electrode will release some positive charge. Thus positive charge moves from the upper electrode to the lower one, which causes a positive current from upper electrode to the lower in the external circuit. Shown in **Figure 5.7b** is such a generator with a 2cm×2cm electrode to power eight LEDs in series. The generated current through LED is measured and shown in **Figure 7c**. Since LEDs are diodes, the generated AC current is chopped to DC current. The open-circuit current of such paper-based generator is shown in **Figure 5.7d**, which is an AC signal. The positive signal corresponds to the pressing, which is rapid and sharp. The negative part corresponds to the releasing process, which is relative slow and gentle. Applying a rectifier on the generator, we can measure the rectified short-circuit current, shown in **Figure 5.7e**. The rectified current in one cycle along with its integral on time domain shows the quantity of transferred charge in the pressing and releasing process. With the rectifier, the entire transferred charge in one cycle is the sum of these two parts. The voltage of charging a commercial 4.7μF capacitor using the above generator with rectifier is shown in **Figure 5.7f**. It takes less than 60s to charge the 4.7μF capacitor to 2V. The zoomed in figure shows detailed charging voltage in one cycle. The step-wise charging is due to the pressing and releasing process. **Figure 5.7g** shows the open-circuit voltage of fan structured generator (four in parallel) and **Figure 5.7h** shows the short-circuit current of fan structured generator (four in parallel).

$$C = \frac{\varepsilon A}{d} \qquad (1)$$

$$Q = CV \qquad (2)$$

$$Q_{PTFE} = Q_{upper} + Q_{lower} \qquad (3)$$

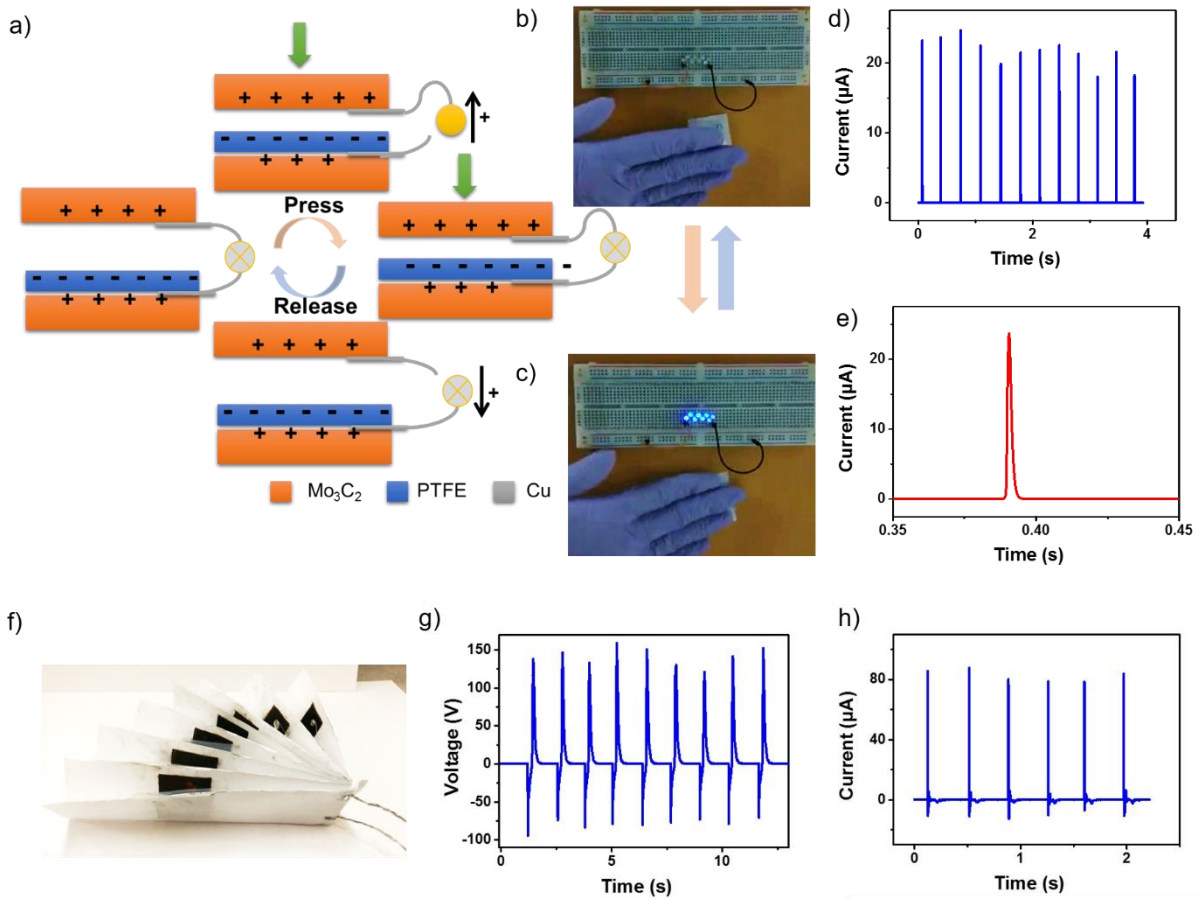

Figure 5.7 (a) Structure and working mechanism of paper-based electret generator. (b,c) Paper-based electret generator powering eight LEDs. (d) Rectified current of generator powering eight LEDs in series and is zoomed in to show the current in one cycle (e). (f) Fan structure generator (g) Open-circuit voltage of fan structured generator (four in parallel) (h) Short-circuit current of fan structured generator (four in parallel).

Figure 5.8a shows the short-circuit current measurement results of a paper-based electret generator, including the rectified short-circuit current in **Figure 5.8b**; charging voltage results of a 4.7μF capacitor using one 2 ×2 cm^2 paper-based electret generator in **Figure 5.8c**; measured current in the generator in **Figure 5.8d**; measured rectified current and charge stored in the capacitor in **Figure 5.8e**; and enlarged results to show the voltage and charge in one cycle in **Figure 5.8f**.

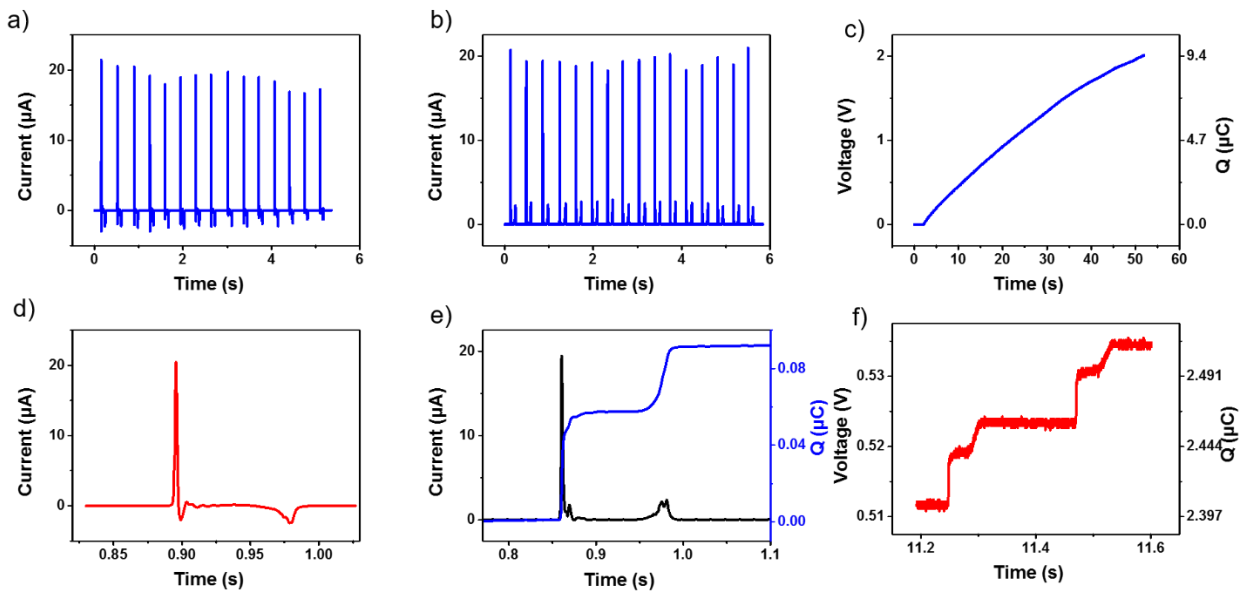

Figure 5.8 (a) Short-circuit current of a paper-based electret generator. (b) Rectified short-circuit current of paper-based electret generator. (c) Charging voltage of a 4.7μF capacitor using one 2 ×2 cm^2 paper-based electret generator. (d) Measured current in the generator. (e) Measured rectified current and charge stored in the capacitor. (f) Enlarged results to show the voltage and charge in one cycle.

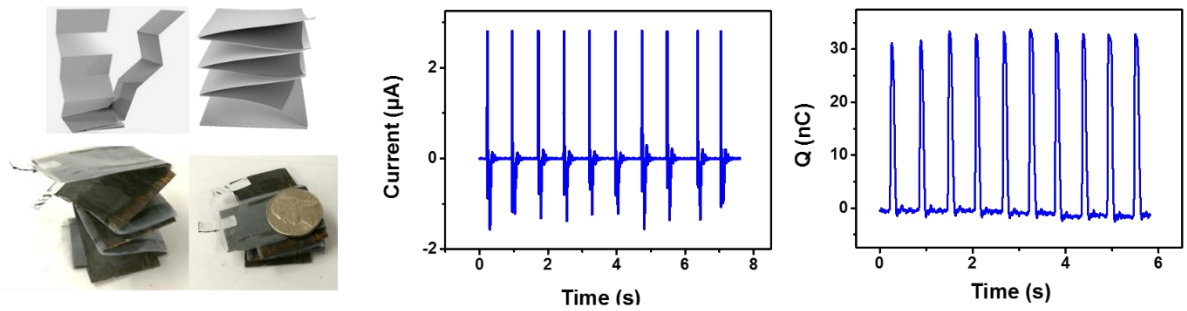

Figure 5.9 A double side converted and folded paper triboelectret generator. (Left) Schematic and optical image of a double side converted MG-paper. (Middle) Short circuit current of a double side converted and folded generator. (Right) Charges generated in different cycles.

Inspired by the structure of origami fan and accordion, we construct a fan structure generator, which has several generators connected in parallel. A single piezo-electret generator can generate high output voltages. By connecting several generators in parallel, one can achieve multiple times of output currents as shown in **Figure 5.7h**, where four generators in parallel can generate 80μA of output current or four times of a single generator output (**Figure 5.7d**). On the other hand, **Figure 5.9** shows a double-side converted and folded paper triboelectric-electret generator. The left side figure is the schematic and optical image; and the middle figure is the measured short circuit current; and the right side figure shows the measured charges generated in different cycles.

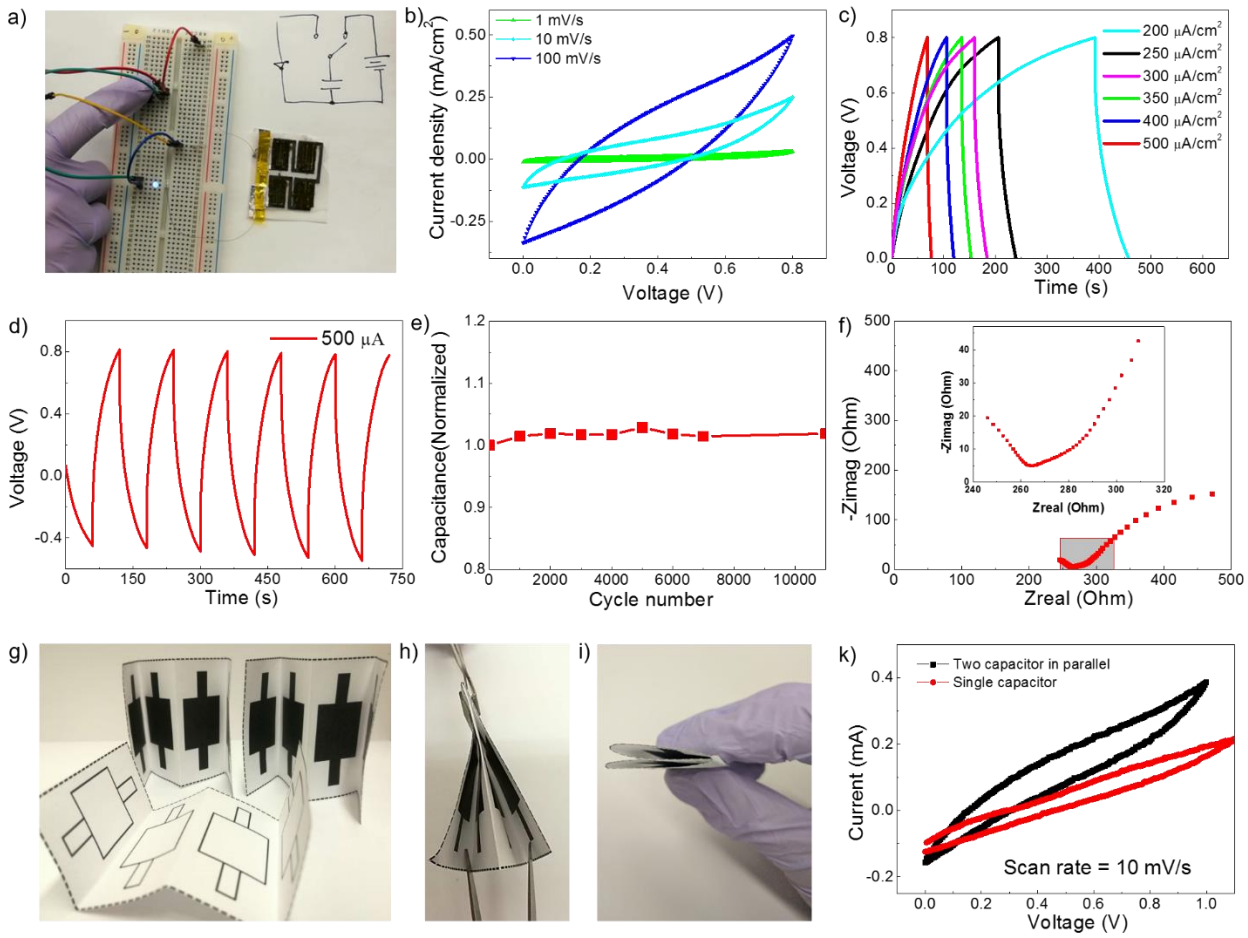

Figure 5.10 (a) A paper-based interdigitated supercapacitor powering up a purple LED. (b) The comparison between the CVs of paper-based interdigitated supercapacitor under different voltage scanning rate. (c) The charge/discharge curves under different current density. (d) Galvanostatic charge/discharge curve with a constant current of 500 μA/cm^2. (e) The long cycling test results of a paper-based supercapacitor for 11000 cycles. (f) Nyquist plots for a paper-based supercapacitor. (g-i) Demonstration of a parallel capacitator by folding the paper electrodes. (k) Comparison of a single capacitor and parallel capacitor at scan rate of 10 mV/s.

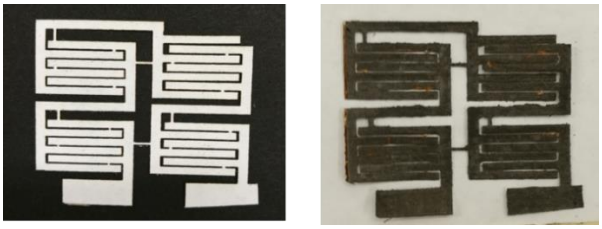

Figure 5.11 Optical images of a paper-based interdigitated supercapacitor before and after the conversion to conducted MG-paper.

The supercapacitor devices are fabricated based on the laser conversion process. The prototype device in **Figure 5.10a** is fabricated as follows: the interdigital capacitor pattern on paper is rinsed with 2.5 mol/L Mo+, 60% wt gelatin and 30% ethanol solutions; the as-prepared patterns are processed with infrared laser; and the patterned area is covered with a layer of high concentration (20m) Li+ salt and 5% PVA as the electrolyte. **Figures 5.10b~f** show the performance of the paper based supercapacitor with the two-electrode capacitor configuration. The charge/discharge, cyclic voltammetry (CV), and the electrochemical impedance spectroscopy (EIS) tests are characterized by using the Gamry workstation.

Figure 5.10a shows four as-fabricated interdigitated supercapacitors are connected in series and the output voltage can reach 3V (each supercapacitor can produce about 0.8 Volt) to power up a purple LED. **Figure 5.10b** shows the cyclic voltammetry of a paper-based supercapacitor with various scan rate from 1 to 100 mV/s. The specific capacitances calculated are 14.01 mF/cm^2, 9.53 mF/cm^2 and 2.43 mF/cm^2 from the CV curves with scan rate of 1, 10 and 100 mV/s, respectively. A rectangular CV curve indicates low internal resistance and the tested device has CV curves close to rectangular even with a high scan rate of 50 mV/s. There are some distortions and oblique tendency under high voltage regions (0.8 V) and high scan rate cases (100 mV/s), which might be attributed to the presence of water splitting. **Figure 5.10e** shows paper-based supercapacitor could maintain its capacitance without no visible decay after 11000 cycles with slight increase in specific capacitance probably due to the intercalations of electrolyte.

In **Figure 5.10c**, the charge/discharge curves with different charging/discharging current density from 200 to 500 $\mu A/cm^2$ are presented. The galvanostatic cycling of supercapacitor electrodes is performed at a constant current density of 500 $\mu A/cm^2$ as show in **Figure 5.10d**. The charge/discharge curves are almost linear in the voltage range (-0.4 V ~ 0.8 V), showing excellent capacitive property. In **Figure 5.10f**, the Nyquist diagram is presented with a straight line in the low-frequency regime and a slight arc in the high-frequency regime. This indicates the device is like a pure capacitor as the larger the slope in the low frequency regime, the better the capacitive behavior. The magnitude of equivalent series resistance (ESR) is indicated by the lowest point in the Nyquist plot as 270 Ω, which determines the charge/discharge rate of the capacitor and is also an important factor that influence the power density.

Other demonstrations are also exhibited as below (**Figure 5.12**), including a electrochemical sensor for heavy metal ions such as Cu^{2+}; resistivity based gas sensor; piezoelectret based pulse wave sensor. In this paper, we develop a direct pattern method to fabricate foldable electronic devices on paper by CO_2 laser. By employing a kind of Mo-gelatin hydrogel, paper fabrics convert to hierarchical porous structure made of metal carbide-graphene-paper skeleton, rather than burnt into ashes with the same power density on pristine untreated paper. This method proves to be versatile on a series of different type of paper, among which filter paper provide the lowest sheet resistance while A4 paper provide similar conductivity but with better feasibility in printing process. Piezoelectret based generator is demonstrated with two electrodes made from the MG-paper, using PTFE as the source of AC current. Taking the most important merit of paper which is the flexibility and foldability, a parallel generator integrated fan structure is designed with higher out-put current. Besides the energy harvesting generator, foldable supercapacitor is also demonstrated by folding the pattern electrodes to parallel supercapacitor. Many other applications are also demonstrated hunting for novelty, including electrochemical cell for heavy metal detection, gas sensor based, and a pulse wave sensor. This method brings a metal free electrodes fabrication solution, which could further broaden the practical application for foldable paper electronics.

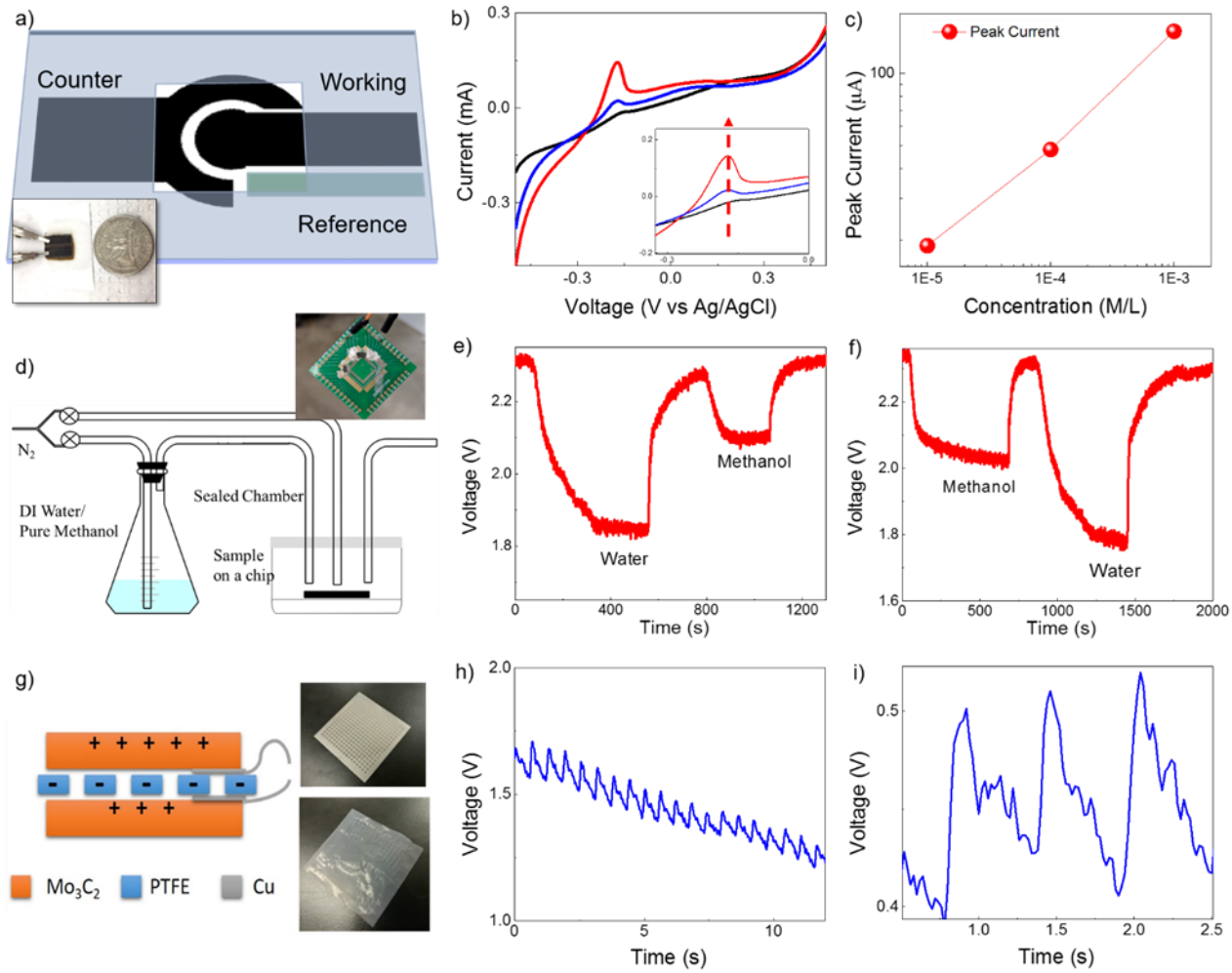

Figure 5.12 Other foldable electronic application based on the MG-paper. (a-c) heavy metal ion detection. (d-f) gas sensor (g-i) pulse wave sensor.

5.4 Experimental Session:

Mo-gelatin gel preparation: $MoCl_5$ (95 wt%, Sigma Aldrich) is dissolved in DI water, with different molar concentration: 1m, 1.5m, 2 m, 2.5m and 3m with 60 wt% gelatin (powder, from porcine skin, type A, Sigma Aldrich) heated to 60 ºC to make homodispersed hydrogel.

Laser direct converted different type of paper electrodes: filter paper, two kinds of nonwoven paper, paper towel, A4 paper (85g) and scientific wiper are rinsed with Mo-gelatin hydrogel on pre-patterned area. Rinsed paper is patterned by CO_2 laser with different power varying from 0.5W to 4.0 W, with scan speed from 50mm/s to 300 mm/s.

Characterization of MG-paper: As patterned electrodes are tailored to 2cm×1cm size to measure their sheet resistance (Keithley 2400). Scanning electron miscopy (SEM, Quanta FEI) is used to characterize the structure of fabric paper and ablated paper with hieratical porous structures. X-ray diffraction (XRD, Bruker 8) and energy dispersive spectroscopy are employed to verify the component and composition of laser ablated paper.

Application demonstrations of MG-paper based electronics:

As-patterned MG-paper is directly used as a conductor on paper, which enables circuit to work after folding. Secondly, such paper electrode is assembled with a piece of pre-charged polytetrafluoroethylene (PTFE) thin film to make a piezoelectret generator. Four pads with area of 2×2 cm^2 are patterned on one piece of paper, which is assembled and connected with different wire connection to make supercapacitors in parallel or in series. Electrolyte made of PVA-LiTFSI (10% 20m) are deposit onto the electrodes before the assembly as separators also. Three electrodes system on paper is made of two prepatterned carbide electrodes and one Ag/AgCl electrode besides, which is tested in 0.5M H_2SO_4 media with different concentration of Cu^{2+}. Electret generator is applied as pulse wave sensor based on its voltage signal change. As patterned carbide paper with hierarchical porous structure is also import into a gas sensing system, which is sensitive to polarized molecules such as moisture and methanol.

Reference

1. Y. H. Jung, T. H. Chang, H. L. Zhang, C. H. Yao, Q. F. Zheng, V. W. Yang, H. Y. Mi, M. Kim, S. J. Cho, D. W. Park, H. Jiang, J. Lee, Y. J. Qiu, W. D. Zhou, Z. Y. Cai, S. Q. Gong and Z. Q. Ma, *Nat Commun*, 2015, **6**.
2. A. Russo, B. Y. Ahn, J. J. Adams, E. B. Duoss, J. T. Bernhard and J. A. Lewis, *Adv Mater*, 2011, **23**, 3426-+.
3. Z. L. Wang, *Acs Nano*, 2013, **7**, 9533-9557.
4. Z. L. Wang, *Mater Today*, 2017, **20**, 74-82.
5. T. H. Nguyen, A. Fraiwan and S. Choi, *Biosensors & Bioelectronics*, 2014, **54**, 640-649.
6. Q. C. Liu, L. Li, J. J. Xu, Z. W. Chang, D. Xu, Y. B. Yin, X. Y. Yang, T. Liu, Y. S. Jiang, J. M. Yan and X. B. Zhang, *Adv Mater*, 2015, **27**, 8095-8101.
7. L. Nyholm, G. Nystrom, A. Mihranyan and M. Stromme, *Adv Mater*, 2011, **23**, 3751-3769.
8. V. L. Pushparaj, M. M. Shaijumon, A. Kumar, S. Murugesan, L. Ci, R. Vajtai, R. J. Linhardt, O. Nalamasu and P. M. Ajayan, *Proceedings of the National Academy of Sciences of the United States of America*, 2007, **104**, 13574-13577.
9. D. W. Wang, F. Li, J. P. Zhao, W. C. Ren, Z. G. Chen, J. Tan, Z. S. Wu, I. Gentle, G. Q. Lu and H. M. Cheng, *Acs Nano*, 2009, **3**, 1745-1752.
10. X. Y. Liu, M. Mwangi, X. J. Li, M. O'Brien and G. M. Whitesides, *Lab on a Chip*, 2011, **11**, 2189-2196.
11. Q. Z. Zhong, J. W. Zhong, B. Hu, Q. Y. Hu, J. Zhou and Z. L. Wang, *Energy & Environmental Science*, 2013, **6**, 1779-1784.
12. A. A. Kumar, J. W. Hennek, B. S. Smith, S. Kumar, P. Beattie, S. Jain, J. P. Rolland, T. P. Stossel, C. Chunda-Liyoka and G. M. Whitesides, *Angew Chem Int Edit*, 2015, **54**, 5835-5852.
13. A. W. Martinez, S. T. Phillips, G. M. Whitesides and E. Carrilho, *Analytical Chemistry*, 2010, **82**, 3-10.
14. E. Carrilho, A. W. Martinez and G. M. Whitesides, *Analytical Chemistry*, 2009, **81**, 7091-7095.
15. P. K. Yang, Z. H. Lin, K. C. Pradel, L. Lin, X. H. Li, X. N. Wen, J. H. He and Z. L. Wang, *Acs Nano*, 2015, **9**, 901-907.
16. S. Felton, M. Tolley, E. Demaine, D. Rus and R. Wood, *Science*, 2014, **345**, 644-646.

6 Chapter: Surfactant assisted large-scale synthesis of MoS_2

Keywords: MoS_2; Self-assembly; 2D materials; surfactant; photoluminescence

6.1 Abstract

A solution-based method is developed to synthesize large scale MoS_2, one key transition metal dichalcogenide (TMDC), by spin-coating pre-assembled metal ions (MoO_4^{2-}) and gelatin solutions on versatile substrates with the assistance of a cationic surfactant. After annealing in sulfur vapor at 300 ºC, the film is converted to MoS_2. By controlling the surfactant and metal ion concentration, the domain size of MoS_2 can be adjusted. Both AFM and SEM characterizations show the morphologies of multi-layer MoS_2 structures, while the optical photoluminescence (PL) tests show monolayer MoS_2 characteristics. Both A exciton at ~1.8eV and B exciton at ~2.0eV imply potential direct band transition, while the energy levels are slightly blue shifted by ~10mV as compared with monolayer MoS_2. The GIWAX scattering tests illustrate well defined stacking of the fabricated film in the z direction, while the in-plane orientation is observed as random. These phenomena imply the potential weak interlayer coupling of the fabricated film as the layer-by-layer assembled gelatin scaffold with the assistance of the surfactant is in favor of the plenary assembly to expand the interlayer distance and weaken the interlayer coupling

6.2 Introduction

Growing single crystal materials has long been a challenging problem to material scientists, which generally requires strict control of growth conditions. The state-of-art methods to grow single crystal structures include the Czochralski process, Bridgman–Stockbarger, hydrothermal synthesis and Sublimation. All of which are performed at high temperature with high pressure or other extreme conditions.[1, 2] Our group has been developing low temperature simple method to synthesis single crystal metal film inspired by Marangoni effect, in which gelation scaffold complex with metal ions are self-assembled to ultra-flat thin films. At the same time, single crystallinity is most desirable for semiconductor materials to eliminate scattering and losses from grain boundaries in the carrier transportation process and promote the device performances such as field effect transistors.

Transition metal di-chalcogenides have been very popular 2D materials in recent years with direct bandgaps when they are scaled down to mono layers. Great efforts have been put into synthesis techniques for large scale uniform layer TMDCs, including chemical vapor deposition, annealing from solution, ALD and etc.[3] MoS_2 as one of the TMDC family member has been widely studied for its unique properties of valley polarization, selective photoluminescence and high carrier mobility in broad range applications in valleytroncis, photonics and electronic devices. Even though MoS_2 has been used as a lubricant since the middle of last century, methods to synthesis controllable and a few layers of MoS_2 are still in the development. Common methods include chemical vapor deposition (CVD),[4] mechanical exfoliation, and hydrothermal method. CVD grown MoS_2 suffers a large number of sulfur vacancy impurities and the latter two methods generally result in polycrystalline MoS_2 with high amount of defects. CVD process also requires high temperature of more than 600 ºC to activate the reaction of precursor sulfur and MoO_3.

At present, wafer-scale synthesis of MoS_2 can only be processed with the highly sophisticated and expensive metal organic chemical vapor deposition (MOCVD) to produce polycrystalline structures with small domains.[5] Here, we demonstrate the synthesis of large scale 2D crystals of MoS_2 by mixing Molybdenum salt in gelatin for the initial formation of thin films and the thermal annealing process in sulfur environment with a low temperature around 300 ^{o}C, as shown in **Figure** 1. By controlling the concertation and spin-coating speed, we can control the thickness of the MoS_2 films and the Raman spectra characterizations indicate these are multilayer MoS_2. A post burning process is performed to remove the residual gelatin and carbon in open air after the sulfurization process.

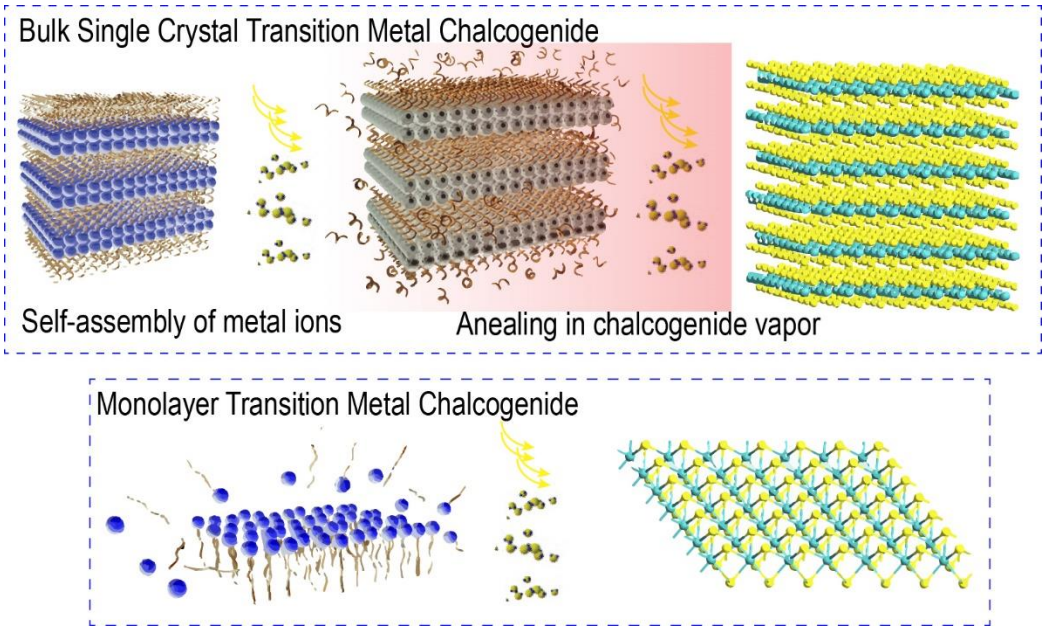

Figure 6.1 The schematic diagram for the large-scale synthesis of MoS_2 by the self-assembly of gelatin scaffold. (Top) Metal ions embedded in the layer-by-layer self-assembled gelatin scaffold structure. (Bottom) Assembly of monolayer gelatin with embedded Mo ions. The gelatin scaffolds with Mo ions are converted to transition metal chalcogenide by annealing in a sulfur vapor process.

6.3 Results and Discussion

The accumulation of the hydrogel with embedded Mo ions at the air/liquid interface is the result of the convection-capillary and recirculation flow generated by the Buoyancy-Marangoni effect upon heating.[6, 7] Self-assembly and ordering of the hydrogel can form large area membranes to function as scaffolds and the conversion of embedded Mo ions to atoms occurs under the elevated temperature. The gelatin scaffolds constrain the crystallization process to grow into two-dimensional layers and the annealing process further assists the formation of MoS_2 and the decomposition of gelatin. Among different concertation of Mo and gelatin, we observe that concentration of 2M Mo with 10 wt% gelatin in DI water provide the most uniform and continuous film as shown in **Figure 6.2a**. High concentration of gelatin will increase the thickness and residual gelatin which can induce cracks on the assembled films, while low concentration gelatin can result in the "free Mo" atoms in the forms of particles between layers. One drop of 100µl

solution results in ~2μm thick single crystalline film on a 1×1 cm^2 silicon oxide surface. The film is then peeled off the substrate and transferred onto a scotch tape or a copper grid for microdiffraction XRD or TEM tests, respectively. **Figure 6.2b** shows the cross section view of the film on a broken sample to reveal the layer-by-layer stacking nature of the structure. The HRTEM (**Figure 6.2d-f**) results show the in-plane diffraction pattern of MoS_2 with a lattice distance of 0.27 nm (100). Synchrotron radiation characterizations in **Figure 6.2 (h-j**) shows the beamline penetrates the sample and resolves sharp Laue patterns asthe sample is single crystal without misfit of diffractions. We transfer the sample onto a scotch tape to avoid background noises from silicon wafer, and the scan area is 20μm×20μm with a step of 1μm. The 400 Laue diffraction patterns are merged to resolve the zone axe as all in the (002) direction. Each sampling spot shows single crystal Laue pattern. Comparing to the plane orientation, a maxim of 9.77 degree is resolved. The small misalignment of the crystal plane is mostly likely induced by the detachment of MoS_2 film from the scotch tape during the transfer process.

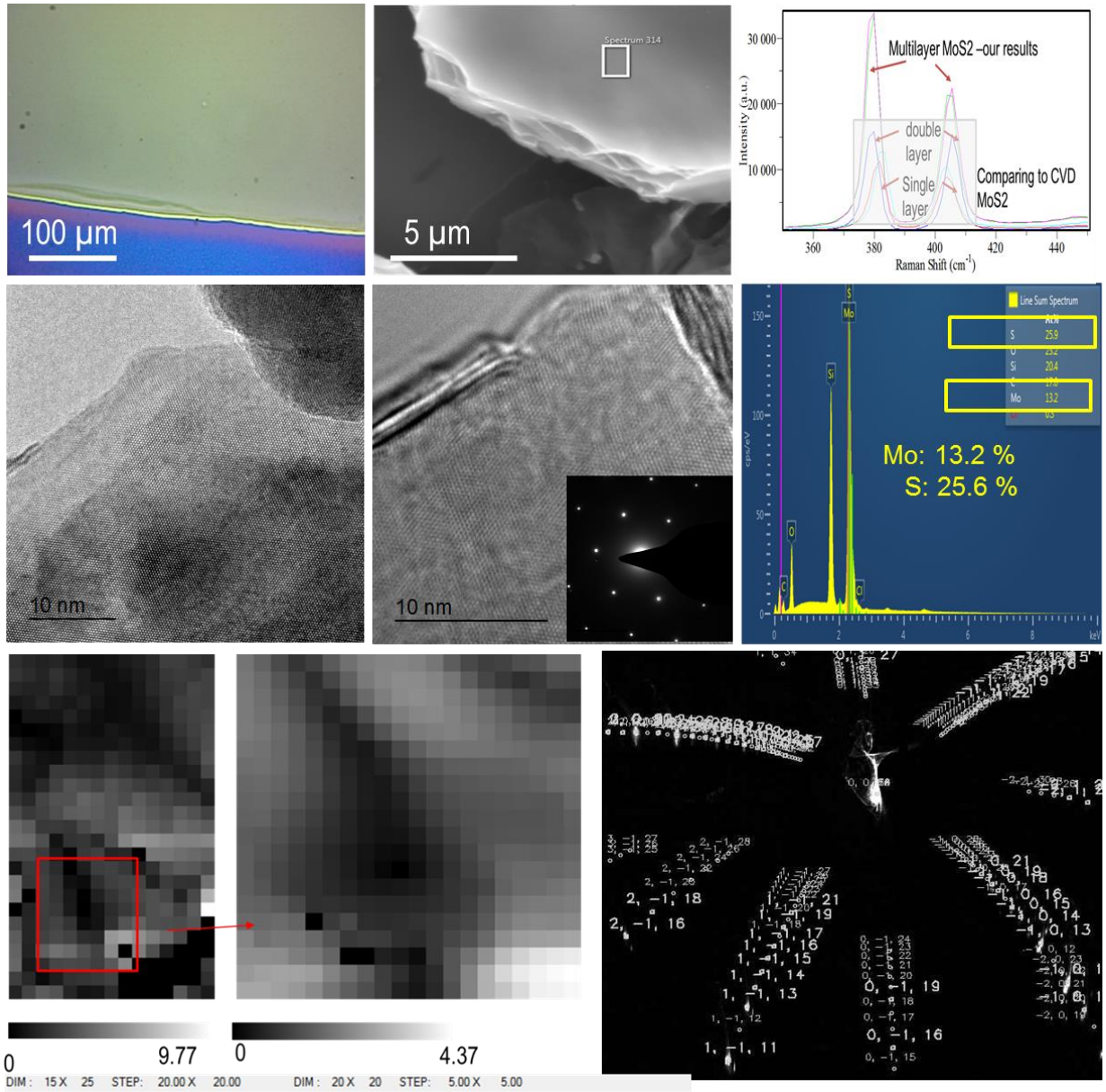

Figure 6.2 (a) Optical image of as synthesized single crystalline large scale MoS_2 thin film with a thickness of about 2 □m. (b) SEM image of a broken sample to show the cross-section view revealing layer-by-layer 2D structures. (c) Raman spectra of a single crystal MoS_2 thin film together with those from monolayer/double layers of MoS_2 grown by the CVD process. (d) TEM image of an exposed edge area of the crystal MoS_2, showing the 2D staking structure and the honey-comb atomic structure of MoS_2. (e) Monolayer MoS_2 area in (d) and the diffraction pattern. (f) EDS of single crystal MoS_2 sample, showing an atomic mole ratio 1:2 (Mo:S). (h,i,j) Micro-diffraction beamline 12.3.2 from the Advanced Light Source (ALS) at Lawrence Berkeley National laboratory with aligned zone-axis implying single crystalline structure.

The nature of single crystalline MoS_2 is verified by the Raman spectrum. The intensities of inner layer vibration E_{2g}^1 peak at ~ 380 cm^{-1} and inter-layer vibration A_{1g} peak at ~ 405 cm^{-1} are higher than those of single layer and double layer MoS_2 (**Figure 6.2c**), while the distance between E_{2g}^1

and A_{1g} enlarge over the peak distance in mono and double layer MoS_2. On the other hand, direct band gap and interlayer photon transmission could only exist in monolayer MoS_2. In order to decrease the layer number, highly diluted solution is prepared with the assistance of surfactant. Thiosalt ammonium molybdate with much lower solubility in water is mediated in SDBS media (0.1% wt) with gelatin (0.1% wt) by spin coating at a rate of 6000 rpm.[7] After the fabrication process, optical image shows sub-millimeter scale triangle structures and radial growth patterns with well-defined edges in the AFM mapping results. The thickness of these structures is about 10-20nm and this result is very different than the results from traditional CVD process where thick MoS_2 film generally aggregate to form particles. The center of these structure is much higher than the other part as the possible starting point for the layer-by-layer nucleation process. The thermal annealing process help sulfur to diffuse down to the bottom layer to grow MoS_2.

The process to make multi-layered MoS_2 brings a solution-based interfacial assembly process to the synthesis of MoS_2 and provides inspiration for low temperature synthesis of single crystalline semiconductors.[8, 9] By systematically controlling the ion concentration and hydrogel concentration, the optimal condition to effectively grow multi-layered MoS_2 single-crystalline films with uniform morphology and topology can be established. The low temperature process to make high quality single crystalline MoS_2 is promising for large scale fabrication of other chalcogenide based single crystal films for electronics[10], optoelectronics and other applications on a broad range of substrates including flexible structures.

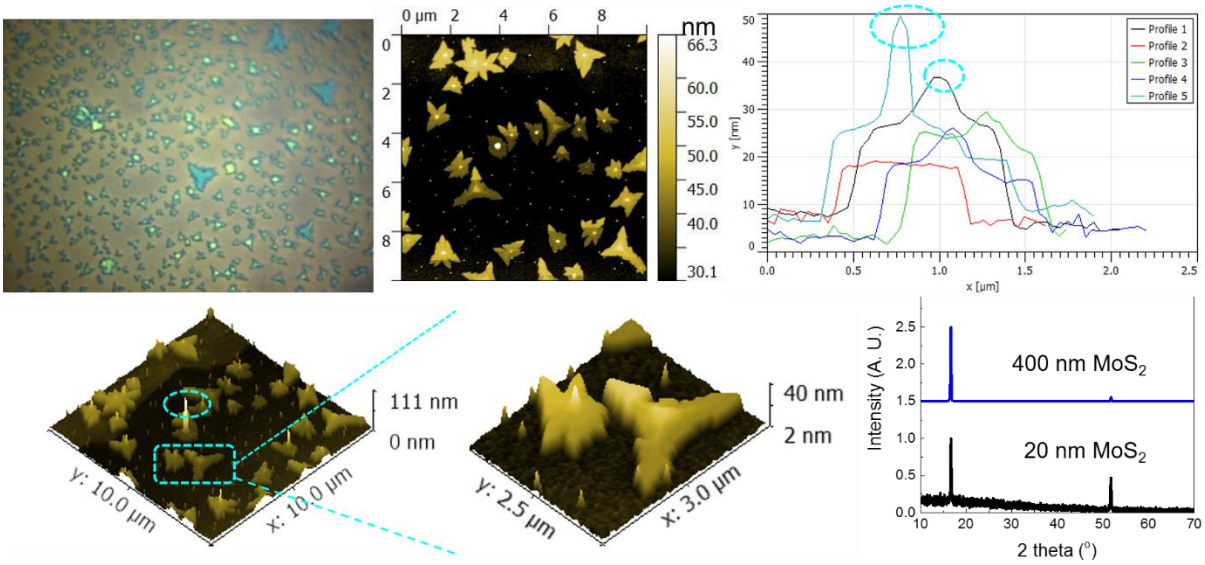

Figure 6.3 (a) An optical image of a few layer MoS_2 grown from diluted thiosalt of Mo. (b)AFM scanning of the sample surface. (c,d,e) Surface profile of different domain in (b), showing average 15 nm in thickness for MoS_2. On those domain, the central area is higher than the rest of the structure implying a nucleation core. (f) XRD results on the film of a few layer MoS_2.

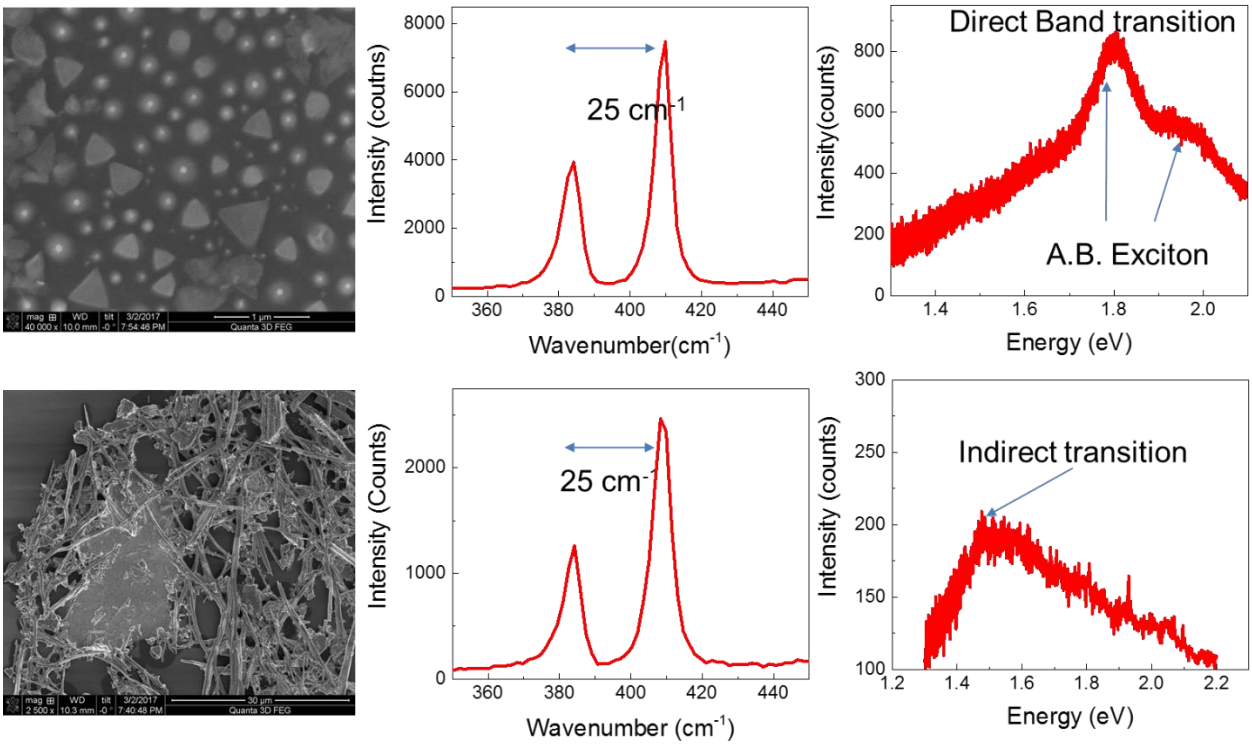

Figure 6.4 Raman and photoluminescence results of synthesized MoS_2 with flat-shape structures (**top**) or nanowire-shape (**bottom**). The control parameter is the concentration of solutions. From the Raman peaks distance, these structures have multiple layers, while the photoluminescence results imply the flat-shape structure has direct band transition.

As shown in **Figure 6.3**, lower concentration gelatin-Mo results in thinner MoS_2 film, highly diluted MoO_4^{2-} ions with the assist of cationic surfactant could grow into flat shape multiple layer MoS_2 which shows direct band transition photoluminescence (**Figure 6.4**). Hight concentration surfactant solution over the critical micelle point will results in cylinder shape assembled MoS_2 wires, which show more obvious indirect band transition at ~1.3 eV. Grazing mode incident small angle x-ray diffraction observe the stacking in z direction and poor orientation in the x-y plane (**Figure 6.5**). Such results could imply a random interlayer alignment which greatly weaken the predicted interlayer interaction, and the surfactant residual could possibly isolate and protect each layer MoS_2 resulting monolayer-like optical properties.

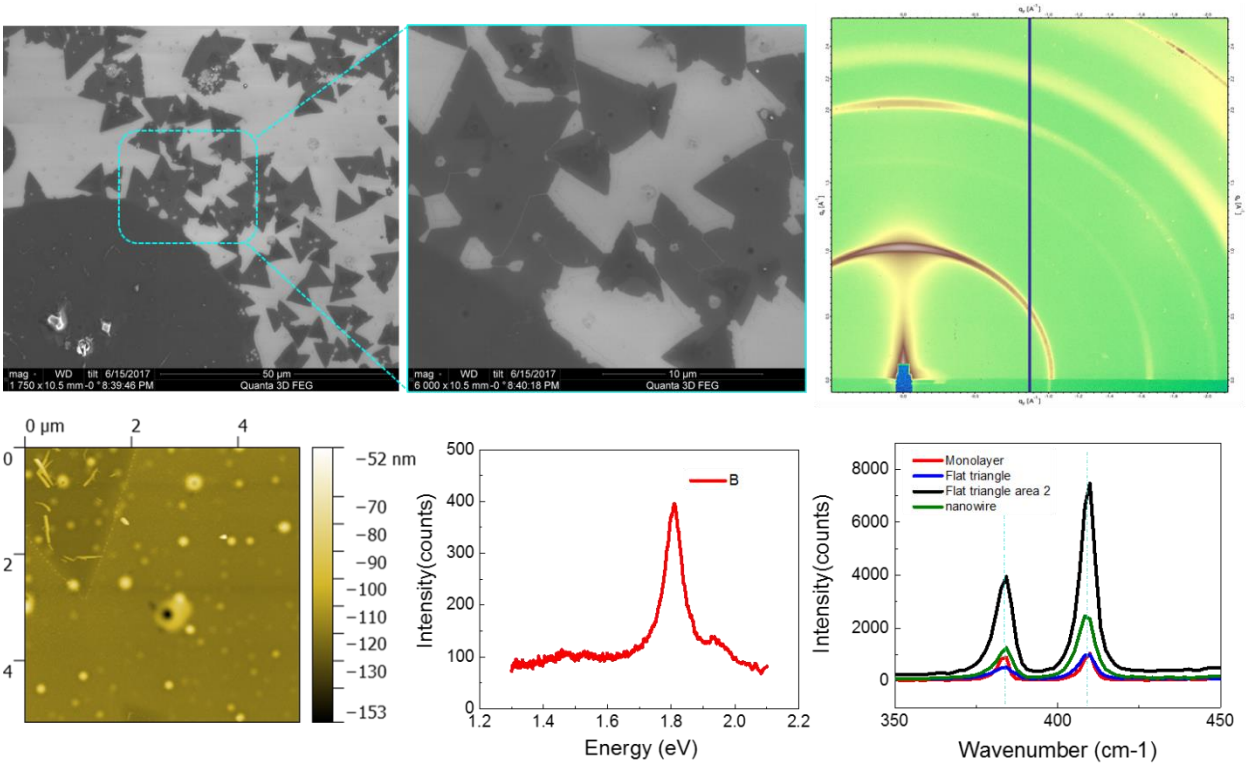

Figure 6.5 Stacking layers of MoS_2. (a) and (b) SEM of MoS_2 layers (c) GIWAX diffraction of (a,b), showing strong inter plane with 001 orientation, with weak inner plane crystallinity. (d) AFM of one piece of the triangle shape MoS_2. (e) Direct photon transition observed on the stacking layer of MoS_2. (f) Raman spectroscopy of multilayer MoS_2.

6.4 Experimental Sessions:

<u>Mo^{5+} -gelatin template preparation:</u> Molybdenum pentachloride (>99.9% wt purity, Sigma Aldrich) is dissolve in DI water to make 2M/L concentration solution. Gelatin (porcine skin, Sigma Aldrich) is dissolve in $MoCl_5$ to make 1%, 5% 10% and 20% wt solutions. The Mo-gelatin solution is spin coated onto silicon with 300 nm silicon oxide at a speed of 3000 rpm for the synthesis of MoS_2. Ammonium molybdate (95% wt, Sigma Aldrich) and surfactant sodium dodecyl benzene sulfonate (SDBS, Sigma Aldrich) are employed to dilute the solution down to 0.1% and 0.1M for with the spin-coating rate increased to 6000 rpm to reduce the number of layers for MoS_2.

<u>MoS_2 conversion and removal of template:</u> Sulfur annealing is performed at 300 ºC in a Thermal Lab 1 zone furnace and the distance between sulfur powder and substrates is 5 cm. The temperature ramping up time takes 15 mins, and the samples are kept at 300 ºC for 30 mins with N_2 or Ar flowing as protective carrier gas under a flow rate of 30 sccm. KOH solution is used to wash the waste gas at the end of flow system. After the furnace is cool down to room temperature, samples are transferred onto a hot plate at 300 ºC for 1 hour to remove the residual gelatin.

<u>Characterization and analysis:</u> Optical microscopy (OM, Keyence 600), Scanning electron microscopy (SEM, FEI Quanta 3D), Transmission electron microscopy (TEM, FEI Tecnai) are employed to study the morphology and structure of as-grown and transferred MoS_2. X-ray diffraction (XRD, Bruker D8), single crystal XRD (ALS, micro-diffraction beamline 12.3.2) are

employed to study the crystallinity of MoS_2. Raman spectrum (Renishaw inVia) and atomic force miscopy (AFM) are used to observe the stacking layers MoS_2.

Reference

1. Wagner, R. S.; Ellis, W. C. *Appl Phys Lett* **1964,** 4, (5), 89-&.

2. Sinno, T.; Dornberger, E.; von Ammon, W.; Brown, R. A.; Dupret, F. *Mat Sci Eng R* **2000,** 28, (5-6), 149-198.

3. Sun, Z.; Liao, T.; Dou, Y.; Hwang, S. M.; Park, M.-S.; Jiang, L.; Kim, J. H.; Dou, S. X. *Nature Communications* **2014,** 5, 3813.

4. Shi, Y. M.; Li, H. N.; Li, L. J. *Chem Soc Rev* **2015,** 44, (9), 2744-2756.

5. Kang, K.; Xie, S.; Huang, L.; Han, Y.; Huang, P. Y.; Mak, K. F.; Kim, C.-J.; Muller, D.; Park, J. *Nature* **2015,** 520, (7549), 656-660.

6. Li, Y. F.; Yoda, M. *Int J Heat Mass Tran* **2016,** 102, 369-380.

7. Uricanu, V. I.; Duits, M. H. G.; Filip, D.; Nelissen, R. M. F.; Agterof, W. G. M. *J Colloid Interf Sci* **2006,** 298, (2), 920-934.

8. Zhou, Y. B.; Deng, B.; Zhou, Y.; Ren, X. B.; Yin, J. B.; Jin, C. H.; Liu, Z. F.; Peng, H. L. *Nano Lett* **2016,** 16, (3), 2103-2107.

9. Zolyomi, V.; Drummond, N. D.; Fal'ko, V. I. *Phys Rev B* **2013,** 87, (19).

10. Lu, Z.; Lee, O.; Wong, J. C.; Salahuddin, S. *J Mater Res* **2016**, 31, (7), 911-916.

7 Chapter: Conclusion

7.1 Summary of Current Research

This work demonstrates a few different approaches for the synthesis and assembly of two-dimensional materials: (1) liquid droplet-based CVD process to grow monolayer graphene; (2) ALD/sulfurization hybrid process to produce TiS_2 coated vertical-aligned carbon nanotube electrodes; (3) CO_2 laser ablation for 2D metal carbide structures of ~10nm thickness; and (4) surfactant-assisted self-assembly process for the synthesis of few layer MoS_2. Based on these new routines, different applications with proper materials design are developed for high performances.

In chapter 2, we have demonstrated the synthesis of single layer graphene on nickel droplets using the CVD process. Reduced droplet size (~1 μm) decreases the carbon absorption amounts and makes possible the as-grown graphene to be single layer. Graphene can outgrow over the boundaries of nickel droplets, forming continuous graphene layer over discontinuous nickel droplets (using 75nm-thick nickel film). Such graphene flakes can be directly used in the demonstrated photo-sensing device without the time-consuming transfer process by responding to visible light with generated photocurrent up to ~0.53 $\mu A/mm^2 \cdot W$. We attribute this phenomenon to a photothermal effect, which is originating from graphene flakes. This has been verified by geometrically symmetric and asymmetric measurements in response to different temperature gradients. This work not only bring inspiration on self-limiting processes for the synthesis of 2D materials and the fabrication of devices bypassing the transfer process, but also investigate the photothermal effect induced by in situ hybridization instead of double gate tuning in previous published reports.

In chapter 3, we have designed a new TiS_2/CNT hybrid electrode made by a-two step ALD process. The synthesis process brings inspiration of direct synthesis for the conformal coating of 2D transition metal dichalcogenide onto versatile substrates and templates. TiS_2/CNT exhibits high capacitance of 195 F/g, 3V working voltage and 60.9 Wh/kg energy density, which outperforms other tested electrodes based on RuO_x/CNT, TiN/CNT and MoS_2/CNT configurations in all three parameters. High concentration LiTFSI salt and nanocrystalline TiS_2/CNT can result in more surface related capacitive behavior to achieve both the high capacitance and power density. Further studies may push the limit of high concentration electrolyte in different energy storage system including supercapacitors as well as utilize transition metal chalcogenides together with highly conductive carbon frames with high surface area such as 3D graphene sponges.

In chapter 4, we have developed a versatile approach for the synthesis of porous 3D metallic transition metal carbides (Mo, W, Co) made of "2D" nanoscale flakes by using an easily accessible CO_2 laser in ambient environment. Among the metal ions and polymer media tested in this work, Mo/W with gelatin produced the best results based on the homogeneity of the flake structure and the carbonization yields. The two major reasons for this were identified as: (a) effective absorption of laser energy, which is key in reaching the necessary high reaction temperatures; (b) the self-assembly of triple helix gelatin polymers

for the layer-by-layer ordering of metal ions. The laser-induced Mo_3C_2 is a conductive and refractory material with hierarchical porosity (from microscale to nanoscale). Mo_3C_2 interdigitated electrodes in conjunction with a Li-rich electrolyte are shown to work in a temperature range of -50 to 300 ^oC with no significant degradation. This work provides a general approach for a low cost and high yield synthesis process for transition metal carbides for applications in flexible electronics and energy storage systems.

In chapter 5, the laser conversion method is utilized to make carbide materials based on various papers. The filter paper is tested to have the lowest sheet resistance, while the A4 paper provides similar conductivity with better printing capabilities. Electronic components are demonstrated by using the laser printing technique. For example, Piezoelectret based generator is demonstrated with two paper electrodes and PTFE as the electret material in the middle. The flexibility and foldability of paper make possible a parallel energy generator with integrated fan structures connected in parallel for high current outputs. Foldable supercapacitor is also demonstrated by folding the patterned electrodes to make parallel supercapacitors. As such, this method could further broaden the practical application for foldable paper electronics.

In chapter 6, precursors are pre-assembled for the synthesis of layer-by-layer 2D MoS_2 by using surfactants to assist transition metal assembly. Different surfactants such as CTAB and gelatin with concentration below the critical micelle values are applied according to transition metal ions such as MoO^{4+} and Mo^{5+}. Such assembled 2D building blocks are converted to transition metal chalcogenide by annealing in sulfur vapor, which produces the few-layer structures with random stacking angles and weak interlayer coupling. The multiple-layer structure shows near direct band transition photoluminescence results with relatively strong intensity.

7.2 Future Directions

Two approaches are proved in this work to be effective in controling the 2D morphology and lattice structure: (1) taking the advantage of low growing speed with self-limiting kinetics such as atomic layer deposition by which materials can be deposited layer-by-layer; (2) to utilize precursors with specific structure and the self-assembly process to construct scaffolds layer-by-layer as the deposition templates and convert metal ions to 2D layered structures. Both approaches could be used to develop 2D materials and their hetero-junction structures, and even more difficult structure such as “Janus” chalcogenide or carbide.

MoS_2, especially with rich edge sites, shows exceptional electrochemical catalytic effects in hydrogen evolution reaction with the band structure matching with H^+/H_2O (charge separator). Some of the carbide materials, such as Mo_2C and WC are known as electrochemical catalyst due to its prestigious charge transfer ability in redox reactions (transfer promoter). Among them, Mo_2C has been showing Pt-like behavior in hydrogen evolution reaction (HER), oxygen evolution reaction (OER) and CO_2 reduction while the price is lower than Pt. With either the CO_2 laser ablation or surfactant mediated self-assembly process, chalcogenide and carbide with 2D structure could be coupled, not only to lower the binding energy but also improve the charge transfer path. Potentially, with hydride chalcogenide-carbide structure or binary/ternary carbide structure, novel metal-free and highly effective catalysis system could be build. Specifically, structures with two-

dimensional morphologies having high surface areas and rich exposed edge states may further improve the catalytic performances.

Transition metal chalcogenides are famous for their direct band transition within visible light range existing in the monolayer which is essential for optical and optoelectronics at the visible light range. A lot of efforts have been put in the exfoliation or control of the TMDC growth processes to fabricate monolayer structures. The PL behavior in our result based on the few-layer TMDC structures could be from the effect of isolation of each individual layer by weakening the interlayer coupling. On the other hand, the state-of-art photoluminescence techniques utilize mostly quantum dots such as CdSe, CdTe, or Se doped ZnO. The color spectrum of quantum dots is highly dependent on the particle size, which requires strict control for PL-quenching or color impurity in display applications. In addition, dispersing quantum dots in polymer may severely decrease their quantum efficiency and photoluminescence intensity. The photoluminescence of transition metal dichalcogenide is more tolerant in terms of their physical particle size and relies more by the intralayer dispersion and interlayer coupling. By using different concentration of precursors and metal ions (Mo^{5+}, Ti^{4+}, Bi^{3+}, Ga^{2+}, etc), onee could potentially broaden the PL spectra range for a wide-range of display applications.

Biography

1. G. E. Moore, Proceedings of the IEEE, 1998, 86, 82-85.
2. 2. M. Despont, J. Brugger, U. Drechsler, U. Durig, W. Haberle, M. Lutwyche, H. Rothuizen, R. Stutz, R. Widmer, G. Binnig, H. Rohrer and P. Vettiger, Sensor Actuat a-Phys, 2000, 80, 100-107.
3. T. Roy, M. Tosun, J. S. Kang, A. B. Sachid, S. B. Desai, M. Hettick, C. M. C. Hu and A. Javey, Acs Nano, 2014, 8, 6259-6264.
4. S. J. Tans, A. R. M. Verschueren and C. Dekker, Nature, 1998, 393, 49-52.
5. A. K. Geim and K. S. Novoselov, Nature Materials, 2007, 6, 183-191.
6. Z. H. Sun and H. X. Chang, Acs Nano, 2014, 8, 4133-4156.
7. A. Molle, J. Goldberger, M. Houssa, Y. Xu, S. C. Zhang and D. Akinwande, Nature Materials, 2017, 16, 163-169.
8. M. Naguib, V. N. Mochalin, M. W. Barsoum and Y. Gogotsi, Advanced Materials, 2014, 26, 992-1005.
9. M. Ghidiu, M. R. Lukatskaya, M. Q. Zhao, Y. Gogotsi and M. W. Barsoum, Nature, 2014, 516, 78-U171.
10. S. Das, J. A. Robinson, M. Dubey, H. Terrones and M. Terrones, in Annual Review of Materials Research, Vol 45, ed. D. R. Clarke, 2015, vol. 45, pp. 1-27.
11. K. Kang, S. Xie, L. Huang, Y. Han, P. Y. Huang, K. F. Mak, C.-J. Kim, D. Muller and J. Park, Nature, 2015, 520, 656-660.
12. G. Fiori, F. Bonaccorso, G. Iannaccone, T. Palacios, D. Neumaier, A. Seabaugh, S. K. Banerjee and L. Colombo, Nat Nanotechnol, 2014, 9, 768-779.
13. W. M. Hu, S. Y. Ren and J. D. Dow, Phys Rev B, 1981, 24, 6156-6157.
14. A. Kormányos, G. Burkard, M. Gmitra, J. Fabian, V. Zólyomi, N. D. Drummond and V. Fal'ko, 2d Mater, 2015, 2, 022001.
15. J. Xiao, M. Zhao, Y. Wang and X. Zhang, Journal, 2017, 0.
16. M. Chhowalla, H. S. Shin, G. Eda, L. J. Li, K. P. Loh and H. Zhang, Nat Chem, 2013, 5, 263-275.
17. X. N. Zang, Q. Zhou, J. Y. Chang, Y. M. Liu and L. W. Lin, Microelectron Eng, 2015, 132, 192-206.
18. T. Palacios, Nat Nanotechnol, 2011, 6, 464-465.
19. J. L. McChesney, A. Bostwick, T. Ohta, T. Seyller, K. Horn, J. Gonzalez and E. Rotenberg, Phys Rev Lett, 2010, 104.
20. H. Wang, L. L. Yu, Y. H. Lee, Y. M. Shi, A. Hsu, M. L. Chin, L. J. Li, M. Dubey, J. Kong and T. Palacios, Nano Lett, 2012, 12, 4674-4680.
21. S. B. Desai, S. R. Madhvapathy, A. B. Sachid, J. P. Llinas, Q. X. Wang, G. H. Ahn, G. Pitner, M. J. Kim, J. Bokor, C. M. Hu, H. S. P. Wong and A. Javey, Science, 2016, 354, 99-102.
22. G. A. Muller, J. B. Cook, H. S. Kim, S. H. Tolbert and B. Dunn, Nano Lett, 2015, 15, 1911-1917.
23. D. H. Deng, K. S. Novoselov, Q. Fu, N. F. Zheng, Z. Q. Tian and X. H. Bao, Nat Nanotechnol, 2016, 11, 218-230.
24. M. Naguib, O. Mashtalir, J. Carle, V. Presser, J. Lu, L. Hultman, Y. Gogotsi and M. W. Barsoum, Acs Nano, 2012, 6, 1322-1331.
25. M. R. Lukatskaya, S. Kota, Z. Lin, M.-Q. Zhao, N. Shpigel, M. D. Levi, J. Halim, P.-L. Taberna, M. W. Barsoum, P. Simon and Y. Gogotsi, 2017, 6, 17105.

26. K. S. Novoselov, A. K. Geim, S. V. Morozov, D. Jiang, Y. Zhang, S. V. Dubonos, I. V. Grigorieva and A. A. Firsov, Science, 2004, 306, 666-669.
27. J. N. Coleman, M. Lotya, A. O'Neill, S. D. Bergin, P. J. King, U. Khan, K. Young, A. Gaucher, S. De, R. J. Smith, I. V. Shvets, S. K. Arora, G. Stanton, H. Y. Kim, K. Lee, G. T. Kim, G. S. Duesberg, T. Hallam, J. J. Boland, J. J. Wang, J. F. Donegan, J. C. Grunlan, G. Moriarty, A. Shmeliov, R. J. Nicholls, J. M. Perkins, E. M. Grieveson, K. Theuwissen, D. W. McComb, P. D. Nellist and V. Nicolosi, Science, 2011, 331, 568-571.
28. F. Wang, J. H. Seo, G. F. Luo, M. B. Starr, Z. D. Li, D. L. Geng, X. Yin, S. Y. Wang, D. G. Fraser, D. Morgan, Z. Q. Ma and X. D. Wang, Nat Commun, 2016, 7.
29. N. P. Dasgupta, X. B. Meng, J. W. Elam and A. B. F. Martinson, Accounts Chem Res, 2015, 48, 341-348.
30. O. Mashtalir, M. Naguib, V. N. Mochalin, Y. Dall'Agnese, M. Heon, M. W. Barsoum and Y. Gogotsi, Nature Communications, 2013, 4.
31. Y. Gogotsi, Nat Mater, 2015, 14, 1079-1080.
32. X. N. Zang, Q. Zhou, J. Y. Chang, K. S. Teh, M. S. Wei, A. Zettl and L. W. Lin, Adv Mater Interfaces, 2017, 4.
33. A. K. Geim and K. S. Novoselov, Nature Materials, 2007, 6, 183-191.
34. X. Zang, Q. Zhou, J. Chang, Y. Liu and L. Lin, Microelectron Eng, 2015, 132, 192-206.
35. K. S. Novoselov, A. K. Geim, S. V. Morozov, D. Jiang, M. I. Katsnelson, I. V. Grigorieva, S. V. Dubonos and A. A. Firsov, Nature, 2005, 438, 197-200.
36. M. H. Oliveira, J. M. J. Lopes, T. Schumann, L. A. Galves, M. Ramsteiner, K. Berlin, A. Trampert and H. Riechert, Nat Commun, 2015, 6.
37. J. H. Lee, E. K. Lee, W. J. Joo, Y. Jang, B. S. Kim, J. Y. Lim, S. H. Choi, S. J. Ahn, J. R. Ahn, M. H. Park, C. W. Yang, B. L. Choi, S. W. Hwang and D. Whang, Science, 2014, 344, 286-289.
38. L. Baraton, Z. B. He, C. S. Lee, C. S. Cojocaru, M. Chtelet, J. L. Maurice, Y. H. Lee and D. Pribat, EPL, 2011, 96.
39. R. M. Jacobberger, B. Kiraly, M. Fortin-Deschenes, P. L. Levesque, K. M. McElhinny, G. J. Brady, R. Rojas Delgado, S. Singha Roy, A. Mannix, M. G. Lagally, P. G. Evans, P. Desjardins, R. Martel, M. C. Hersam, N. P. Guisinger and M. S. Arnold, Nat Commun, 2015, 6.
40. P. W. Sutter, J. I. Flege and E. A. Sutter, Nature Materials, 2008, 7, 406-411.
41. J. Cai, C. A. Pignedoli, L. Talirz, P. Ruffieux, H. Söde, L. Liang, V. Meunier, R. Berger, R. Li, X. Feng, K. Müllen and R. Fasel, Nat Nanotechnol, 2014, 9, 896-900.
42. D. Geng, H. Wang and G. Yu, Advanced Materials, 2015, 27, 2821-2837.
43. Z. Yan, Z. Peng and J. M. Tour, Accounts of Chemical Research, 2014, 47, 1327-1337.
44. G. Ding, Y. Zhu, S. Wang, Q. Gong, L. Sun, T. Wu, X. Xie and M. Jiang, Carbon, 2013, 53, 321-326.
45. D. Geng, B. Wu, Y. Guo, L. Huang, Y. Xue, J. Chen, G. Yu, L. Jiang, W. Hu and Y. Liu, Proceedings of the National Academy of Sciences of the United States of America, 2012, 109, 7992-7996.
46. A. R. Harutyunyan, Proc. Natl. Acad. Sci. USA, 2012, 109.
47. K. K. Nanda, Pramana - Journal of Physics, 2009, 72, 617-628.

48. A. Ismach, C. Druzgalski, S. Penwell, A. Schwartzberg, M. Zheng, A. Javey, J. Bokor and Y. Zhang, Nano Lett, 2010, 10, 1542-1548.
49. T. M. Paronyan, E. M. Pigos, G. Chen and A. R. Harutyunyan, Acs Nano, 2011, 5, 9619-9627.
50. H. Kim, C. Mattevi, M. R. Calvo, J. C. Oberg, L. Artiglia, S. Agnoli, C. F. Hirjibehedin, M. Chhowalla and E. Saiz, Acs Nano, 2012, 6, 3614-3623.
51. P. Y. Huang, C. S. Ruiz-Vargas, A. M. Van Der Zande, W. S. Whitney, M. P. Levendorf, J. W. Kevek, S. Garg, J. S. Alden, C. J. Hustedt, Y. Zhu, J. Park, P. L. McEuen and D. A. Muller, Nature, 2011, 469, 389-392.
52. L. M. Malard, M. A. Pimenta, G. Dresselhaus and M. S. Dresselhaus, Physics Reports, 2009, 473, 51-87.
53. A. C. Ferrari, J. C. Meyer, V. Scardaci, C. Casiraghi, M. Lazzeri, F. Mauri, S. Piscanec, D. Jiang, K. S. Novoselov, S. Roth and A. K. Geim, Phys Rev Lett, 2006, 97.
54. C. Mattevi, H. Kim and M. Chhowalla, Journal of Materials Chemistry, 2011, 21, 3324-3334.
55. D. Wang, H. Tian, Y. Yang, D. Xie, T. L. Ren and Y. Zhang, Scientific Reports, 2013, 3.
56. E. J. H. Lee, K. Balasubramanian, R. T. Weitz, M. Burghard and K. Kern, Nat Nanotechnol, 2008, 3, 486-490.
57. P. Wei, W. Bao, Y. Pu, C. N. Lau and J. Shi, Phys Rev Lett, 2009, 102.
58. M. Brandbyge, J. L. Mozos, P. Ordejón, J. Taylor and K. Stokbro, Physical Review B - Condensed Matter and Materials Physics, 2002, 65, 1654011-16540117.
59. N. M. Gabor, J. C. W. Song, Q. Ma, N. L. Nair, T. Taychatanapat, K. Watanabe, T. Taniguchi, L. S. Levitov and P. Jarillo-Herrero, Science, 2011, 334, 648-652.
60. P. Dollfus, V. H. Nguyen and J. Saint-Martin, Journal of Physics Condensed Matter, 2015, 27.
61. M. Pumera and A. H. Loo, Trac-Trend Anal Chem, 2014, 61, 49-53.
62. J. Zhang, S. H. Liu, H. W. Liang, R. H. Dong and X. L. Feng, Adv Mater, 2015, 27, 7426-+.
63. S. Y. Chen, C. X. Zheng, M. S. Fuhrer and J. Yan, Nano Lett, 2015, 15, 2526-2532.
64. G. A. Muller, J. B. Cook, H. S. Kim, S. H. Tolbert and B. Dunn, Nano Lett, 2015, 15, 1911-1917.
65. Z. W. Seh, J. H. Yu, W. Y. Li, P. C. Hsu, H. T. Wang, Y. M. Sun, H. B. Yao, Q. F. Zhang and Y. Cui, Nat Commun, 2014, 5.
66. E. A. Suslov, O. V. Bushkova, E. A. Sherstobitova, O. G. Reznitskikh and A. N. Titov, Ionics, 2016, 22, 503-514.
67. E. J. Frazer and S. Phang, J Power Sources, 1981, 6, 307-317.
68. Y. Q. Jiang, P. B. Wang, X. N. Zang, Y. Yang, A. Kozinda and L. W. Lin, Nano Lett, 2013, 13, 3524-3530.
69. M. S. Whittingham and J. A. Panella, Mater Res Bull, 1981, 16, 37-45.
70. J. Chen, S. L. Li, Z. L. Tao and F. Gao, Chem Commun, 2003, DOI: 10.1039/b300054k, 980-981.
71. V. Pore, M. Ritala and M. Leskela, Chem Vapor Depos, 2007, 13, 163-168.
72. R. Warren, F. Sammoura, F. Tounsi, M. Sanghadasa and L. W. Lin, J Mater Chem A, 2015, 3, 15568-15575.

73. E. Kao, C. Yang, R. Warren, A. Kozinda and L. W. Lin, Sensor Actuat a-Phys, 2016, 240, 160-166.
74. L. M. Suo, O. Borodin, T. Gao, M. Olguin, J. Ho, X. L. Fan, C. Luo, C. S. Wang and K. Xu, Science, 2015, 350, 938-943.
75. L. Smith and B. Dunn, Science, 2015, 350, 918-918.
76. P. Simon and Y. Gogotsi, Nat Mater, 2008, 7, 845-854.
77. M. Acerce, D. Voiry and M. Chhowalla, Nat Nanotechnol, 2015, 10, 313-318.
78. M. Ghidiu, M. R. Lukatskaya, M. Q. Zhao, Y. Gogotsi and M. W. Barsoum, Nature, 2014, 516, 78-U171.
79. J. P. Liu, J. Jiang, C. W. Cheng, H. X. Li, J. X. Zhang, H. Gong and H. J. Fan, Advanced Materials, 2011, 23, 2076-+.
80. G. H. Yu, L. B. Hu, M. Vosgueritchian, H. L. Wang, X. Xie, J. R. McDonough, X. Cui, Y. Cui and Z. N. Bao, Nano Letters, 2011, 11, 2905-2911.
81. Y. X. Xu, Z. Y. Lin, X. Zhong, X. Q. Huang, N. O. Weiss, Y. Huang and X. F. Duan, Nat Commun, 2014, 5.
82. C. C. Hu, K. H. Chang, M. C. Lin and Y. T. Wu, Nano Letters, 2006, 6, 2690-2695.
83. M. Toupin, T. Brousse and D. Belanger, Chem Mater, 2004, 16, 3184-3190.
84. J. Musschoot, Q. Xie, D. Deduytsche, S. Van den Berghe, R. L. Van Meirhaeghe and C. Detavernier, Microelectron Eng, 2009, 86, 72-77.
85. S. W. Choi, C. M. Jang, D. Y. Kim, J. S. Ha, H. S. Park, W. Koh and C. S. Lee, J Korean Phys Soc, 2003, 42, S975-S979.
86. A. Lewandowski, A. Olejniczak, M. Galinski and I. Stepniak, J Power Sources, 2010, 195, 5814-5819.
87. M. Lovric, M. Hermes and F. Scholz, J Solid State Electr, 1998, 2, 401-404.
88. S. D. Tilley, M. Schreier, J. Azevedo, M. Stefik and M. Graetzel, Adv Funct Mater, 2014, 24, 303-311.
89. D. H. Deng, K. S. Novoselov, Q. Fu, N. F. Zheng, Z. Q. Tian and X. H. Bao, Nat Nanotechnol, 2016, 11, 218-230.
90. Y. J. Han, X. Yue, Y. S. Jin, X. D. Huang and P. K. Shen, J Mater Chem A, 2016, 4, 3673-3677.
91. V. Augustyn, P. Simon and B. Dunn, Energ Environ Sci, 2014, 7, 1597-1614.
92. M. Chintapalli, K. Timachova, K. R. Olson, S. J. Mecham, D. Devaux, J. M. DeSimone and N. P. Balsara, Macromolecules, 2016, 49, 3508-3515.
93. Y. W. Zhu, S. Murali, M. D. Stoller, K. J. Ganesh, W. W. Cai, P. J. Ferreira, A. Pirkle, R. M. Wallace, K. A. Cychosz, M. Thommes, D. Su, E. A. Stach and R. S. Ruoff, Science, 2011, 332, 1537-1541.
94. C. G. Liu, Z. N. Yu, D. Neff, A. Zhamu and B. Z. Jang, Nano Letters, 2010, 10, 4863-4868.
95. S. T. Oyama, in The chemistry of transition metal carbides and nitrides, Springer, 1996, pp. 1-27.
96. M. Naguib, J. Come, B. Dyatkin, V. Presser, P. L. Taberna, P. Simon, M. W. Barsoum and Y. Gogotsi, Electrochemistry Communications, 2012, 16, 61-64.
97. M. Ghidiu, M. R. Lukatskaya, M. Q. Zhao, Y. Gogotsi and M. W. Barsoum, Nature, 2014, 516, 78-U171.

98. M. Khazaei, M. Arai, T. Sasaki, C. Y. Chung, N. S. Venkataramanan, M. Estili, Y. Sakka and Y. Kawazoe, Advanced Functional Materials, 2013, 23, 2185-2192.
99. Mashtalir, M. Naguib, V. N. Mochalin, Y. Dall'Agnese, M. Heon, M. W. Barsoum and Y. Gogotsi, Nature Communications, 2013, 4.
100. P. Eklund, M. Beckers, U. Jansson, H. Högberg and L. Hultman, Thin Solid Films, 2010, 518, 1851-1878.
101. S. Ingason, M. Dahlqvist and J. Rosen, J Phys-Condens Mat, 2016, 28.
102. Y. Gogotsi, Nat Mater, 2015, 14, 1079-1080.
103. C. Xu, L. Wang, Z. Liu, L. Chen, J. Guo, N. Kang, X.-L. Ma, H.-M. Cheng and W. Ren, Nat Mater, 2015, 14, 1135-1141.
104. R. S. Kappes, F. Schonfeld, C. Li, A. A. Golriz, M. Nagel, T. Lippert, H. J. Butt and J. S. Gutmann, Springerplus, 2014, 3.
105. L. E. R. O'Leary, J. A. Fallas, E. L. Bakota, M. K. Kang and J. D. Hartgerink, Nat Chem, 2011, 3, 821-828.
106. S. S. Harilal, J. R. Freeman, P. K. Diwakar and A. Hassanein, Springer Ser Opt Sci, 2014, 182, 143-166.
107. S. B. Ogale, P. P. Patil, D. M. Phase, Y. V. Bhandarkar, S. K. Kulkarni, S. Kulkarni, S. V. Ghaisas and S. M. Kanetkar, Phys Rev B, 1987, 36, 8237-8250.
108. J. Bello, H. R. Bello and J. R. Vinograd, Biochimica et Biophysica Acta, 1962, 57, 222-229.
109. Royon, Y. Petit, G. Papon, M. Richardson and L. Canioni, Opt Mater Express, 2011, 1, 866-882.
110. M. R. Lukatskaya, O. Mashtalir, C. E. Ren, Y. Dall'Agnese, P. Rozier, P. L. Taberna, M. Naguib, P. Simon, M. W. Barsoum and Y. Gogotsi, Science, 2013, 341, 1502-1505.
111. J. Lin, Z. W. Peng, Y. Y. Liu, F. Ruiz-Zepeda, R. Q. Ye, E. L. G. Samuel, M. J. Yacaman, B. I. Yakobson and J. M. Tour, Nature Communications, 2014, 5.
112. Y. H. Jung, T. H. Chang, H. L. Zhang, C. H. Yao, Q. F. Zheng, V. W. Yang, H. Y. Mi, M. Kim, S. J. Cho, D. W. Park, H. Jiang, J. Lee, Y. J. Qiu, W. D. Zhou, Z. Y. Cai, S. Q. Gong and Z. Q. Ma, Nat Commun, 2015, 6.
113. A. Russo, B. Y. Ahn, J. J. Adams, E. B. Duoss, J. T. Bernhard and J. A. Lewis, Adv Mater, 2011, 23, 3426-+.
114. Z. L. Wang, Acs Nano, 2013, 7, 9533-9557.
115. Z. L. Wang, Mater Today, 2017, 20, 74-82.
116. T. H. Nguyen, A. Fraiwan and S. Choi, Biosensors & Bioelectronics, 2014, 54, 640-649.
117. Q. C. Liu, L. Li, J. J. Xu, Z. W. Chang, D. Xu, Y. B. Yin, X. Y. Yang, T. Liu, Y. S. Jiang, J. M. Yan and X. B. Zhang, Adv Mater, 2015, 27, 8095-8101.
118. L. Nyholm, G. Nystrom, A. Mihranyan and M. Stromme, Adv Mater, 2011, 23, 3751-3769.
119. V. L. Pushparaj, M. M. Shaijumon, A. Kumar, S. Murugesan, L. Ci, R. Vajtai, R. J. Linhardt, O. Nalamasu and P. M. Ajayan, Proceedings of the National Academy of Sciences of the United States of America, 2007, 104, 13574-13577.
120. D. W. Wang, F. Li, J. P. Zhao, W. C. Ren, Z. G. Chen, J. Tan, Z. S. Wu, I. Gentle, G. Q. Lu and H. M. Cheng, Acs Nano, 2009, 3, 1745-1752.

121. X. Y. Liu, M. Mwangi, X. J. Li, M. O'Brien and G. M. Whitesides, Lab on a Chip, 2011, 11, 2189-2196.
122. Q. Z. Zhong, J. W. Zhong, B. Hu, Q. Y. Hu, J. Zhou and Z. L. Wang, Energy & Environmental Science, 2013, 6, 1779-1784.
123. A. A. Kumar, J. W. Hennek, B. S. Smith, S. Kumar, P. Beattie, S. Jain, J. P. Rolland, T. P. Stossel, C. Chunda-Liyoka and G. M. Whitesides, Angew Chem Int Edit, 2015, 54, 5835-5852.
124. A. W. Martinez, S. T. Phillips, G. M. Whitesides and E. Carrilho, Analytical Chemistry, 2010, 82, 3-10.
125. E. Carrilho, A. W. Martinez and G. M. Whitesides, Analytical Chemistry, 2009, 81, 7091-7095.
126. P. K. Yang, Z. H. Lin, K. C. Pradel, L. Lin, X. H. Li, X. N. Wen, J. H. He and Z. L. Wang, Acs Nano, 2015, 9, 901-907.
127. S. Felton, M. Tolley, E. Demaine, D. Rus and R. Wood, Science, 2014, 345, 644-646.
128. Wagner, R. S.; Ellis, W. C. Appl Phys Lett 1964, 4, (5), 89-&.
129. Sinno, T.; Dornberger, E.; von Ammon, W.; Brown, R. A.; Dupret, F. Mat Sci Eng R 2000, 28, (5-6), 149-198.
130. Sun, Z.; Liao, T.; Dou, Y.; Hwang, S. M.; Park, M.-S.; Jiang, L.; Kim, J. H.; Dou, S. X. Nature Communications 2014, 5, 3813.
131. Shi, Y. M.; Li, H. N.; Li, L. J. Chem Soc Rev 2015, 44, (9), 2744-2756.
132. Kang, K.; Xie, S.; Huang, L.; Han, Y.; Huang, P. Y.; Mak, K. F.; Kim, C.-J.; Muller, D.; Park, J. Nature 2015, 520, (7549), 656-660.
133. Li, Y. F.; Yoda, M. Int J Heat Mass Tran 2016, 102, 369-380.
134. Uricanu, V. I.; Duits, M. H. G.; Filip, D.; Nelissen, R. M. F.; Agterof, W. G. M. J Colloid Interf Sci 2006, 298, (2), 920-934.
135. Zhou, Y. B.; Deng, B.; Zhou, Y.; Ren, X. B.; Yin, J. B.; Jin, C. H.; Liu, Z. F.; Peng, H. L. Nano Lett 2016, 16, (3), 2103-2107.
136. Zolyomi, V.; Drummond, N. D.; Fal'ko, V. I. Phys Rev B 2013, 87, (19).
137. Lu, Z.; Lee, O.; Wong, J. C.; Salahuddin, S. J Mater Res 2016, 31, (7), 911-916.